



Cite this: DOI: 10.1039/d5sc09176d

## Recent advances and design strategies of cathode materials for aqueous aluminum-ion batteries

Jiayou Feng, Shuimei Chen, Yuzheng Wu, Xiaodan Huang \* and Chengzhong Yu \*

The growing global energy demand stimulates the urgent need for safe, sustainable, and cost-effective energy storage technologies. Aqueous aluminum-ion batteries (AAIBs) have emerged as promising candidates owing to their abundant resources, intrinsic safety, environmental compatibility, and high capacity. AAIB research has seen rapid development, focusing on high-capacity cathodes compatible with Al anodes. The high charge density of trivalent  $\text{Al}^{3+}$  induces strong electrostatic interactions with the cathode, impeding ion transport, causing structural distortion, and accelerating capacity decay, while side reactions in aqueous electrolytes further limit reversibility and stability. Addressing these challenges requires a mechanistic understanding of how the cathode composition and structure regulate  $\text{Al}^{3+}$ –cathode interactions and redox behavior. This review analyzes the fundamental  $\text{Al}^{3+}$  storage mechanisms in AAIBs, emphasizing the influence of cathode chemistry, structural characteristics, and electrolyte environment on ion transport,  $\text{Al}^{3+}$ –cathode interactions and electrochemical performance. Furthermore, representative cathodes, including manganese-based oxides, vanadium-based compounds, Prussian blue analogues and organic cathode materials, are systematically summarized in terms of structure, performance, and optimization strategies. Finally, the review outlines current challenges and prospective research directions for advancing next-generation high-performance AAIB cathodes. This review is expected to provide valuable insights for guiding cathode material design and inspire future strategies to enhance the capacity, stability, and rate performance of AAIBs.

Received 24th November 2025

Accepted 30th December 2025

DOI: 10.1039/d5sc09176d

rsc.li/chemical-science

## 1. Introduction

The fast-growing global energy consumption has intensified the demand for sustainable and efficient energy storage, driving the advancement of next-generation electrochemical storage technologies. In recent decades, lithium-ion batteries (LIBs) have dominated portable electronics, electric vehicles, and grid-scale applications, owing to their high energy density and long cycle life.<sup>1–3</sup> However, their further advancement is hindered by intrinsic limitations: scarce lithium resources increase cost and supply risks, while flammable and toxic organic carbonate electrolytes pose serious safety hazards such as leakage, combustion, and even explosion.<sup>4,5</sup> Moreover, repeated lithium plating and stripping also induce dendrite formation, which can trigger internal short circuits and thermal runaway.<sup>6–8</sup> These issues highlight the urgent need for the development of next-generation electrochemical storage systems that offer enhanced safety, environmental friendliness, and cost-effectiveness.

In response to these challenges, researchers have turned their attention to post-lithium-ion batteries based on abundant

elements such as sodium (Na), potassium (K), zinc (Zn), magnesium (Mg), calcium (Ca), and aluminum (Al).<sup>9–16</sup> Among these, aluminum has attracted particular attention as the most abundant metal in the Earth's crust (~8.2 wt%) and for its low cost (Fig. 1a).<sup>17</sup> Furthermore, aluminum can reversibly transfer three electrons per atom, yielding a high theoretical gravimetric capacity of ~2980 mAh g<sup>−1</sup> and a volumetric capacity of ~8046 mAh cm<sup>−3</sup>, which is approximately four times that of lithium metal.<sup>18</sup> These attributes position aluminum as a promising candidate for the development of high-capacity and cost-effective energy storage systems. Aluminum-ion batteries (AIBs) are typically categorized into two types based on the electrolyte: organic and aqueous systems.<sup>19,20</sup> Organic AIBs generally utilize ionic liquids as electrolytes, whereas aqueous AIBs (AAIBs) employ aqueous solutions of aluminum salts. Compared to organic systems, aqueous electrolytes offer several advantages, including non-toxicity, low cost, and non-flammability, thereby ensuring enhanced safety and stability.<sup>21,22</sup> Additionally, their low viscosity and high dielectric constant contribute to high ionic conductivity, improving electrochemical kinetics.<sup>18</sup> Consequently, AAIBs have attracted widespread attention as a safe, low-cost, and high-performance energy storage technology, with a rapidly increasing number of publications in recent decades (Fig. 1b).

Australian Institute for Bioengineering and Nanotechnology, The University of Queensland, Brisbane, QLD 4072, Australia. E-mail: x.huang@uq.edu.au; c.yu@uq.edu.au



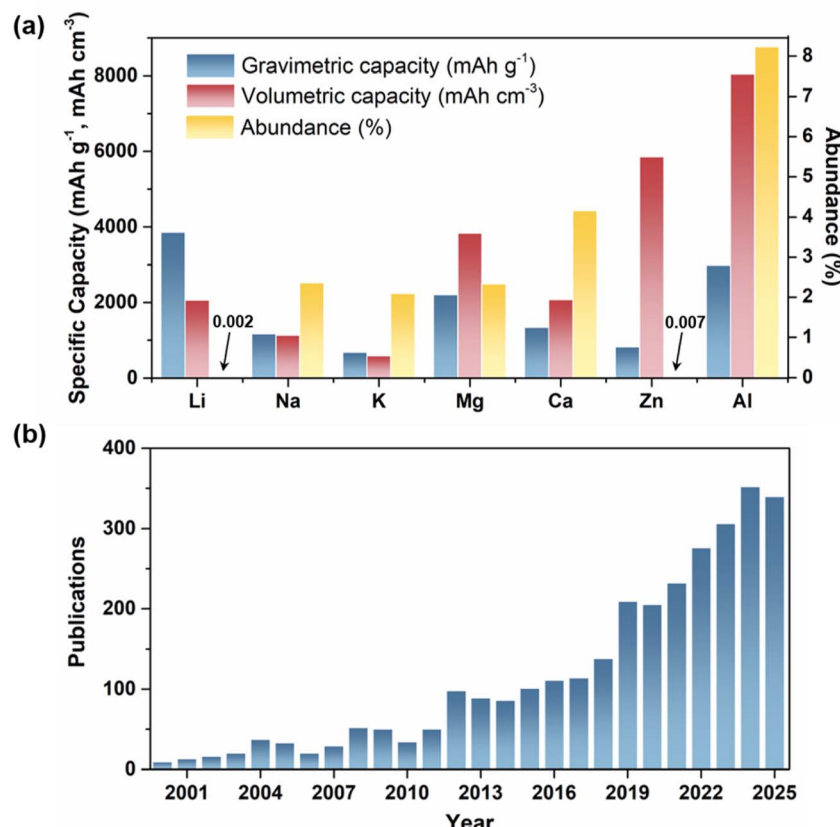


Fig. 1 (a) Comparison of different metal anodes in terms of gravimetric capacity, volumetric capacity and earth's crust abundance. (b) Publication trends of aqueous aluminum-ion batteries from 2000 to 2025. Data were obtained from the Web of Science using the search keywords "aqueous aluminum-ion battery", "aqueous aluminum ion battery", or "AAIB".

Nevertheless, AAIBs still face several scientific and technical challenges. Although trivalent  $\text{Al}^{3+}$  offers a high theoretical capacity, its small ionic radius and high charge density ( $364 \text{ mm}^{-3}$ ) lead to strong electrostatic interactions within the cathode matrix.<sup>18,23–25</sup> These interactions hinder ion migration and charge transfer, limit the reversible insertion/extraction of  $\text{Al}^{3+}$ , and induce structural distortion and collapse during cycling, resulting in rapid capacity decay. Additionally, side reactions in aqueous electrolytes, such as hydrogen evolution, anode corrosion, and the formation of passivating oxide layers, further deteriorate coulombic efficiency and cycling stability.<sup>26,27</sup> These issues highlight that one of the key directions for advancing AAIBs lies in designing cathode materials capable of regulating  $\text{Al}^{3+}$ –host interactions to achieve reversible ion storage with minimal structural deformation. A mechanistic understanding of how the cathode structure and chemical characteristics govern  $\text{Al}^{3+}$  accessibility, migration kinetics, and redox reversibility is therefore essential for guiding the rational development of high-capacity, high-rate and high-stability cathode systems. To date, most published reviews on AAIBs have primarily provided general overviews of recent progress and challenges in cathodes, anodes, and electrolytes.<sup>21,28–30</sup> However, comprehensive reviews dedicated to AAIBs cathode materials remain scarce, and systematic comparisons of their structural characteristics, energy storage mechanisms, and electrochemical behaviors are still lacking.

Therefore, this review presents a systematic analysis of cathode materials for AAIBs. We first outline the fundamental energy storage mechanisms, with particular emphasis on how the chemical nature and structural characteristics of the cathode, along with the electrolyte environment, govern  $\text{Al}^{3+}$  transport behavior and host–guest interactions, thereby determining the electrochemical performance in terms of capacity, reversibility, rate capability, and cycling stability. Subsequently, we categorize representative cathodes into four categories: manganese-based oxides, vanadium-based compounds, Prussian blue analogues, and organic materials (Fig. 2), and discuss their structural features, corresponding electrochemical behaviors and optimization strategies. By comparing their distinct  $\text{Al}^{3+}$ –host interactions mechanisms and structure–performance relationships, this review aims to provide comprehensive scientific guidance for the rational design and future development of high-performance cathode materials for AAIBs. Finally, the challenges and promising research directions for each cathode category are summarized to inspire further progress in this emerging field.

## 2. Energy storage mechanisms of AAIBs

AAIBs are typically composed of a cathode, an anode, electrolyte and a separator. The cathode materials are primarily transition-

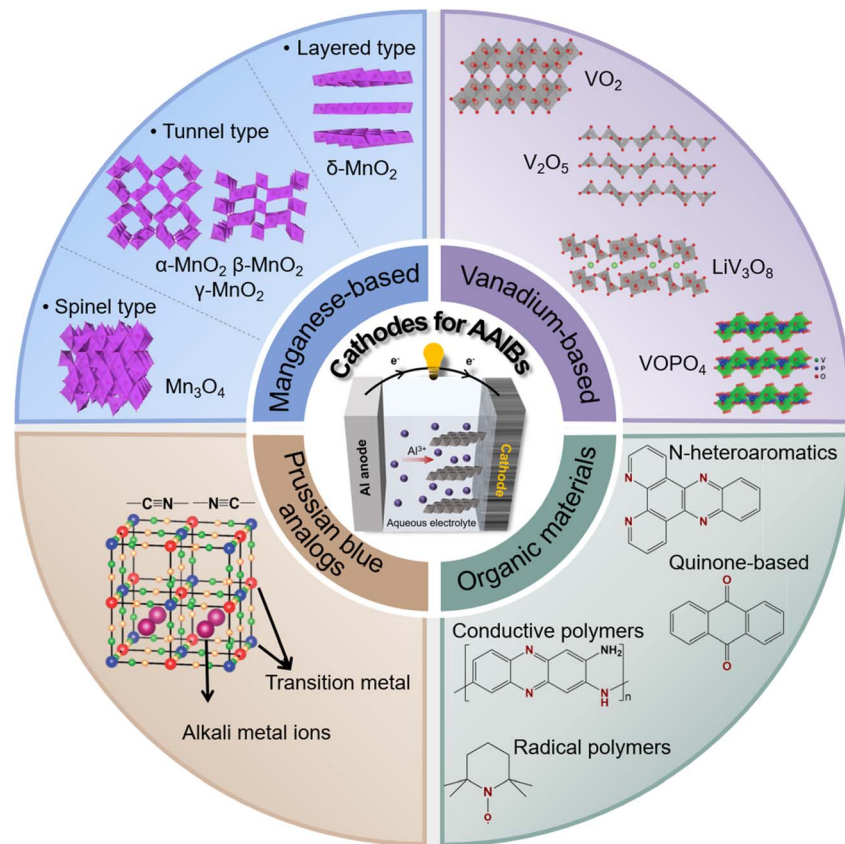
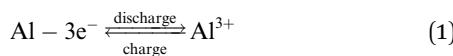


Fig. 2 Representative categories of cathode materials developed for AAIBs.

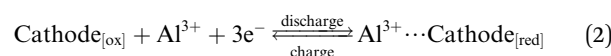
metal oxides or organic compounds, while aluminum metal or aluminum alloys serve as the anode. Glass fiber is commonly used as the separator, and the electrolyte usually consists of aqueous solutions containing aluminum salts such as  $\text{Al}(\text{OTf})_3$  or  $\text{Al}_2(\text{SO}_4)_3$ .

During the charge–discharge process, reversible redox reactions occur at both electrodes. The  $\text{Al}^{3+}$  ions in solvated form (denoted as  $\text{Al}^{3+}$  for simplicity) serve as charge carriers that migrate through the electrolyte, while electrons are transferred in the external circuit between the anode and cathode. Specifically, during discharge, the aluminum anode undergoes oxidation, releasing three electrons to form  $\text{Al}^{3+}$  (eqn (1)). The  $\text{Al}^{3+}$  ions migrate toward the cathode through the electrolyte, whereas the released electrons travel through the external circuit to reach the cathode. The active cathode material in the oxidation form (Cathode<sub>[ox]</sub>) gains electrons and undergoes transformation into the reduced form (Cathode<sub>[red]</sub>), accompanied by host–guest interaction between the incoming  $\text{Al}^{3+}$  species and the reduced cathode material (eqn (2)). In the subsequent charging process, this reaction reverses:  $\text{Al}^{3+}$  ions are extracted from the cathode, migrate back to the anode, and are reduced to metallic aluminum, thereby completing a reversible charge–discharge cycle.

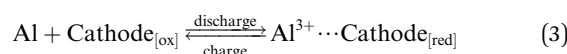
Anode:



Cathode:



Overall:



## 2.1 Factors affecting the electrochemical mechanism

The energy storage mechanism of AAIBs is related to the reaction shown in eqn (3), *i.e.*, the host–guest interactions between  $\text{Al}^{3+}$  and the cathode active species, the reversibility of reaction 3 in the charge–discharge process, and the possible occurrence of side reactions. These factors are ultimately dictated by the structural and chemical characteristics of the cathode material and the electrolyte environment, including the anion salt type, concentration and pH, which in turn determine the key electrochemical performance metrics of AAIBs.

Firstly, the chemical nature of the cathode material is a key factor governing the energy storage mechanism of AAIBs. The type of electroactive center not only determines the redox reversibility but also influences the type and strength of interaction with  $\text{Al}^{3+}$ . For inorganic transition-metal oxide cathodes, specific redox couples control both electron-transfer reversibility and reaction kinetics, depending on the electronic



structure of the metal centers. Transition metals with partially filled 3d orbitals enable reversible redox reactions, such as Mn ( $Mn^{2+}/Mn^{3+}/Mn^{4+}$ ) and V ( $V^{3+}/V^{4+}/V^{5+}$ ) oxides. Their tunable valence ranges allow multiple electron transfers with minimal structural distortion, making them the most widely studied inorganic cathode materials.<sup>31–33</sup> Nevertheless, strong coulombic interactions between  $Al^{3+}$  and oxygen in the metal oxide can induce lattice stress or even structural collapse during repeated  $Al^{3+}$  extraction/insertion, thereby limiting the rate capability and cycling stability. For organic cathodes, the redox reversibility primarily depends on the intrinsic reversibility of the functional groups, such as  $C=O/C-OH$ . Functional groups within conjugated  $\pi$ -systems or capable of stabilizing negative charges or radical intermediates tend to exhibit higher reversibility.<sup>34,35</sup> During discharge,  $Al^{3+}$  coordinates with these negatively charged sites to maintain charge neutrality, so the stability of  $Al^{3+}$ -functional group interaction also dictates the redox reversibility. Compared with inorganic cathodes, organic cathodes exhibit weaker  $Al^{3+}$  coordination, leading to less structural distortion during ion transport and consequently superior rate capability and cycling stability.

Secondly, the structural characteristics of the cathode material also affect the energy storage mechanism of AAIBs. Parameters such as interlayer spacing, cavity size, and the exposure of active sites directly determine  $Al^{3+}$  accessibility and diffusion kinetics. Cathodes featuring larger interlayer spacing or more open frameworks offer wider migration channels, thereby facilitating faster  $Al^{3+}$  transport and enhancing redox reactions during charge and discharge. For inorganic transition-metal oxide cathodes, layered structures generally provide larger diffusion pathways for  $Al^{3+}$  compared with tunnel-type frameworks, resulting in improved ion transport kinetics. However, the relatively weak structural rigidity of layered materials makes them prone to lattice strain or even collapse upon repeated  $Al^{3+}$  insertion and extraction. Therefore, achieving a balance between sufficient diffusion space and structural stability remains a critical challenge. For organic cathodes, the highly exposed active centers facilitate ion accessibility, while the flexible molecular backbones can effectively accommodate volume changes, thereby mitigating structural stress during cycling. As a result, despite relatively lower specific capacity, organic cathodes generally exhibit superior structural stability and rate performance compared with their rigid inorganic counterparts.

In addition, the electrolyte environment, including anion salt type, concentration and pH, also significantly affects the charge-discharge behavior and energy storage mechanisms of AAIBs. These factors determine the solvation structure of  $Al^{3+}$  and the likelihood of side reactions. Typically, in highly concentrated electrolytes, the proportion of free water is reduced. This suppresses water activity, mitigates the hydrogen evolution reaction (HER), and facilitates the reversible deposition of Al on the anode.<sup>36</sup> The type of anion (*e.g.*,  $Cl^-$ ,  $OTf^-$ , and  $SO_4^{2-}$ ) also regulates the coordination environment of  $Al^{3+}$ . For instance,  $CF_3SO_3^-$  ( $OTf^-$ ) can reduce the number of water molecules surrounding the cation, thereby promoting ion transport and charge transfer, making it a commonly used salt

in aqueous batteries.<sup>37</sup> Moreover, the electrolyte pH also influences the insertion behavior of cations. Adjusting the pH allows selective regulation of  $Al^{3+}$  and  $H^+$  insertion during the electrochemical process, with  $H^+$  insertion typically occurring under relatively low pH conditions.<sup>38</sup> Sometimes, the introduction of co-solvents such as acetonitrile (AN) and triethyl phosphate (TEP) into a hydrated eutectic  $Al^{3+}$  electrolyte can reduce water activity, suppress side reactions like the HER and corrosion, and widen the electrochemical stability window, thereby enhancing the stability and reversibility of AAIBs.<sup>39</sup>

## 2.2 Impact on electrochemical performance

The aforementioned chemical and structural characteristics of the cathode, together with the electrolyte environment, influence the redox behavior and host-guest interactions with  $Al^{3+}$ , ultimately affecting the overall electrochemical performance of AAIBs, including capacity performances and the cycling stability.

The capacity performances, including rate capacities, are fundamentally dictated by the redox activity and ion transport dynamics within the cathodes. The theoretical specific capacity is primarily determined by the number of electrons involved in redox reactions, governed by the valence changes of metal centers in inorganic cathodes and by the number of redox-active functional groups in organic cathodes. The achievable capacity depends on the structural accessibility of  $Al^{3+}$  ions and the efficiency of redox reactions. Inorganic cathode materials with larger interlayer spacing or more open frameworks can better accommodate  $Al^{3+}$ , providing wider diffusion channels and sufficient storage sites, thereby enabling higher capacity. Generally, layered structures are more favorable for  $Al^{3+}$  accommodation than tunnel-type frameworks, leading to superior capacity performance. For organic cathodes, flexible backbones or porous structures can facilitate  $Al^{3+}$  diffusion, while densely packed molecules often exhibit lower practical capacities due to limited ion accessibility. The rate capability is largely determined by the diffusion kinetics of  $Al^{3+}$  within the cathode and the efficiency of charge transport. Slow ion diffusion limits charge transfer per unit time, resulting in significant capacity decay at high current densities. For inorganic cathodes, constructing materials with high specific surface area and abundant defects can accelerate ion transport and enhance reaction kinetics. Additionally, hybridization with conductive carbon improves electronic conductivity, further supporting high-rate performance. For organic cathodes, highly exposed active sites facilitate rapid  $Al^{3+}$  access and diffusion, promoting excellent rate capability.

For cycling stability, both the intrinsic redox reversibility of the cathode and the strength of  $Al^{3+}$ -host interactions play decisive roles. In inorganic metal oxide cathodes, the high charge density of  $Al^{3+}$  leads to strong electrostatic interactions with the lattice, which hinders ion diffusion and induces lattice strain, phase transitions, or even partial dissolution, ultimately reducing reaction reversibility and leading to structural collapse and capacity fading. To mitigate this, introducing stabilizing species, such as metal cations or organic molecules, has been



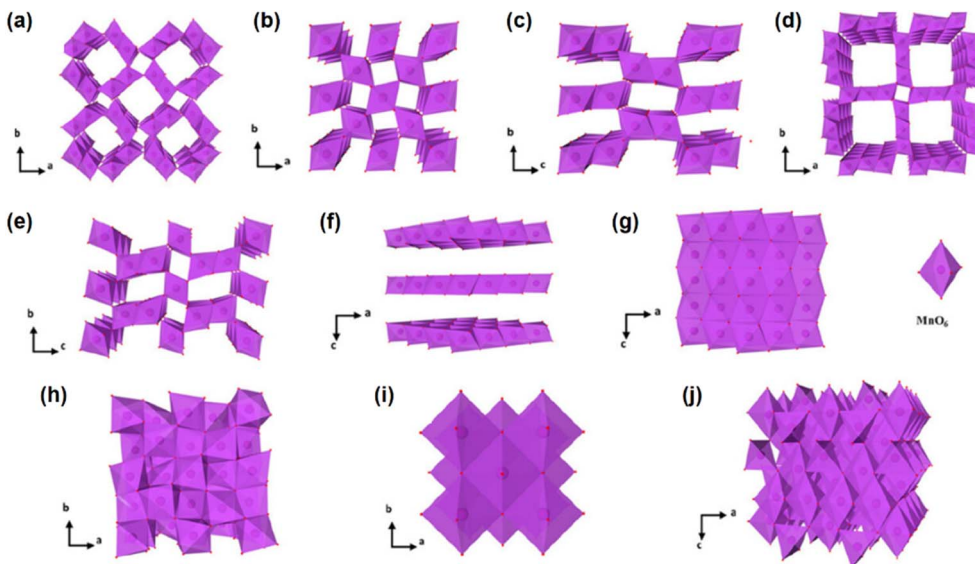


Fig. 3 Crystal structures of (a)  $\alpha$ -MnO<sub>2</sub>, (b)  $\beta$ -MnO<sub>2</sub>, (c) R-MnO<sub>2</sub>, (d) T-MnO<sub>2</sub>, (e)  $\gamma$ -MnO<sub>2</sub>, (f)  $\delta$ -MnO<sub>2</sub>, (g)  $\varepsilon$ -MnO<sub>2</sub>, (h) Mn<sub>2</sub>O<sub>3</sub>, (i) MnO, and (j) Mn<sub>3</sub>O<sub>4</sub>. Reproduced with permission.<sup>41</sup> Copyright 2024, American Chemical Society.

shown to weaken these electrostatic interactions and tune the host–guest coupling strength to a moderate level. This strategy effectively buffers volumetric changes, suppresses structural degradation and maintains framework integrity, thereby enhancing both redox reversibility and cycling stability. In contrast, the interactions between Al<sup>3+</sup> and organic cathodes are generally mild, making the redox reversibility primarily depend on the intrinsic reversibility of the functional groups. Functional groups within conjugated  $\pi$ -systems or capable of stabilizing negative charges or radical intermediates tend to exhibit good reversibility. Moreover, the flexible molecular backbones of organic cathodes can effectively accommodate volumetric changes during Al<sup>3+</sup> interaction, helping to preserve framework integrity and enhance cycling stability. Additionally, dissolution of cathode materials leads to active material loss and structural degradation, thereby accelerating capacity fading and shortening cycling life.

Collectively, the intrinsic redox behavior of the cathode active centers and the host–guest interactions between Al<sup>3+</sup> and the cathode material jointly determine the key electrochemical parameters of AAIBs, including specific capacity, rate capability, reversibility, and cycling stability. Therefore, a rational selection of cathode materials and modulation of Al<sup>3+</sup>–host interactions are of great significance for the design of next-generation high-performance cathode materials for AAIBs.

### 3. Cathode materials for AAIBs

#### 3.1 Manganese-based cathode materials

Manganese oxides have attracted intensive attention as cathode materials for energy storage, primarily due to their abundant natural reserves, low cost and nontoxicity.<sup>31,40</sup> The multiple oxidation states of manganese (Mn<sup>2+</sup>/Mn<sup>3+</sup>/Mn<sup>4+</sup>/Mn<sup>7+</sup>) support multi-electron transfer reactions, thereby enabling a high

theoretical specific capacity of 616 mAh g<sup>-1</sup> (based on the Mn<sup>4+</sup>/Mn<sup>2+</sup> redox couple). In addition, this redox flexibility leads to the formation of a variety of manganese oxides with distinct structures (Fig. 3). MnO<sub>2</sub> and Mn<sub>2</sub>O<sub>3</sub> are generally composed of edge- or corner-sharing [MnO<sub>6</sub>] octahedra, while MnO adopts a face-centered cubic structure, and Mn<sub>3</sub>O<sub>4</sub> is considered a mixture of Mn<sub>2</sub>O<sub>3</sub> and MnO.<sup>41,42</sup> Notably, MnO<sub>2</sub> exhibits diverse phases, including tunnel-type (e.g.,  $\alpha$ -MnO<sub>2</sub>,  $\beta$ -MnO<sub>2</sub>, R-MnO<sub>2</sub>, T-MnO<sub>2</sub>, and  $\gamma$ -MnO<sub>2</sub>), layered-type (e.g.,  $\delta$ -MnO<sub>2</sub>, birmessite) and three-dimensional spinel-type (e.g.,  $\varepsilon$ -MnO<sub>2</sub>). This structural diversity endows Mn-based oxides with tunability in Al<sup>3+</sup> storage behavior, making them highly attractive cathode materials for AAIBs, with ongoing efforts focused on elucidating their intercalation mechanisms and enhancing electrochemical performance through structural engineering.

The electrochemical stability and ion transport properties of manganese oxides are strongly dependent on their crystal structure.<sup>43</sup> Among tunnel-type MnO<sub>2</sub>,  $\beta$ -MnO<sub>2</sub> possesses the narrowest channels ( $1 \times 1$ ,  $2.3 \times 2.3 \text{ \AA}^2$ ) and is considered the most thermodynamically stable.<sup>41</sup> However, its narrow tunnels severely limit ion diffusion, resulting in poor electrochemical performance. To date, no studies have reported its application as a cathode in AAIBs. In contrast,  $\alpha$ -MnO<sub>2</sub> features larger  $2 \times 2$  ( $4.6 \times 4.6 \text{ \AA}^2$ ) tunnels, which facilitate ion transport and accommodate larger ionic species, making it the most widely investigated tunnel-type MnO<sub>2</sub> for AAIB cathodes.  $\gamma$ -MnO<sub>2</sub>, with mixed  $1 \times 1$  ( $2.3 \times 2.3 \text{ \AA}^2$ ) and  $1 \times 2$  ( $2.3 \times 4.6 \text{ \AA}^2$ ) tunnels, exhibits intermediate structural openness, and some studies have focused on defect engineering to improve its ion diffusion capabilities. Layered-type  $\delta$ -MnO<sub>2</sub> offers a larger interlayer spacing ( $\sim 0.7 \text{ nm}$ ), significantly exceeding the tunnel sizes of other MnO<sub>2</sub>. This enhanced ion-accessible volume and facilitates ion intercalation, and it has thus attracted considerable interest as a high-capacity cathode material.<sup>44</sup> In the following

sections, we will systematically discuss the electrochemical behavior of different manganese oxides in AAIBs.

**3.1.1 Tunnel-type manganese oxides.** In 2018, Archer *et al.* used  $\alpha$ -MnO<sub>2</sub> with a  $2 \times 2$  tunnel structure as a cathode material in AAIBs.<sup>45</sup> By pairing  $\alpha$ -MnO<sub>2</sub> with an ionic liquid treated aluminum anode (TAI), the TAI/2 M Al(OTf)<sub>3</sub>/ $\alpha$ -MnO<sub>2</sub> full cell demonstrated a high specific capacity of 380 mAh g<sup>-1</sup> and an average discharge potential of approximately 1.3 V at a current density of 100 mA g<sup>-1</sup>. During electrochemical cycling, reversible formation and dissolution of an amorphous layer composed of low-valence manganese oxides occur on the surface of  $\alpha$ -MnO<sub>2</sub>. This study provided the first compelling evidence for the viability of manganese oxides, particularly  $\alpha$ -MnO<sub>2</sub>, as high-capacity cathode materials in AAIBs. However, the cell showed limited capacity retention, maintaining a discharge capacity of just 168 mAh g<sup>-1</sup> after 40 cycles at 100 mA g<sup>-1</sup>.

Given the intrinsic limitations of pristine  $\alpha$ -MnO<sub>2</sub>, such as sluggish Al<sup>3+</sup> transport within the narrow tunnels and structural instability arising from repeated Al<sup>3+</sup>-cathode interactions, subsequent studies have focused on structural optimization strategies, such as introducing defects and expanding tunnel dimensions, to improve ionic accessibility and electrochemical performance. In 2024, Li *et al.* developed  $\alpha$ -MnO<sub>2</sub> with oxygen vacancies (denoted as O<sub>d</sub>-MnO<sub>2</sub>) by calcination under an argon atmosphere and employed it as a cathode material for AAIBs.<sup>46</sup> The introduction of oxygen vacancies facilitated the opening of the microstructure, enhancing electrolyte accessibility and accelerating electrochemical reaction kinetics. As a result, the O<sub>d</sub>-MnO<sub>2</sub> cathode exhibited improved rate performance and cycling stability. In 5 M Al(OTf)<sub>3</sub> electrolyte, it delivered a discharge plateau at  $\sim$ 1.5 V and a high specific capacity of 480 mAh g<sup>-1</sup> at a current density of 100 mA g<sup>-1</sup>. Compared to pristine  $\alpha$ -MnO<sub>2</sub>, O<sub>d</sub>-MnO<sub>2</sub> retained 100 mAh g<sup>-1</sup> after 180 cycles at 500 mA g<sup>-1</sup>, whereas the capacity of  $\alpha$ -MnO<sub>2</sub> rapidly decayed within 40 cycles (Fig. 4a). This enhancement was attributed to the presence of oxygen vacancies, which provided structural flexibility to accommodate volume changes during cycling, thereby improving stability. Therefore, oxygen vacancies can enhance the electrochemical performance of  $\alpha$ -MnO<sub>2</sub> by improving ion/electron transport and increasing structural flexibility, making it an effective strategy for MnO<sub>2</sub> optimization in AAIBs.

$\gamma$ -MnO<sub>2</sub> features a mixed tunnel structure composed of  $1 \times 1$  and  $1 \times 2$  channels, which are narrower than the tunnels of  $\alpha$ -MnO<sub>2</sub> and thus less favorable for Al<sup>3+</sup> intercalation. To overcome this limitation,  $\gamma$ -MnO<sub>2</sub> enriched with oxygen vacancies (denoted as O<sub>v</sub>-MnO<sub>2</sub>) was synthesized *via* annealing under an argon atmosphere.<sup>47</sup> The introduction of oxygen vacancies can open the MnO<sub>6</sub> octahedral framework, generating additional ion diffusion pathways and extending the proton diffusion path along the *a-c* plane, thereby enhancing the overall capacity (Fig. 4b). In 5 M Al(OTf)<sub>3</sub> electrolyte, O<sub>v</sub>-MnO<sub>2</sub> delivered a high discharge capacity of 481.9 mAh g<sup>-1</sup> at 200 mA g<sup>-1</sup> and maintained 128.6 mAh g<sup>-1</sup> after 200 cycles at 0.4 A g<sup>-1</sup>. To the best of our knowledge,  $\beta$ -MnO<sub>2</sub>, which possesses only  $1 \times 1$  tunnel structures, has not yet been explored as a cathode material for

AAIBs, likely due to its severely limited channel size that restricts Al<sup>3+</sup> intercalation.

Overall, the ion storage capacity of tunnel-type MnO<sub>2</sub> is strongly influenced by tunnel size. Narrow tunnels, particularly in  $\beta$ - and  $\gamma$ -MnO<sub>2</sub>, limit the intercalation of bulky multivalent ions such as Al<sup>3+</sup>, while  $\alpha$ -MnO<sub>2</sub> shows appreciable Al<sup>3+</sup> storage capacity. To address the inherent diffusion constraints in these tunnel-structured MnO<sub>2</sub>, introducing oxygen vacancies has emerged as an effective strategy to expand ion diffusion pathways and enhance the electrochemical performance of these materials.

**3.1.2 Layered-type manganese oxides.** Compared to tunnel-type MnO<sub>2</sub>, layered  $\delta$ -MnO<sub>2</sub> exhibits larger interlayer spacing ( $\sim$ 0.7 nm), providing a more open framework for ion diffusion and storage. This structure enables the accommodation of more Al<sup>3+</sup> and holds promise for achieving higher specific capacities.

In 2019, Yu *et al.* employed  $\delta$ -MnO<sub>2</sub> as the cathode material for AAIBs.<sup>48</sup> During the initial discharge,  $\delta$ -MnO<sub>2</sub> underwent a conversion reaction, in which Mn<sup>4+</sup> was reduced and dissolved in the electrolyte as Mn<sup>2+</sup>. Upon subsequent charging, the dissolved Mn<sup>2+</sup> was oxidized and combined with Al<sup>3+</sup> to form amorphous Al<sub>x</sub>Mn<sub>1-x</sub>O<sub>2</sub>, which then served as the active material for the following charge/discharge cycles (Fig. 4c). The resulting TAI/2 M Al(OTf)<sub>3</sub>/ $\delta$ -MnO<sub>2</sub> coin cell delivered a capacity of approximately 350 mAh g<sup>-1</sup> at 100 mA g<sup>-1</sup>. Moreover, increasing the Mn<sup>2+</sup> concentration in the electrolyte was shown to facilitate the formation of Al<sub>x</sub>Mn<sub>1-x</sub>O<sub>2</sub> and mitigate further Mn dissolution. By introducing 0.5 M MnSO<sub>4</sub>, the modified cell exhibited a significantly enhanced capacity of 554 mAh g<sup>-1</sup> with a discharge plateau at around 1.35 V and retained 320 mAh g<sup>-1</sup> after 65 cycles, demonstrating improved cycling stability (Fig. 4d). These results highlight the critical role of Mn<sup>2+</sup> in stabilizing the cathode structure and enhancing the electrochemical performance of  $\delta$ -MnO<sub>2</sub>-based AAIBs. In a separate study,  $\delta$ -MnO<sub>2</sub> paired with a Pt-sputtered Al anode in a 5 M Al(OTf)<sub>3</sub> electrolyte also delivered a high capacity of 452 mAh g<sup>-1</sup> at 50 mA g<sup>-1</sup> without any Mn<sup>2+</sup> supplementation.<sup>49</sup>

Although layered  $\delta$ -MnO<sub>2</sub> possesses a large interlayer spacing favorable for Al<sup>3+</sup> transport, its poor structural stability leads to rapid capacity decay during cycling. In the initial charge/discharge process,  $\delta$ -MnO<sub>2</sub> undergoes an irreversible electrochemically induced structural rearrangement with Al<sup>3+</sup> to form a relatively more stable layered amorphous Al<sub>x</sub>MnO<sub>2</sub> phase, which subsequently serves as the active material during cycling and mitigates the excessively strong Al<sup>3+</sup>-MnO<sub>2</sub> interaction in subsequent cycles.<sup>48,50</sup> Inspired by this electrochemical conversion, direct pre-intercalation of Al<sup>3+</sup> has been employed to construct relatively stable layered manganese oxides. For instance, Ran *et al.* synthesized layered Al<sub>x</sub>MnO<sub>2</sub>·nH<sub>2</sub>O cathodes *via* a modified hydrothermal method, which, when coupled with an Al-Cu alloy anode in a 2 M Al(OTf)<sub>3</sub> electrolyte, delivered an initial discharge capacity of approximately 400 mAh g<sup>-1</sup> at 500 mA g<sup>-1</sup>, with 83% capacity retention after 400 cycles.<sup>51</sup>

Similar conversion behavior to layered Al<sub>x</sub>MnO<sub>2</sub> during the first charge-discharge process has also been observed in other Mn oxide cathodes. In 2019, Lu *et al.* reported that Mn<sub>3</sub>O<sub>4</sub> could



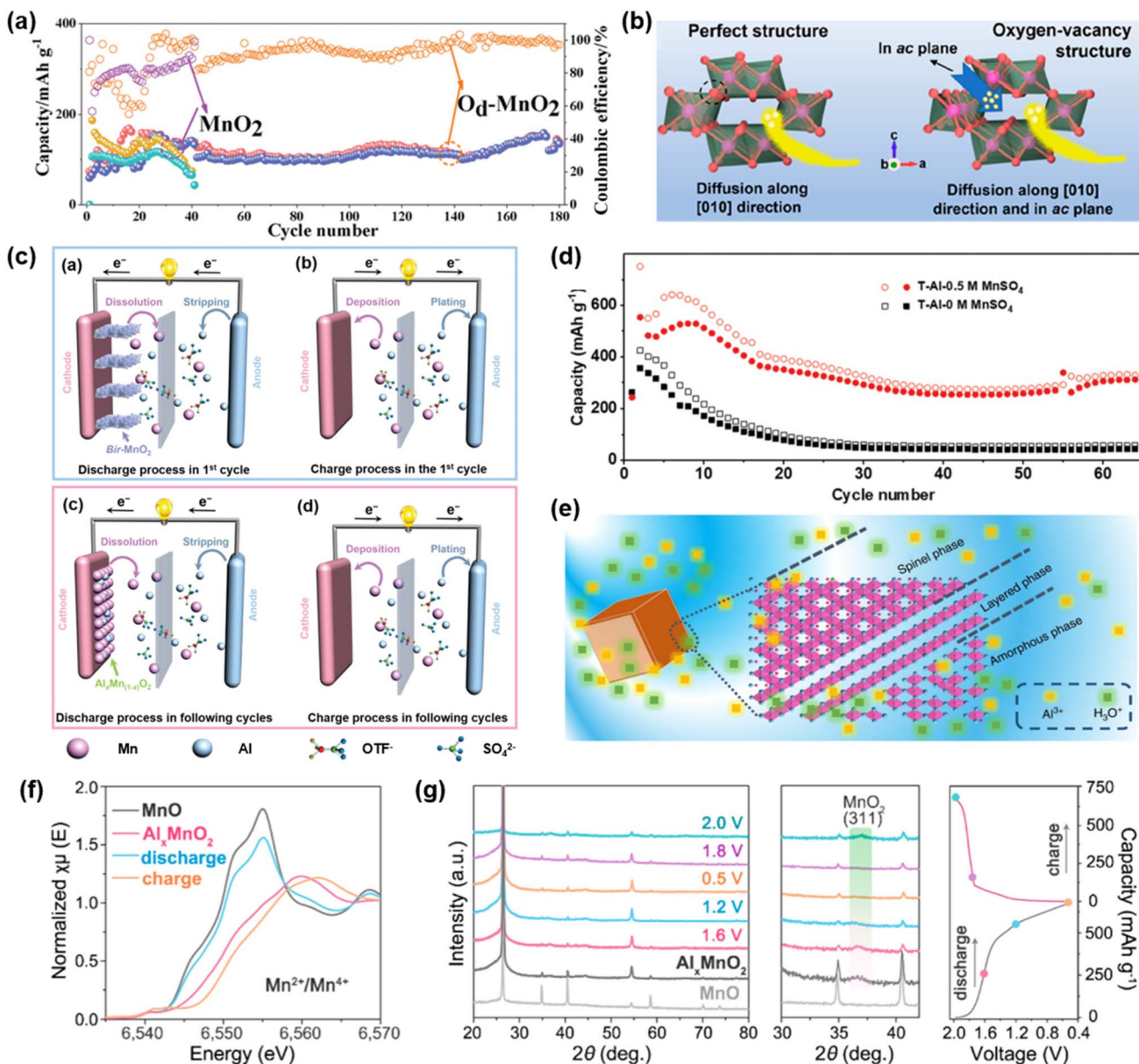


Fig. 4 (a) Cycling performance of  $\text{O}_d\text{-MnO}_2$  and  $\text{MnO}_2$  at  $500 \text{ mA g}^{-1}$ . Reproduced with permission.<sup>46</sup> Copyright 2024, Wiley-VCH. (b) Diffusion of  $\text{H}^+$  into the perfect structure of  $\text{MnO}_2$  and the structure of  $\text{MnO}_2$  with an oxygen vacancy. Reproduced with permission.<sup>47</sup> Copyright 2023, American Chemical Society. (c) The schematic diagram of aluminum–manganese electrochemistry in the first discharge process, the first charge process, and the discharge process and charge process in the following cycles. (d) Cycling performance of T-Al/δ- $\text{MnO}_2$  and T-Al/0.5Mn/δ- $\text{MnO}_2$  batteries. Reproduced with permission.<sup>48</sup> Copyright 2019, Wiley-VCH. (e) The schematic profile of the structure of  $\text{Al}_x\text{MnO}_2\cdot n\text{H}_2\text{O}$ . Reproduced with permission.<sup>52</sup> Copyright 2019, Springer Nature. (f) Mn K-edge XANES spectra of  $\text{Al}_x\text{MnO}_2$  cathodes after full discharge and charge. (g) XRD patterns of  $\text{Al}_x\text{MnO}_2$  cathodes at selected states during the first cycle and typical charge/discharge curves at  $100 \text{ mA g}^{-1}$ . Reproduced with permission.<sup>53</sup> Copyright 2020, American Chemical Society.

be electrochemically converted into a layered  $\text{Al}_x\text{MnO}_2\cdot n\text{H}_2\text{O}$  structure, resulting in a significant enhancement in capacity.<sup>52</sup> During the initial charging process, a portion of  $\text{Mn}^{3+}$  in octahedral sites was oxidized to  $\text{Mn}^{4+}$ , while  $\text{Mn}^{2+}$  in tetrahedral sites and the remaining  $\text{Mn}^{3+}$  in octahedral sites dissolved into the electrolyte, triggering the formation of a layered phase. The dissolved Mn species subsequently reassembled along the edges of the layered domains in the  $\text{Al}(\text{OTf})_3$  electrolyte, forming amorphous regions (Fig. 4e). As a result, the obtained

$\text{Al}_x\text{MnO}_2\cdot n\text{H}_2\text{O}$  exhibits a mixed-phase structure and delivers a high discharge capacity of  $467 \text{ mAh g}^{-1}$  at a current density of  $30 \text{ mA g}^{-1}$ , with a distinct discharge plateau at around  $1.2 \text{ V}$  and a retained capacity of  $272 \text{ mAh g}^{-1}$  after 60 cycles. The superior capacity of  $\text{Al}_x\text{MnO}_2\cdot n\text{H}_2\text{O}$  arises from its layered structure, which enables easier  $\text{Al}^{3+}$  diffusion, and the presence of crystal water, which reduces electrostatic interactions between the  $\text{Al}^{3+}$  and the host anions. Similarly, in 2020, Yan *et al.* employed  $\text{MnO}$  as a precursor, which was electrochemically converted

into a layered  $\text{Al}_x\text{MnO}_2$  phase during the initial charge.<sup>53</sup> The resulting Zn-Al/2 M Al(OTf)<sub>3</sub>/Al<sub>x</sub>MnO<sub>2</sub> coin cell exhibited a high discharge plateau ( $\sim 1.6$  V), a stable reversible capacity (460 mAh g<sup>-1</sup> after 80 cycles at 100 mA g<sup>-1</sup>), and excellent rate performance (100 mAh g<sup>-1</sup> at 3 A g<sup>-1</sup>). *Ex situ* XANES and XRD analyses confirmed the reversible Mn<sup>4+</sup>/Mn<sup>2+</sup> redox behavior and structural evolution during interaction between Al<sup>3+</sup> and the host lattice, providing solid evidence for a reversible Al<sup>3+</sup> storage mechanism in MnO-derived Al<sub>x</sub>MnO<sub>2</sub> (Fig. 4f and g).

In summary, current studies indicate that manganese oxide materials with layered structures offer advantages over tunnel-type structures by providing more space for Al<sup>3+</sup> storage. However, these layered phases are often structurally unstable and undergo a transformation into more stable layered Al<sub>x</sub>MnO<sub>2</sub> phases during the initial charge/discharge process, facilitated by the pre-incorporation of Al<sup>3+</sup> within the host lattice. Despite these advancements, no systematic comparisons have been conducted to determine which type of manganese oxide converts more effectively into Al<sub>x</sub>MnO<sub>2</sub> and delivers better electrochemical performance. The extent of this transformation, including the degree of interaction between Al<sup>3+</sup> and the cathode material and the ratio between the newly formed Al<sub>x</sub>MnO<sub>2</sub> phase and the residual parent phase, remains unclear. In addition, the atomic ratio of Al to Mn in the Al<sub>x</sub>MnO<sub>2</sub> phase, which could reveal the quantitative level of Al<sup>3+</sup> participation in the structure, has yet to be clearly established.

**3.1.3 Modified manganese oxide composites.** Pure-phase  $\delta$ -MnO<sub>2</sub> itself remains intrinsically unstable and tends to transform into Al<sub>x</sub>MnO<sub>2</sub> during the initial cycle. Due to the high charge density of Al<sup>3+</sup>, strong coulombic interactions arise between Al<sup>3+</sup> and the host lattice, leading to sluggish diffusion kinetics and even structural collapse during cycling.<sup>54</sup> The formation of the Al<sub>x</sub>MnO<sub>2</sub> phase partially mitigates these effects by alleviating the excessively strong Al<sup>3+</sup>-MnO<sub>2</sub> interaction in subsequent cycles. However, the resulting Al<sub>x</sub>MnO<sub>2</sub> still suffers from gradual capacity decay and poor cycling stability, primarily due to the remaining strong electrostatic interactions between Al<sup>3+</sup> and the host framework that continues to drive structural degradation over prolonged cycling. To address this, recent studies have explored the incorporation of stabilizing species, including organic molecules and heteroatoms, to further reinforce the structural robustness of  $\delta$ -MnO<sub>2</sub>.

Jiang *et al.* reported a layered manganese oxide cathode pre-intercalated with benzoquinone-coordinated Al<sup>3+</sup> (BQ-Al<sub>x</sub>MnO<sub>2</sub>) (Fig. 5a).<sup>55</sup> In this design, organic benzoquinone (BQ) molecules coordinate with Al<sup>3+</sup> to form BQ-Al<sup>3+</sup> complexes, which are subsequently introduced between MnO<sub>2</sub> layers. This coordination lowers the effective charge of Al<sup>3+</sup>, weakening its electrostatic interaction with the host lattice and facilitating reversible Al<sup>3+</sup>-host intercalation. Simultaneously, the co-intercalation of BQ-Al<sup>3+</sup> complexes expands the interlayer spacing of MnO<sub>2</sub>, further improving ion transport and structural stability. As a result, the BQ-Al<sub>x</sub>MnO<sub>2</sub> cathode, paired with a Zn<sub>50</sub>Al<sub>50</sub> alloy anode and a mixed electrolyte of 2 M Al(OTf)<sub>3</sub> and 0.2 M Mn(OTf)<sub>2</sub>, exhibited outstanding electrochemical performance. The assembled coin cell delivered a discharge capacity of 300 mAh g<sup>-1</sup> at a current density of 1 A g<sup>-1</sup> and maintained  $\sim 99\%$  of

its capacity after over 800 cycles, demonstrating both high capacity and cycling stability. In addition to organic molecule intercalation, cation pre-intercalation has also proven effective in stabilizing layered MnO<sub>2</sub> frameworks and enhancing electrochemical kinetics. For instance, Cu<sup>2+</sup> pre-intercalated  $\delta$ -MnO<sub>2</sub> synthesized *via* a simple hydrothermal method exhibited a high discharge capacity of 363.4 mAh g<sup>-1</sup> at 400 mA g<sup>-1</sup> and retained 164.5 mAh g<sup>-1</sup> of its capacity after 300 cycles.<sup>56</sup> The incorporated Cu<sup>2+</sup> increased the electronegativity of lattice oxygen, moderated the strong electrostatic interaction with Al<sup>3+</sup> and optimized H<sup>+</sup> adsorption energy, thereby enhancing proton participation and maintaining the layered structure.

Metal cation substitution, especially with aliovalent ions, can simultaneously tailor the host structure and introduce charge carriers (holes or electrons) to maintain charge neutrality, thereby enhancing the structural stability of the cathode material.<sup>57,58</sup> Building on this concept, Geng *et al.* developed a defective cobalt-substituted layered manganese oxide ( $\delta$ -MnO<sub>2</sub>) as a cathode material for AAIBs (Fig. 5b and c).<sup>59</sup> The synergistic effect between the incorporated Co atoms and Mn vacancies improved the electrical conductivity, facilitated Al<sup>3+</sup> diffusion, and effectively suppressed Mn dissolution during cycling (Fig. 5d). As a result, the assembled battery exhibited a high specific capacity of 585 mAh g<sup>-1</sup> at a current density of 100 mA g<sup>-1</sup>, with 78% capacity retention after 300 cycles. However, the Co-doped  $\delta$ -MnO<sub>2</sub> exhibited relatively poor rate capacity, delivering only 185 mAh g<sup>-1</sup> at a high current density of 500 mA g<sup>-1</sup>. To improve this, our group introduced metal heteroatoms with higher metal–oxygen bond dissociation energies, such as V and Ti, to reinforce the  $\delta$ -MnO<sub>2</sub> framework while expanding the interplanar spacing (Fig. 5e and f).<sup>60</sup> The enlarged interlayer spacing reduces diffusion resistance and accelerates Al<sup>3+</sup> transport and adsorption, resulting in enhanced rate performance. Meanwhile, the stronger metal–oxygen bonds improve structural stability and suppress Mn dissolution. As a result, the V-doped  $\delta$ -MnO<sub>2</sub> cathode achieved a high reversible capacity of 518 mAh g<sup>-1</sup> at 200 mA g<sup>-1</sup> with 86% capacity retention over 400 cycles. Moreover, its rate performance was significantly improved, delivering 468, 339, and 285 mAh g<sup>-1</sup> at 0.5, 1, and 2 A g<sup>-1</sup>, respectively.

Another strategy to enhance the structural stability and electrochemical performance of MnO<sub>2</sub> cathodes is the composite approach. By integrating MnO<sub>2</sub> with other functional materials such as conductive carbon, the resulting hybrid structures can enhance structural stability, suppress manganese dissolution, stabilize oxygen vacancies, or provide additional active sites for ion storage.<sup>32,61</sup> For instance, a hybrid  $\alpha$ -MnO<sub>2</sub> cathode with Al<sup>3+</sup> pre-insertion and g-C<sub>3</sub>N<sub>4</sub> was developed, where Al<sup>3+</sup> expands the tunnel structures and reduces strain during intercalation, while g-C<sub>3</sub>N<sub>4</sub> occupies oxygen vacancies and forms Mn–N bonds with the MnO<sub>6</sub> lattice.<sup>62</sup> This dual modification not only improves structural robustness but also significantly enhances electrochemical performance, delivering an excellent capacity of 329.25 mAh g<sup>-1</sup> at 0.5 A g<sup>-1</sup> and a rate capability of 137.67 mAh g<sup>-1</sup> at 1.5 A g<sup>-1</sup>, highlighting the effectiveness of composite engineering in stabilizing MnO<sub>2</sub> cathodes for AAIBs.



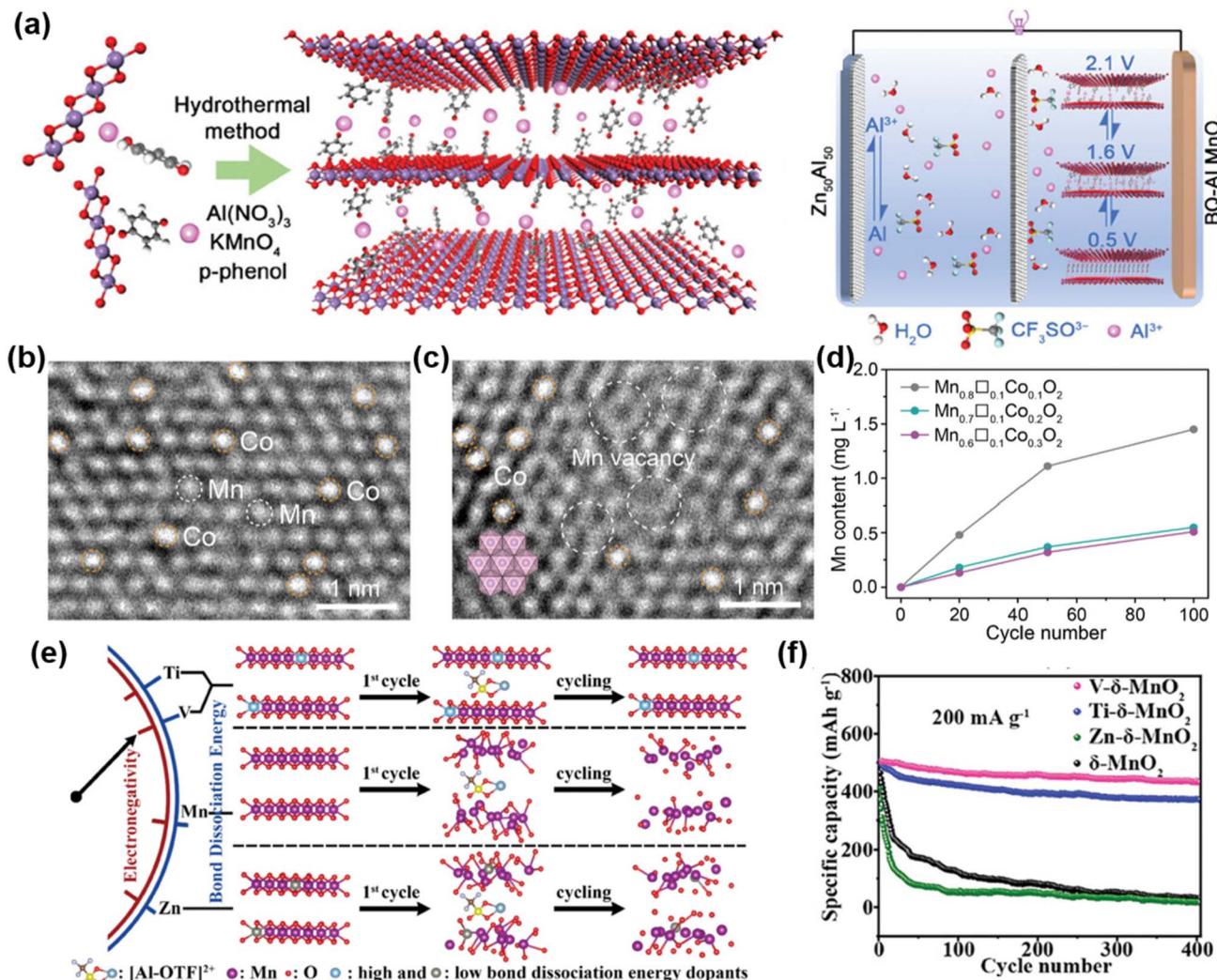


Fig. 5 (a) Schematic illustration of preparation of layered BQ-Al<sub>x</sub>MnO<sub>2</sub> by a hydrothermal method, during which highly coordinated BQ-Al<sup>3+</sup> pre-intercalated in MnO<sub>2</sub> layers, and the scheme of an aqueous AlB full cell that is composed of a Zn<sub>50</sub>Al<sub>50</sub> alloy anode and titanium foil-supported BQ-Al<sub>x</sub>MnO<sub>2</sub> cathode, with 2 M Al(OTf)<sub>3</sub> solution as aqueous electrolyte. Reproduced with permission.<sup>55</sup> Copyright 2024, Wiley-VCH. Atomic-resolution HAADF-STEM images of (b) Mn<sub>0.8</sub>Co<sub>0.2</sub>O<sub>2</sub> and (c) acid-coagulated Mn<sub>0.7</sub>□<sub>0.1</sub>Co<sub>0.2</sub>O<sub>2</sub>. Inset: the hexagonal arrangement of Mn atoms in ideal MnO<sub>2</sub> sheets. (d) ICP-AES measurement of dissolved manganese in 2 M Al(OTf)<sub>3</sub> electrolyte after different numbers of cycles. Reproduced with permission.<sup>59</sup> Copyright 2023, Wiley-VCH. (e) Schematic illustration of the impact of heteroatom doping on the electrochemical stability and performance of δ-MnO<sub>2</sub> cathodes during AAIB cycling. (f) Electrochemical cycling performances of pristine and doped δ-MnO<sub>2</sub> cathodes at 200 mA g<sup>-1</sup>. Reproduced with permission.<sup>60</sup> Copyright 2024, Wiley-VCH.

Overall, tunnel-type MnO<sub>2</sub> cathodes suffer from limited capacity due to their narrow channels, whereas layered δ-MnO<sub>2</sub> offers greater interlayer spacing, making it a more promising host for Al<sup>3+</sup> storage. However, the layered structure is inherently unstable and typically undergoes an *in situ* transformation into an Al<sub>x</sub>MnO<sub>2</sub> phase during the initial charge/discharge cycle. In addition to δ-MnO<sub>2</sub>, other manganese oxides such as MnO and spinel-type Mn oxides can also be electrochemically converted into Al<sub>x</sub>MnO<sub>2</sub> during initial cycling. Nevertheless, the stability of the resulting Al<sub>x</sub>MnO<sub>2</sub> remains limited. Therefore, recent research has focused on interlayer engineering strategies, such as organic molecule intercalation, metal-ion pre-intercalation, and heteroatom doping, to stabilize or enlarge the interlayer spacing and suppress structural degradation.

These methods aim to preserve the advantageous layered framework while enhancing both the cycling stability and rate performance of Mn-based cathodes. Future research could further refine and integrate these strategies to develop high-performance and durable manganese-based cathode materials for AAIBs.

### 3.2 Vanadium-based cathode materials

Metallic vanadium, with its wide range of oxidation states from +2 to +5, enables multi-electron transfer and thus delivers high capacities, making vanadium-based compounds an important class of cathode materials. Vanadium-based compounds include vanadium oxides, vanadates, and vanadium phosphates. Among them, vanadium oxides are the most widely



studied. Owing to the variable oxidation states of vanadium, vanadium oxides exhibit diverse crystal structures, primarily including orthorhombic layered  $V_2O_5$ , bilayer  $V_2O_5 \cdot nH_2O$  and  $V_3O_7 \cdot H_2O$ , and monoclinic tunnel-structured  $VO_2$ ,  $V_6O_{13}$ , and  $V_2O_3$ . Vanadates, generally denoted as  $M_xV_nO_m$  (where  $M$  represents metal cations or ammonium ions), are derived from the pre-intercalation of metal ions into vanadium oxides. Such pre-intercalation is beneficial for enhancing the structural stability of vanadium oxides. Vanadium phosphates are constructed from  $[PO_4]$  tetrahedra and  $[VO_6]$  octahedra, forming a three-dimensional open framework. They typically exhibit a robust structural framework and remarkable thermal stability and good structural integrity during ion insertion/extraction. However, the separation of  $[VO_6]$  octahedra by phosphate groups leads to intrinsically low electronic conductivity. The variations in crystal structures and chemical compositions among these vanadium-based compounds lead to differences in electrochemical performance, which provides both opportunities and challenges for their application as cathodes in AAIBs.

**3.2.1 Vanadium oxides.** In 2016, González *et al.* first employed  $V_2O_5$  as a cathode material for AAIBs and explored the possibility of  $Al^{3+}$  intercalation into  $V_2O_5$ .<sup>63</sup> Using a three-electrode configuration in 1 M  $AlCl_3$  electrolyte, they found that during discharge,  $V_2O_5$  irreversibly transformed into amorphous  $Al_xV_2O_5$ . The amorphous structure facilitated dynamic chemical interactions with  $Al^{3+}$ -containing electrolyte species, thereby enhancing the charge storage capacity.

Subsequently, in 2020, Zhao *et al.* proposed that in AAIBs, protons can reversibly interact with  $V_2O_5$ , whereas direct  $Al^{3+}$  participation is difficult.<sup>38</sup> By tuning electrolyte composition and pH, they regulated  $H^+$  intercalation selectivity (Fig. 6a). In 2 M  $Al(OTf)_3$  acidic electrolyte,  $V_2O_5$  delivered a discharge capacity of  $\sim 200 \text{ mAh g}^{-1}$  at  $20 \text{ mA g}^{-1}$ , with a discharge plateau at around 0.9 V and  $120 \text{ mAh g}^{-1}$  remaining after 50 cycles (Fig. 6b). DFT calculations revealed that proton insertion induced a structural transformation from orthorhombic layered  $V_2O_5$  to a triclinic phase, accompanied by reductions in both interlayer spacing and volume. The insertion of one proton could deliver  $\sim 147 \text{ mAh g}^{-1}$  with good structural stability, whereas insertion of two protons increased the capacity to  $296 \text{ mAh g}^{-1}$  but caused significant volume contraction and severe structural degradation (Fig. 6c). These studies clarified the ion storage behavior in  $V_2O_5$ , though the dominant mechanism remains under debate.

To enhance the electrochemical performance of  $V_2O_5$ , in 2023, De *et al.* synthesized interconnected nanosheet-structured  $V_2O_5$  *via* a hydrothermal method using  $NH_4VO_3$  followed by high-temperature calcination.<sup>64</sup> This two-dimensional nanosheet architecture increased the electrode–electrolyte contact area, facilitating rapid ion diffusion. In a three-electrode setup with 0.5 M  $AlCl_3$  electrolyte, the electrode delivered an initial discharge capacity of  $\sim 140 \text{ mAh g}^{-1}$  at  $0.5 \text{ A g}^{-1}$  and maintained 96% of its capacity after 1000 cycles at  $1 \text{ A g}^{-1}$  (Fig. 6d). The excellent capacity retention and rate performance were attributed to the high specific surface area provided by the interconnected nanosheet structure, which promoted ion

accumulation at the electrode–electrolyte interface, enhancing the electric double-layer contribution to the total capacity.

Introducing oxygen vacancies is another effective strategy. Wang *et al.* introduced oxygen vacancies ( $O_v$ ) into  $V_2O_5$  *via* oxalic acid treatment.<sup>65</sup> The resulting  $O_v\text{-}V_2O_5$  exhibited a high initial capacity of  $400 \text{ mAh g}^{-1}$  at  $0.4 \text{ A g}^{-1}$  in 5 M  $Al(OTf)_3$  electrolyte, nearly double that of pristine  $V_2O_5$  ( $\sim 200 \text{ mAh g}^{-1}$ ) (Fig. 6e). Theoretical calculations indicated that  $O_v\text{-}V_2O_5$  had lower adsorption energies for both  $H^+$  and  $Al^{3+}$  compared with pristine  $V_2O_5$ , implying reduced diffusion barriers and accelerated ion transport. Although oxygen vacancies improved cycling stability (Fig. 6f), the capacity of  $O_v\text{-}V_2O_5$  still declined to  $103 \text{ mAh g}^{-1}$  after 200 cycles, indicating rapid fading.

Besides defect engineering, compositing with conductive materials has also been investigated to improve the electrochemical performance of  $V_2O_5$ . Yang *et al.* fabricated a  $V_2O_5\text{@}MXene$  composite cathode by depositing rod-like  $V_2O_5$  onto monolayer MXene.<sup>66</sup> In 5 M  $Al(OTf)_3$  electrolyte, the composite exhibited a wide voltage window (0.1–2.4 V) and an exceptionally high initial capacity of  $626 \text{ mAh g}^{-1}$  at  $100 \text{ mA g}^{-1}$  (Fig. 6g). Compared with pristine  $V_2O_5$ , the composite demonstrated approximately twice the cycle life, improved coulombic efficiency, and retained  $200 \text{ mAh g}^{-1}$  after 100 cycles at  $400 \text{ mA g}^{-1}$  (Fig. 6h). The enhanced performance was attributed to the excellent electrical conductivity and pseudocapacitive characteristics of MXene, which improved electron transport, ion diffusion, and electrode stability.

In summary, layered  $V_2O_5$  enables reversible interactions with  $Al^{3+}$  or  $H^+$  in AAIBs but suffers from limited capacity and structural instability. Although defect engineering and conductive composite design have improved capacity and cycle life, capacity fading remains significant. Therefore, stabilizing the crystal structure and enhancing the reversible ion storage are critical directions for the future development of  $V_2O_5$ -based cathodes.

Compared with layered  $V_2O_5$ , tunnel-type vanadium oxides generally exhibit higher lattice stability during repeated ion–host interaction, which is beneficial for achieving long cycle life.<sup>67,68</sup> Among them, the most representative is the metastable monoclinic bronze-type vanadium dioxide ( $VO_2(B)$ ), whose crystal structure consists of alternating  $[VO_6]$  octahedra and tetrahedra, forming characteristic one-dimensional diffusion tunnels. The tunnel size ( $4.984 \text{ \AA} \times 3.281 \text{ \AA}$ ) is significantly larger than the ionic radius of  $Al^{3+}$  ( $0.53 \text{ \AA}$ ), thus providing sufficient space for guest ion transport and storage.

Recent studies have further optimized the  $VO_2$  structure to enhance its electrochemical performance in AAIBs. In 2020, Cai *et al.* synthesized porous  $VO_2(B)$  nanobelts *via* a hydrothermal method and employed them as cathode materials for AAIBs.<sup>69</sup> The robust  $VO_2(B)$  framework effectively resisted lattice shear during cycling, while the porous nanobelt morphology shortened ion diffusion pathways and increased electrode–electrolyte contact area. As a result, the electrode delivered a specific capacity of  $234 \text{ mAh g}^{-1}$  at  $150 \text{ mA g}^{-1}$  and retained 77.2% of its capacity after 1000 cycles at  $1 \text{ A g}^{-1}$  in a three-electrode system with 5 M  $Al(OTf)_3$  electrolyte (Fig. 7a and b). In another study, Wang *et al.* reported that the unique interconnected tunnel



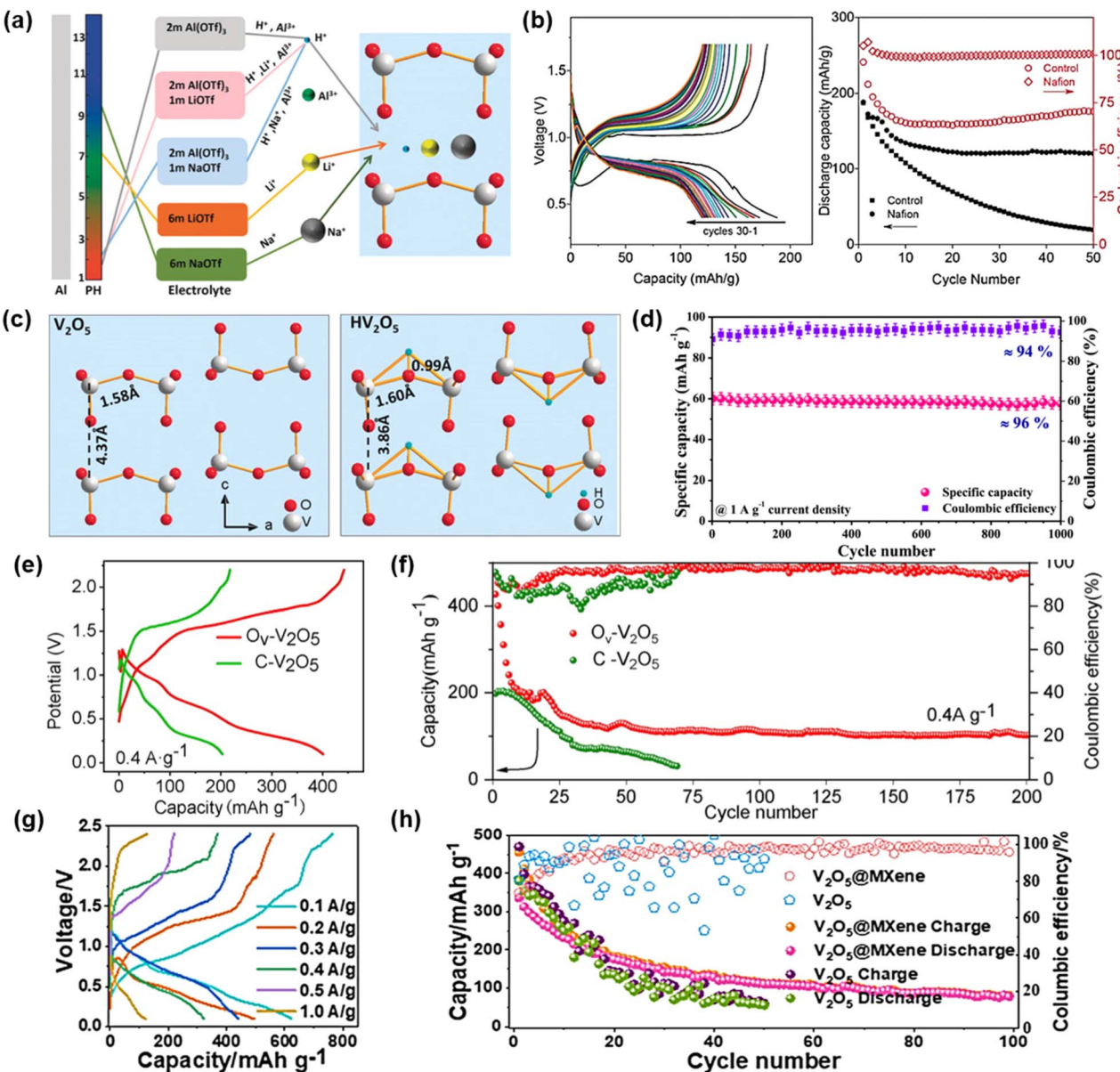


Fig. 6 (a) Different cation intercalating behaviors of  $\text{V}_2\text{O}_5$  through regulating the electrolytes. (b) Galvanostatic discharge/charge profiles of aqueous  $\text{Al}/\text{V}_2\text{O}_5$  batteries using a Nafion modified separator and corresponding cycling performance and coulombic efficiency. (c) Structure of pristine  $\text{V}_2\text{O}_5$  and  $\text{V}_2\text{O}_5$  after proton insertion. Reproduced with permission.<sup>38</sup> Copyright 2020, Wiley-VCH. (d) Cycling stability performance of the synthesized  $\text{V}_2\text{O}_5$  material. Reproduced with permission.<sup>64</sup> Copyright 2023, American Chemical Society. (e) The initial GCD curves for  $\text{O}_v\text{-V}_2\text{O}_5$  and  $\text{C-V}_2\text{O}_5$  at  $0.4\text{ A g}^{-1}$  and (f) cycling performance at  $0.4\text{ A g}^{-1}$ . Reproduced with permission.<sup>65</sup> Copyright 2025, Elsevier. (g) Rate performance of  $\text{V}_2\text{O}_5\text{@MXene}$  and (h) comparison of the cycle performance between  $\text{V}_2\text{O}_5\text{@MXene}$  and  $\text{V}_2\text{O}_5$  at  $0.4\text{ A g}^{-1}$ . Reproduced with permission.<sup>66</sup> Copyright 2024, American Chemical Society.

structure of monoclinic  $\text{VO}_2$  enabled rapid  $\text{Al}^{3+}$  diffusion while effectively mitigating volume changes, achieving  $235\text{ mAh g}^{-1}$  at  $200\text{ mA g}^{-1}$  and retaining 49.3% of its capacity when the current density increased to  $2\text{ A g}^{-1}$  (Fig. 7c).<sup>70</sup>

More recently, in 2025, Wang *et al.* achieved both a compositional transformation from  $\text{V}_2\text{O}_5$  to  $\text{VO}_2$  and a crystallographic transition from the orthorhombic to the monoclinic phase *via* glucose-assisted hydrothermal reduction, while simultaneously introducing  $\text{Cu}^{2+}$  doping (Fig. 7d).<sup>71</sup> The introduced  $\text{Cu}$  3d orbitals enhanced the hybridization between  $\text{V}$  3d and  $\text{O}$  2p

orbitals and strengthened electronic coupling, optimizing the band structure and improving both ion and electron transport. At an optimal  $\text{Cu}$  content of 1 mmol, the resulting  $\text{VO}_2$  cathode, paired with 5 M  $\text{Al}(\text{OTf})_3$  electrolyte and an ionic-liquid-treated  $\text{Al}$  anode, delivered an initial discharge capacity of  $642\text{ mAh g}^{-1}$  at  $0.4\text{ A g}^{-1}$  and maintained  $116\text{ mAh g}^{-1}$  after 200 cycles at  $0.8\text{ A g}^{-1}$  (Fig. 7e and f), outperforming pristine  $\text{VO}_2$  in both capacity and cycling stability.

In summary,  $\text{VO}_2\text{(B)}$  demonstrates considerable potential for AAIB applications owing to its spacious tunnel structure.

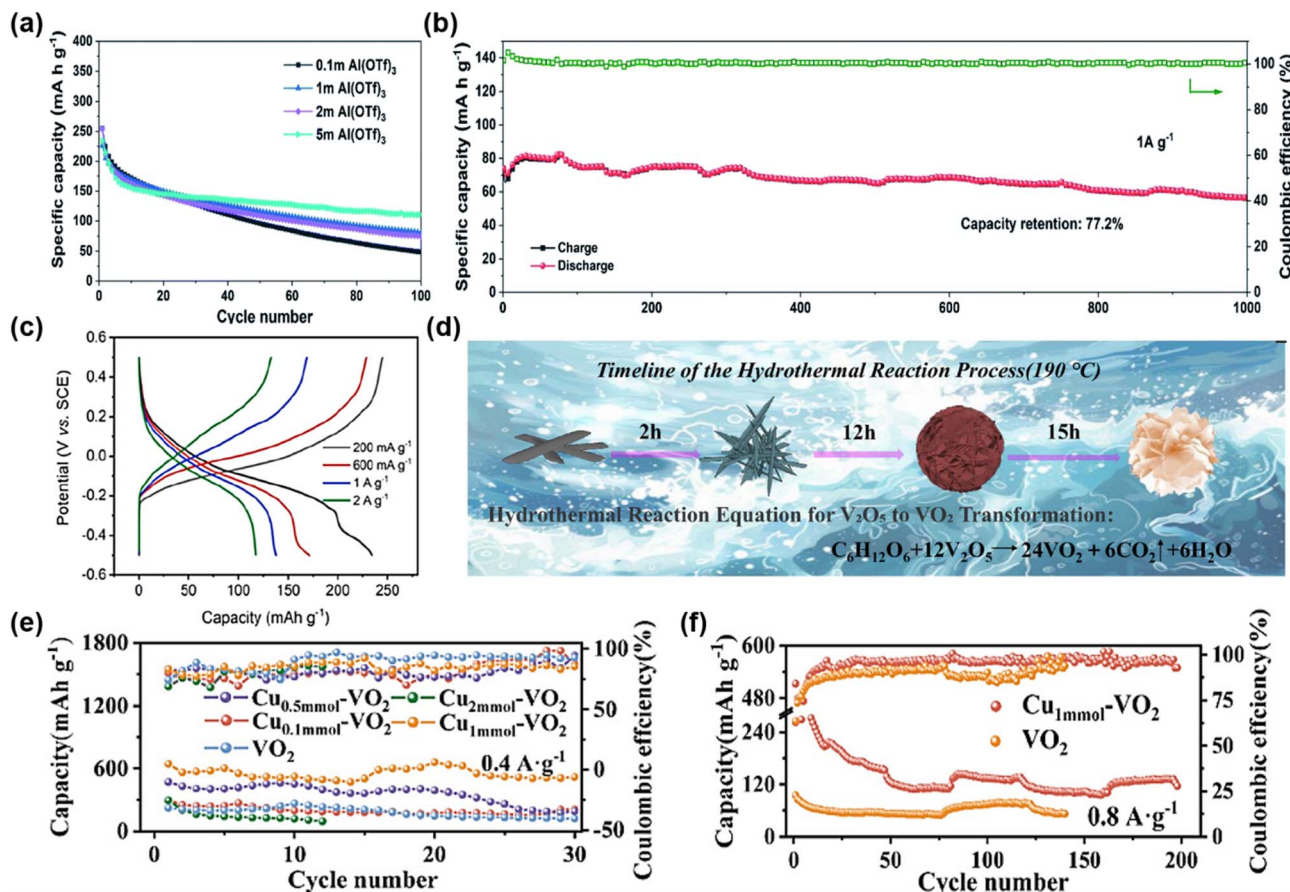


Fig. 7 (a) Cycling performances of the VO<sub>2</sub>-B electrodes in the Al(OTf)<sub>3</sub> electrolytes with different concentrations at 150 mA g<sup>-1</sup>. (b) Long-term cycling performance of the VO<sub>2</sub>-B electrodes at 1 A g<sup>-1</sup> in the 5 M Al(OTf)<sub>3</sub> electrolyte. Reproduced with permission.<sup>69</sup> Copyright 2020, Royal Society of Chemistry. (c) GCD curve of VO<sub>2</sub> at different current densities. Reproduced with permission.<sup>70</sup> Copyright 2021, Elsevier. (d) Schematic diagram of preparation and morphology evolution of Cu<sub>1mmol</sub>-VO<sub>2</sub>. (e) Cycling performance at 0.4 A g<sup>-1</sup>. (f) Cycling performance of VO<sub>2</sub> and Cu<sub>0.5mmol</sub>-VO<sub>2</sub> at 0.8 A g<sup>-1</sup>. Reproduced with permission.<sup>71</sup> Copyright 2025, Wiley-VCH.

However, unlike layered vanadium oxides, where interlayer spacing can be tuned to enhance ion diffusion kinetics, the tunnel dimensions of VO<sub>2</sub> are relatively fixed, restricting further improvement in ion diffusion kinetics. Therefore, effective strategies to accelerate ion migration within the tunnels are urgently needed. Current strategies, including nanostructure design to shorten diffusion paths and doping to optimize the electronic structure, have enhanced performance. Nevertheless, there remains substantial room for improvement in their long-term cycling stability and high-rate capability.

**3.2.2 Vanadates.** Due to the flexible distortion of V-O polyhedra and the multiple oxidation states of vanadium, V-O frameworks exhibit high structural adaptability toward the incorporation of foreign metal cations and ammonium ions, giving rise to a wide variety of vanadates. These materials can be regarded as derivatives formed by the combination of vanadium oxides with additional ions or clusters. Typically, the introduced cations act as “pillars” within the framework, enhancing interlayer stability and improving ion transport kinetics, thereby boosting electrochemical performance.

In 2022, Soundharrajan *et al.* reported the application of LiV<sub>3</sub>O<sub>8</sub> cathodes in AAIBs.<sup>72</sup> The presence of Li<sup>+</sup> in its layered

structure can mitigate the strong coulombic attraction between Al<sup>3+</sup> and the host lattice, thereby facilitating Al<sup>3+</sup> diffusion kinetics (Fig. 8a). In 2 M Al(OTf)<sub>3</sub> electrolyte, LiV<sub>3</sub>O<sub>8</sub> delivered a high capacity of 289 mAh g<sup>-1</sup> at 0.29C and maintained 147 mAh g<sup>-1</sup> after 500 cycles at 0.59C, corresponding to a capacity retention of 77.3% (Fig. 8b and c).

In 2023, Liu *et al.* for the first time applied NH<sub>4</sub>V<sub>4</sub>O<sub>10</sub> as a cathode for AAIBs.<sup>73</sup> The large and lightweight NH<sub>4</sub><sup>+</sup> act as pillars in the crystal structure, expanding the interlayer spacing and promoting fast ion transport. As a result, the layered NH<sub>4</sub>V<sub>4</sub>O<sub>10</sub> achieved 257.78 mAh g<sup>-1</sup> at 0.5 A g<sup>-1</sup> in 2 M Al(OTf)<sub>3</sub> and retained 87.80 mAh g<sup>-1</sup> even at a high current density of 5 A g<sup>-1</sup> (Fig. 8d). Subsequent work further examined electrolyte optimization for the NH<sub>4</sub>V<sub>4</sub>O<sub>10</sub> cathode material. Radhakantha *et al.* demonstrated that adding 0.5 M NH<sub>4</sub>Cl to 1 M AlCl<sub>3</sub> electrolyte effectively suppressed vanadium dissolution.<sup>74</sup> The first-cycle capacity decay decreased from 84% to 32%, and the electrolyte color changed from deep yellow to light yellow (Fig. 8e and f), indicating that the additive suppressed V dissolution and improved structural stability.

In addition, Wu *et al.* prepared (NH<sub>4</sub>)<sub>2</sub>V<sub>10</sub>O<sub>25</sub>·8H<sub>2</sub>O/Ti<sub>3</sub>C<sub>2</sub>T<sub>x</sub> composites *via* van der Waals self-assembly.<sup>75</sup> The

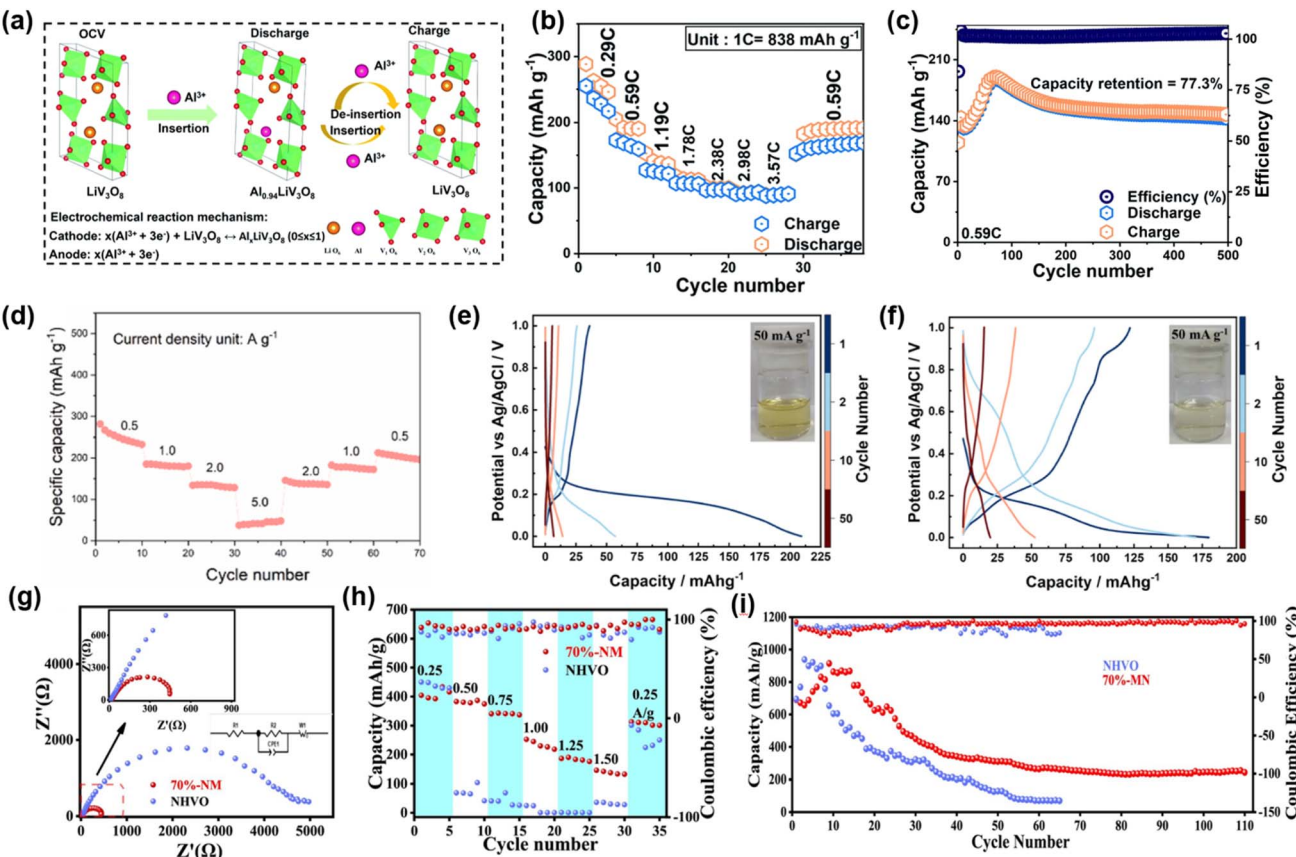


Fig. 8 (a) Schematic representation of the  $\text{Al}^{3+}$  storage properties of the  $\text{LiV}_3\text{O}_8$  cathode during the charge and discharge course. (b) Rate performances of  $\text{LiV}_3\text{O}_8$  at different current densities and (c) cycle life curve at 0.59C. Reproduced with permission.<sup>72</sup> Copyright 2022, Royal Society of Chemistry. (d) Rate tests of layered  $\text{NH}_4\text{V}_4\text{O}_{10}$  nanosheets at sets of current densities from 0.5 to 5  $\text{A g}^{-1}$ . Reproduced with permission.<sup>73</sup> Copyright 2023, Elsevier. (e and f) GCD (current density = 50  $\text{mA g}^{-1}$ ) profile of  $\text{NH}_4\text{V}_4\text{O}_{10}$  electrodes cycled in 1 M  $\text{AlCl}_3$  (e) and 1 M  $\text{AlCl}_3$  + 0.5 M  $\text{NH}_4\text{Cl}$  (f) electrolytes, respectively. Reproduced with permission.<sup>74</sup> Copyright 2024, American Chemical Society. (g) Multiplicity curve of 70%-NM ( $(\text{NH}_4)_2\text{V}_{10}\text{O}_{25} \cdot 8\text{H}_2\text{O}/\text{Ti}_3\text{C}_2\text{T}_x$  composites). (h) Rate performance of 70%-NM and NHVO ( $(\text{NH}_4)_2\text{V}_{10}\text{O}_{25} \cdot 8\text{H}_2\text{O}$ ). (i) Cycling performance graphs for 70%-NM and NHVO. Reproduced with permission.<sup>75</sup> Copyright 2024, Elsevier.

incorporation of MXene reduced the charge-transfer resistance to one-tenth that of the pristine material and significantly enhanced both rate capability and cycling stability (Fig. 8g and h). At 1.0  $\text{A g}^{-1}$ , the electrode maintained 268.7  $\text{mAh g}^{-1}$  after 110 cycles (Fig. 8i). This result indicates that MXene not only accelerates ion transport but also acts as a mechanical support to stabilize structure during cycling, highlighting the advantages of composite design.

**3.2.3 Vanadium phosphates.** Vanadium phosphates are composed of  $[\text{VO}_6]$  octahedra and  $[\text{PO}_4]$  tetrahedra, forming a three-dimensional open framework with excellent crystallographic stability and can maintain structural integrity during cycling. The presence of  $[\text{PO}_4]$  tetrahedra introduces a P–O covalency-induced effect, which weakens the V–O covalent bonds, thereby endowing vanadium phosphates with relatively high redox potentials.<sup>76</sup> However, similar to other phosphate-based electrodes, the  $[\text{VO}_6]$  octahedra are isolated from each other by intervening  $[\text{PO}_4]$  tetrahedra, which hinders electron transport pathways and results in intrinsically low electrical conductivity.<sup>77</sup>

In 2018, Nacimento *et al.* first applied NASICON-type  $\text{Na}_3\text{V}_2(\text{PO}_4)_3$  as a cathode for rechargeable aluminum batteries, delivering a reversible capacity of 60–100  $\text{mAh g}^{-1}$  at current densities ranging from 10 to 1000  $\text{mA g}^{-1}$  in a three-electrode configuration with  $\text{AlCl}_3$ -based electrolyte (Fig. 9a).<sup>78</sup> In 2020, Wang *et al.* employed  $\text{VOPO}_4$  as the cathode and incorporated a mechanically robust gelatin–polyacrylamide hydrogel electrolyte to construct a flexible AAIB, achieving a capacity of 88  $\text{mAh g}^{-1}$  at 0.8  $\text{A g}^{-1}$  and maintaining 22  $\text{mAh g}^{-1}$  even at a high rate of 6  $\text{A g}^{-1}$  (Fig. 9b).<sup>79</sup> Remarkably, this device retained 86.2% of its initial capacity after 2800 cycles at 1  $\text{A g}^{-1}$  (Fig. 9c), demonstrating excellent cycling stability and mechanical flexibility. Subsequently, Pang *et al.* utilized layered  $\text{VOPO}_4 \cdot 2\text{H}_2\text{O}$  nanosheets as a cathode material for AAIBs, achieving reversible trivalent  $\text{Al}^{3+}$  storage in 2.5 M  $\text{Al}(\text{OTf})_3$  electrolyte.<sup>80</sup> At a current density of 20  $\text{mA g}^{-1}$ , the material delivered an initial discharge capacity of 125.4  $\text{mAh g}^{-1}$  with an operating voltage of  $\sim 0.9$  V, retaining 60% of its capacity after 40 cycles (Fig. 9d and e), highlighting its cycling stability and application potential. More recently, Liu *et al.* demonstrated that phenylamine intercalation can effectively expand the

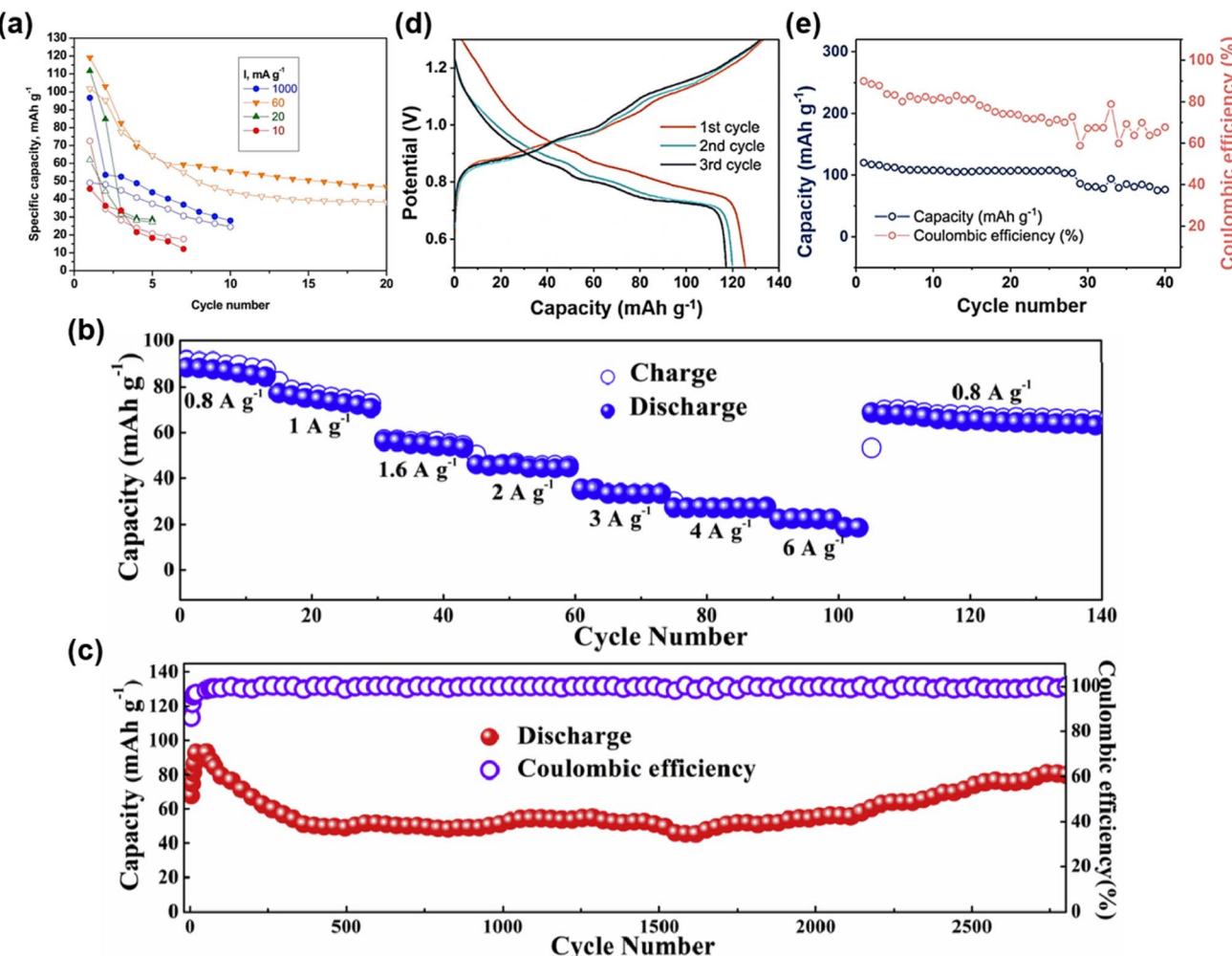


Fig. 9 (a) Capacity–cycle number at several rates of Na<sub>3</sub>V<sub>2</sub>(PO<sub>4</sub>)<sub>3</sub> (charge: open symbols; discharge: closed symbols). Reproduced with permission.<sup>78</sup> Copyright 2018, Elsevier. (b) Rate capability at various rates and (c) long-term cycling performance and the corresponding coulombic efficiency at 1 A g<sup>-1</sup> of the rechargeable solid-state aqueous AlIB. Reproduced with permission.<sup>79</sup> Copyright 2020, Elsevier. (d) First three charge/discharge curves and (e) cycling performance of VOPO<sub>4</sub>·2H<sub>2</sub>O/Al metal batteries at a current density of 20 mA g<sup>-1</sup>. Reproduced with permission.<sup>80</sup> Copyright 2021, Elsevier.

interlayer spacing of VOPO<sub>4</sub>, enabling high-capacity and long-life Al<sup>3+</sup> storage in aqueous batteries.<sup>81</sup>

Overall, the capacities and operating voltages of vanadium-based cathodes in AAIBs are generally lower than those of their manganese-based counterparts, primarily due to their intrinsic structural and electronic limitations, including relatively low electrical conductivity and suboptimal ion transport pathways. Future research should focus on improving the capacity, stability, and conductivity through strategies such as nanostructure engineering, conductive network construction, and doping modifications, while combining *in situ* characterization with theoretical calculations to gain deeper insights into their energy storage mechanisms.

### 3.3 Prussian blue analogs

Prussian blue analogs (PBAs) were first discovered in the 18th century and widely employed as dyes. It was not until 2011 that Cui *et al.* first utilized KNi-PB as a cathode material for

potassium-ion batteries, followed by their report on the application of KCu-PB in lithium-ion batteries.<sup>82,83</sup> These pioneering studies not only broadened the application scope of PBAs in rechargeable ion batteries but also revealed their great potential as cathode materials.

PBAs are generally represented by the formula A<sub>x</sub>M[ M'(CN)<sub>6</sub>]<sub>1-x</sub>·□<sub>y</sub>·nH<sub>2</sub>O (0 < x < 2), where A denotes alkali metal ions (commonly K, Na, or Li), M corresponds to N-coordinated transition metal ions, M' refers to C-coordinated transition metal ions (most commonly Fe), and □ represents vacancies arising from the loss of M'(CN)<sub>6</sub> units and the occupation by coordination water.<sup>84,85</sup> Prussian blue and its analogues are often abbreviated as AM-PB. In AM-PB, the Fe<sup>2+</sup>/Fe<sup>3+</sup> redox couple at the M'-site metal generally serves as the dominant redox pair. When the M-site metal is also electrochemically active (*e.g.*, Fe, Co, and Mn), an additional M<sup>2+</sup>/M<sup>3+</sup> redox couple is introduced, enabling two redox-active centers and thus a higher theoretical capacity. In contrast, when M is electrochemically



inactive (*e.g.*, Ni, Cu, and Zn), only the  $\text{Fe}^{2+}/\text{Fe}^{3+}$  redox couple contributes to charge storage, resulting in a lower theoretical capacity.<sup>86</sup>

The ideal PBA structure adopts a face-centered cubic framework with a lattice parameter of  $\sim 10.2$  Å (Fig. 10a). In this structure,  $\text{C}\equiv\text{N}$  groups are located along the cube edges, where M and M' ions form octahedral coordination with N and C atoms of cyanide ligands respectively, constructing a three-dimensional open framework. The interstitial sites between octahedra create diffusion pathways for ion transport, thereby allowing the reversible transport and storage of cations. The crystal structure of PBAs can transform among cubic, monoclinic, rhombohedral, trigonal, and tetragonal phases (Fig. 10) depending on the A<sup>+</sup> content and the amount of crystalline water.<sup>87,88</sup> Such structural evolutions significantly influence their electrochemical stability. Moreover, PBAs commonly contain  $[\text{Fe}(\text{CN})_6]$  vacancies, which are often occupied by coordinated water molecules (Fig. 10f). These vacancies not only reduce the number of active sites but may also disrupt the continuity of the Fe-CN-M framework, leading to structural distortion or collapse and, consequently, inferior cycling performance. Owing to PBA open three-dimensional frameworks, facile synthesis, abundant resources, and tunable operating voltage, PBAs have attracted widespread attention as promising electrode materials for energy storage applications.

**3.3.1 PBAs with a single redox-active center.** In 2015, Li *et al.* synthesized  $\text{K}_{0.02}\text{Cu}[\text{Fe}(\text{CN})_6]_{0.7} \cdot 3.7\text{H}_2\text{O}$  (abbreviated as CuFe-PBA) *via* a co-precipitation method and, for the first time, demonstrated reversible  $\text{Al}^{3+}$  storage in PBAs.<sup>89</sup> In a three-electrode configuration with 1 M  $\text{Al}(\text{NO}_3)_3$  electrolyte, the  $\text{Al}^{3+}$  intercalated  $\text{Al}_x\text{CuFe-PBA}$ , similar to the  $\text{Al}_x\text{MnO}_2$  phase observed in Mn-based systems, was employed as the working electrode with activated carbon as the counter electrode, delivering a reversible capacity of  $\sim 50$  mAh g<sup>-1</sup> at 1C and retaining  $\sim 90\%$  of its initial capacity after 1000 cycles at 5C (Fig. 11a). Comparative analysis with other cation systems revealed that

the achievable capacity was mainly limited by the number of electron transfers in the  $\text{Fe}^{2+}/\text{Fe}^{3+}$  redox couple, rather than the nature of the inserted cations. This study provided the first clear evidence for the feasibility of reversible  $\text{Al}^{3+}$  intercalation in PBAs, laying the foundation for subsequent research. Subsequently, Liu *et al.* employed copper hexacyanoferrate ( $\text{KCu}[\text{Fe}(\text{CN})_6] \cdot 8\text{H}_2\text{O}$ , CuHCF) nanoparticles as cathodes in AAIBs and elucidated a two-step kinetic mechanism for  $\text{Al}^{3+}$  intercalation.<sup>90</sup> Cyclic voltammetry revealed two distinct redox peaks, suggesting that  $\text{Al}^{3+}$  undergoes partial desolvation prior to insertion into the A-site of the framework, a phenomenon attributed to the strong solvation effect of the highly charged  $\text{Al}^{3+}$  and the necessary desolvation process (Fig. 11b). During cycling,  $\text{Fe}^{3+}$  coordinated to the C atom was reduced to  $\text{Fe}^{2+}$ , while  $\text{Cu}^{2+}$  coordinated to the N atom remained electrochemically inert, serving only to maintain the structural stability. In a three-electrode configuration with 0.5 M  $\text{Al}_2(\text{SO}_4)_3$  electrolyte, CuHCF delivered a discharge capacity of 62.9 mAh g<sup>-1</sup> at 50 mA g<sup>-1</sup> and still retained 46.9 mAh g<sup>-1</sup> at 400 mA g<sup>-1</sup>, demonstrating excellent rate performance (Fig. 11c). After 1000 cycles at 400 mA g<sup>-1</sup>, a capacity retention of 54.9% was achieved, with nearly 100% coulombic efficiency, indicating high utilization and limited side reactions. Nevertheless, the capacity fading was mainly attributed to the dissolution of CuHCF in the acidic  $\text{Al}_2(\text{SO}_4)_3$  electrolyte.

To address the issues of low capacity, short cycle life, and dissolution of CuHCF in aqueous electrolytes, Zhao *et al.* proposed an electrolyte-engineering strategy by introducing  $[\text{Fe}(\text{CN})_6]^{3-}$  into the electrolyte to drive the re-nucleation of dissolved transition metal ions, thereby preventing framework degradation (Fig. 11d).<sup>91</sup> In the optimized electrolyte, no  $\text{Cu}^{2+}$  were detected, confirming the effectiveness of this approach. Remarkably, CuHCF delivered ultra-stable electrochemical performance, achieving 99.8% capacity retention after 40 000 cycles at 1 A g<sup>-1</sup> in 1 M  $(\text{NH}_4)_2\text{SO}_4$  electrolyte with 5 mmol  $\text{K}_3\text{Fe}(\text{CN})_6$  added (Fig. 11e). This approach effectively

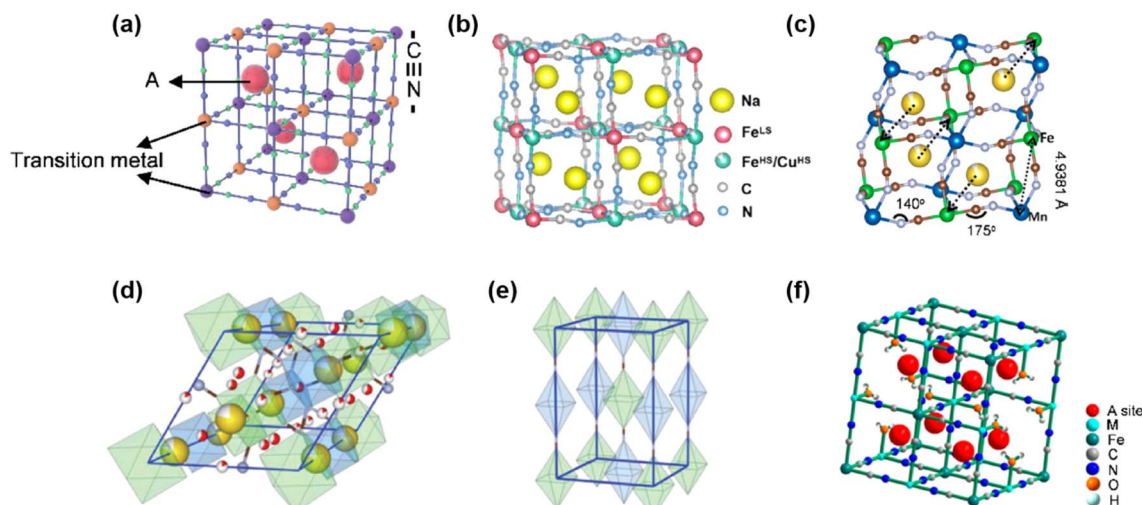


Fig. 10 Schematic crystal structures of PBAs: (a) cubic phase, (b) monoclinic phase, (c) rhombohedral phase, (d) trigonal phase, (e) tetragonal phase, and (f) PBA framework with  $[\text{Fe}(\text{CN})_6]$  vacancies. Reproduced with permission.<sup>86</sup> Copyright 2025, Springer Nature.



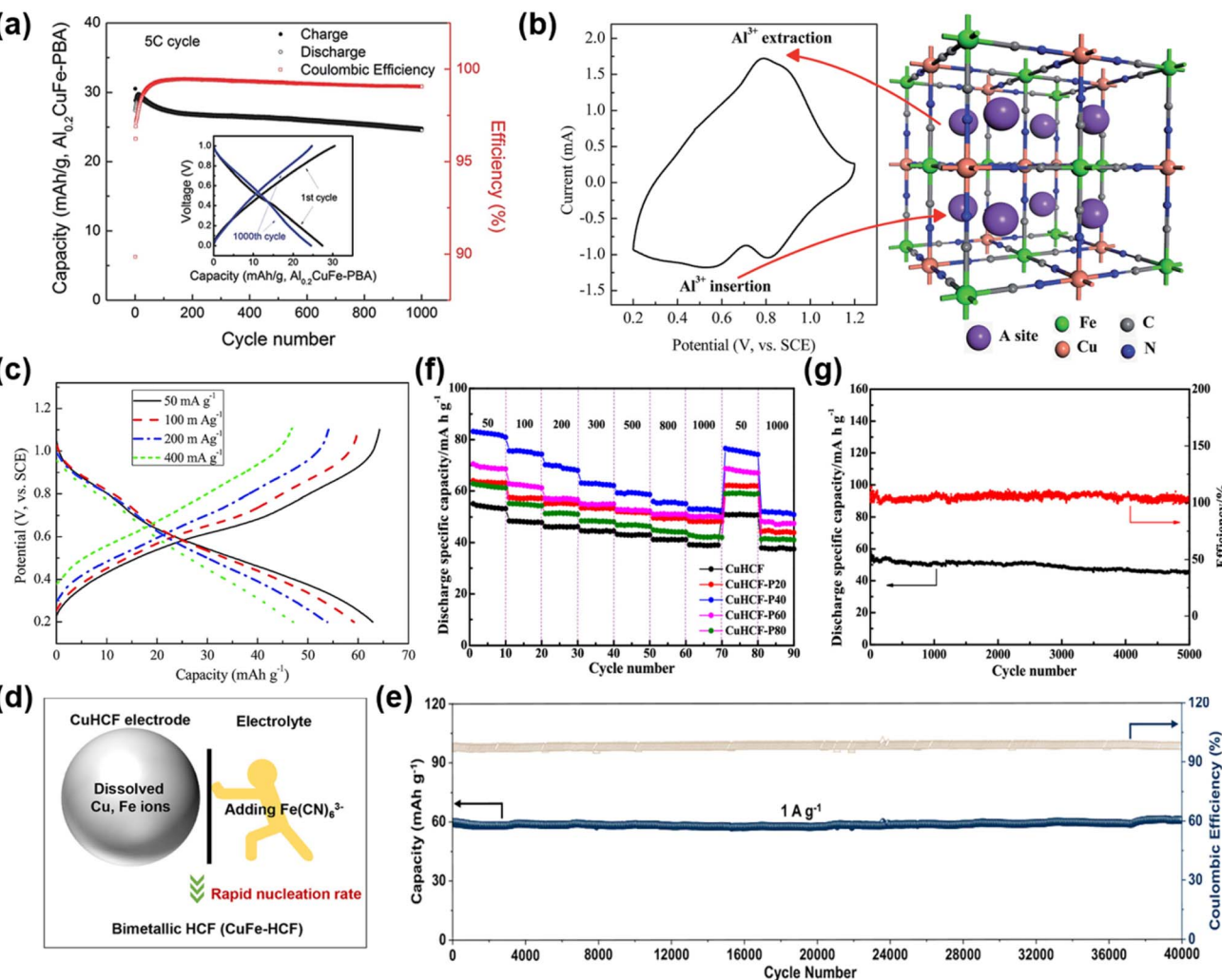


Fig. 11 (a) Cycling performance and coulombic efficiency of an AC/Al<sub>0.2</sub>CuFe-PBA cell at a 5C rate. The inset figure shows the 1st and 1000th charge and discharge curves. Reproduced with permission.<sup>89</sup> Copyright 2015, Wiley-VCH. (b) Typical CV curve of the CuHCF electrode in aqueous Al<sub>2</sub>(SO<sub>4</sub>)<sub>3</sub> and the schematic positions of Al<sup>3+</sup> in the CuHCF framework and (c) charge/discharge curves at different current densities of the CuHCF electrode in 0.5 M Al<sub>2</sub>(SO<sub>4</sub>)<sub>3</sub> aqueous solution. Reproduced with permission.<sup>90</sup> Copyright 2015, Royal Society of Chemistry. (d) Schematic diagram of inhibiting metal ion dissolution and (e) long-term stability performance. Reproduced with permission.<sup>91</sup> Copyright 2023, American Chemical Society. (f) The rate performance of the as-prepared samples at a current density of 50–1000 mA g<sup>-1</sup> and (g) cycle performance at a current density of 1000 mA g<sup>-1</sup>. Reproduced with permission.<sup>93</sup> Copyright 2023, American Chemical Society.

suppressed transition-metal dissolution and enabled ultralong cycling stability of CuHCF. Radhakantha *et al.* demonstrated that higher electrolyte concentrations can enhance the structural stability of the CuHCF framework, exhibiting near-zero lattice strain during Al<sup>3+</sup> insertion.<sup>92</sup>

In addition, Zheng *et al.* investigated the pre-intercalation of Al<sup>3+</sup> into CuHCF at different temperatures and found that the sample treated at 40 °C (CuHCF-P40) exhibited the highest capacity and the best cycling performance.<sup>93</sup> CuHCF-P40 delivered a discharge capacity of 83.1 mAh g<sup>-1</sup> at 50 mA g<sup>-1</sup>, ~1.6 times higher than that of pristine CuHCF (Fig. 11f). Even after 5000 cycles at 1000 mA g<sup>-1</sup>, a capacity of 54.5 mAh g<sup>-1</sup> was retained, corresponding to 80.3% capacity retention (Fig. 11g). This result suggested that moderate Al<sup>3+</sup> pre-intercalation expands ion transport channels and mitigates structural distortion during cycling, enhancing both capacity and stability,

whereas excessive or insufficient Al<sup>3+</sup> respectively blocks diffusion pathways or fails to stabilize the framework effectively. Building upon this, Sayeed *et al.* fabricated flexible full cells pairing Al<sup>3+</sup> pre-intercalated CuHCF cathodes with MoO<sub>3</sub> anodes in a PVA-based 3 M AlCl<sub>3</sub> gel electrolyte.<sup>94</sup> The device delivered 48 mAh g<sup>-1</sup> at a high current density of 3 A g<sup>-1</sup>, with negligible capacity fading over 150 cycles. This work not only further validated the effectiveness of Al<sup>3+</sup> pre-intercalation but also demonstrated its potential for stable and efficient energy storage in flexible and wearable electronic devices.

**3.3.2 PBAs with dual redox-active centers.** The aforementioned CuHCF-based PBA cathodes rely solely on the [Fe(CN)<sub>6</sub>]<sup>4-</sup>/[Fe(CN)<sub>6</sub>]<sup>3-</sup> redox couple, and their reversible capacity is therefore inherently limited. To overcome this constraint, in 2019, Zhou *et al.* synthesized K<sub>0.2</sub>Fe[Fe(CN)<sub>6</sub>]<sub>0.79</sub>·2.1H<sub>2</sub>O (denoted as FF-PBA), featuring dual transition-metal



redox sites, where  $\text{Fe}^{2+}$  coordinated to N atoms and  $\text{Fe}^{3+}$  coordinated to C atoms are both electrochemically active.<sup>95</sup> This dual activity was confirmed by the appearance of two well-defined redox peak pairs in the cyclic voltammetry curves (Fig. 12a). In a three-electrode system with a highly concentrated 5 M  $\text{Al}(\text{CF}_3\text{SO}_3)_3$  water-in-salt electrolyte (Al-WISE), FF-PBA delivered an initial discharge capacity of 116 mAh g<sup>-1</sup> and exhibited an average capacity fading rate of only  $\sim 0.39\%$  per cycle (Fig. 12b). Notably, electrolyte color changes provided visual evidence of dissolution behavior: in 1 M  $\text{Al}(\text{NO}_3)_3$  and 0.5 M  $\text{Al}_2(\text{SO}_4)_3$  solutions, the electrolytes gradually turned light or deep blue, indicating dissolution of FF-PBA. In contrast, the Al-WISE electrolyte showed almost no visible color change even after 50 cycles (Fig. 12c), demonstrating that high-concentration electrolytes effectively suppressed dissolution, thereby ensuring long-term cycling stability. Building upon this, Bai *et al.* assembled a full cell pairing an FF-PBA cathode with a deep

eutectic-modified Al anode in  $\text{Al}(\text{OTf})_3$  electrolyte, which delivered a capacity of 85 mAh g<sup>-1</sup> at 100 mA g<sup>-1</sup> and remained at 58 mAh g<sup>-1</sup> after 150 cycles, with an average coulombic efficiency of 97.1% (Fig. 12d).<sup>96</sup>

Beyond Fe–Fe PBAs, other bimetallic redox-site PBAs (*e.g.*, V–Fe, Mn–Fe, and Co–Fe) have been investigated to enhance the capacity and cycling stability. Gao *et al.* reported potassium nickel hexacyanoferrate (KNHCF) as a cathode paired with an Al foil anode in 5 M  $\text{Al}(\text{CF}_3\text{SO}_3)_3$  electrolyte, revealing for the first time the charge-compensation mechanism of PBAs in multi-metal redox systems.<sup>97</sup> The coin cell achieved an initial discharge capacity of 46.5 mAh g<sup>-1</sup> at 20 mA g<sup>-1</sup>. During cycling, Ni gradually dissolved while Fe redox activity increased, compensating for the capacity loss and sustaining overall performance (Fig. 12e). Furthermore, owing to the multiple valence states of vanadium, vanadium-based PBAs (V-PBAs) can undergo multi-electron redox processes, thereby providing

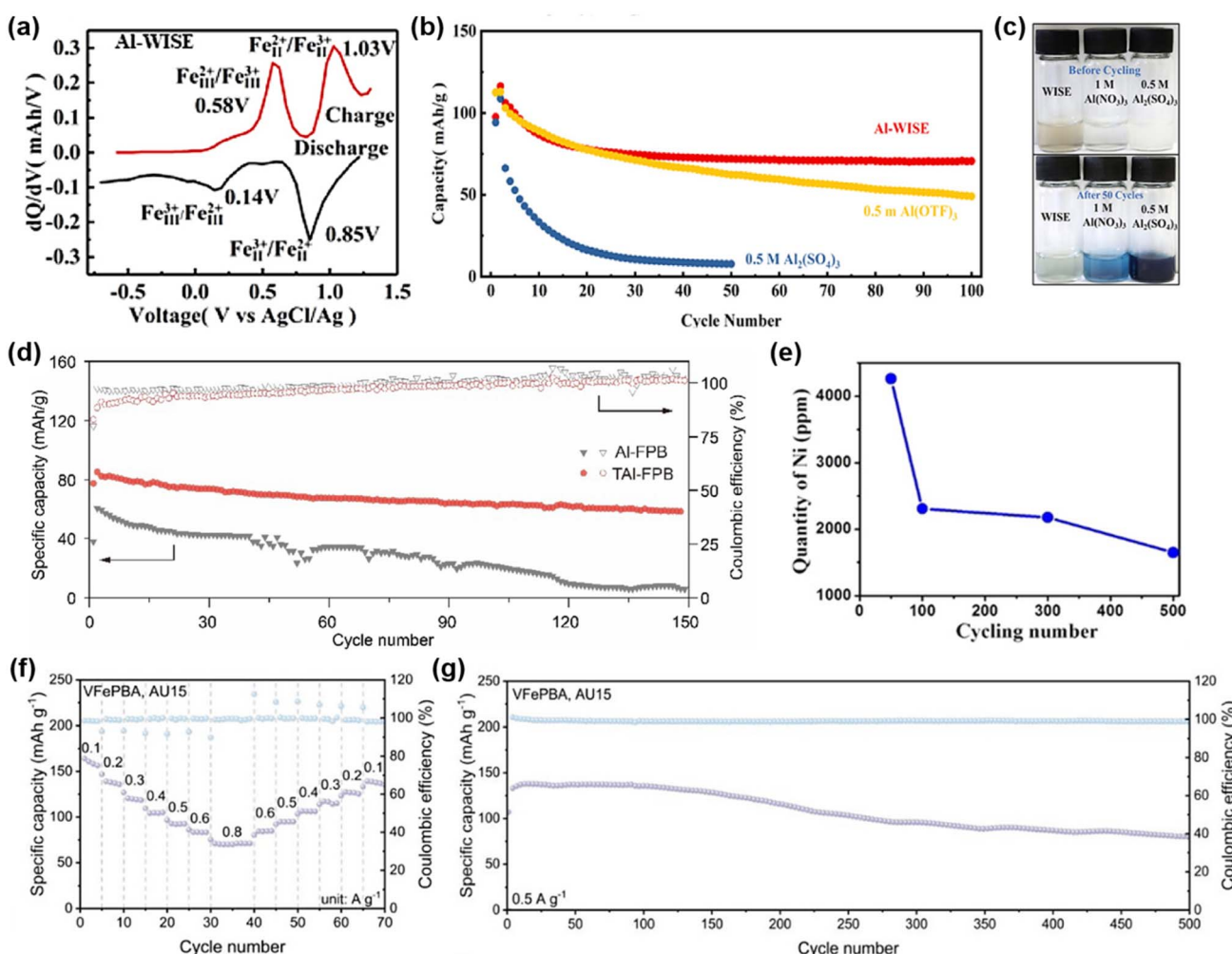


Fig. 12 (a) The differential profiles of the 50th cycle in Al-WISE. (b) Cycling life and coulombic efficiency of the FF-PBA cathode in Al-WISE, 0.5 M  $\text{Al}_2(\text{SO}_4)_3$ , and 0.5 M  $\text{Al}(\text{OTf})_3$  electrolytes. (c) The cathode dissolution experiment. The upper photos are obtained before cycling and the bottom photos are obtained after 50 cycles. Reproduced with permission.<sup>95</sup> Copyright 2019, American Chemical Society. (d) Cycling performance and corresponding coulombic efficiency of aqueous Al-FPB batteries using Al and TAI with 2 M  $\text{Al}(\text{OTf})_3$  at 100 mA g<sup>-1</sup>. Reproduced with permission.<sup>96</sup> Copyright 2021, Elsevier. (e) Ni dissolution concentration from the KNHCF electrode after the 50th, 100th, 300th, 500th cycles measured by ICP-OES. Reproduced with permission.<sup>97</sup> Copyright 2020, Wiley-VCH. (f) Capacitive contribution ratios of VFePBA at various scan rates. (g) Long-term cycling performance of VFePBA. Reproduced with permission.<sup>98</sup> Copyright 2025, Wiley-VCH.



more active sites for charge storage. Feng *et al.* synthesized V-PBAs *via* an acid-assisted hydrothermal method, and the synergistic effect between V and Fe redox centers was found to significantly enhance capacity.<sup>98</sup> In a full cell with a Zn anode and a deep eutectic electrolyte (denoted as AU15, composed of  $\text{Al}_2(\text{SO}_4)_3$ , urea, and  $\text{H}_2\text{O}$ ), V-PBAs delivered a high capacity of  $161.37 \text{ mAh g}^{-1}$  at  $0.1 \text{ A g}^{-1}$  and maintained  $\sim 100 \text{ mAh g}^{-1}$  after 500 cycles at  $0.5 \text{ A g}^{-1}$  (Fig. 12f and g), demonstrating excellent capacity retention and cycling stability.

**3.3.3 Optimization strategies for PBAs.** Although the introduction of electrochemically active metals such as Mn and Co can significantly enhance the specific capacity of PBAs, the accompanying volume effects inevitably lead to lattice distortion and cycling degradation. To address these challenges, researchers have explored strategies such as defect engineering, entropy engineering, and nanostructure engineering to optimize the overall performance of PBAs.

**3.3.3.1 Defect engineering.** Introducing defects or vacancies into the PBA framework can broaden the diffusion channels for

$\text{Al}^{3+}$  transport and improve ionic kinetics, thereby enhancing the electrochemical performance. In 2021, Wang *et al.* designed a defective manganese hexacyanoferrate (MnFe-PBA) cathode containing  $[\text{Fe}(\text{CN})_6]$  vacancies, which effectively expanded the  $\text{Al}^{3+}$  transport pathways and weakened the coulombic interactions between  $\text{Al}^{3+}$  and the host framework (Fig. 13a and b).<sup>99</sup> Benefiting from this structural feature and the presence of dual electrochemically active sites ( $\text{Mn}^{3+}/\text{Mn}^{2+}$  and  $\text{Fe}^{3+}/\text{Fe}^{2+}$ ), the defective MnFe-PBA delivered an initial discharge capacity of  $106.3 \text{ mAh g}^{-1}$  at  $0.2 \text{ A g}^{-1}$  and maintained higher capacity at  $1.0 \text{ A g}^{-1}$ . In contrast, the vacancy-free MnFe-PBA-0 exhibited much lower capacity, highlighting the critical role of vacancies in improving both capacity and rate performance (Fig. 13c).

Similarly, Shang *et al.* utilized the strong chelating effect of  $\text{Na}_2\text{EDTA}$  to introduce a controlled number of Mn cation vacancies ( $V_{\text{Mn}}$ ) into the Mn-PBA framework, obtaining  $V_{\text{Mn}}\text{-PBAs}$ .<sup>100</sup> Compared with conventional Mn-PBAs,  $V_{\text{Mn}}\text{-PBAs}$  delivered an initial discharge capacity of  $108 \text{ mAh g}^{-1}$  at  $0.1 \text{ A g}^{-1}$  and consistently outperformed at higher current

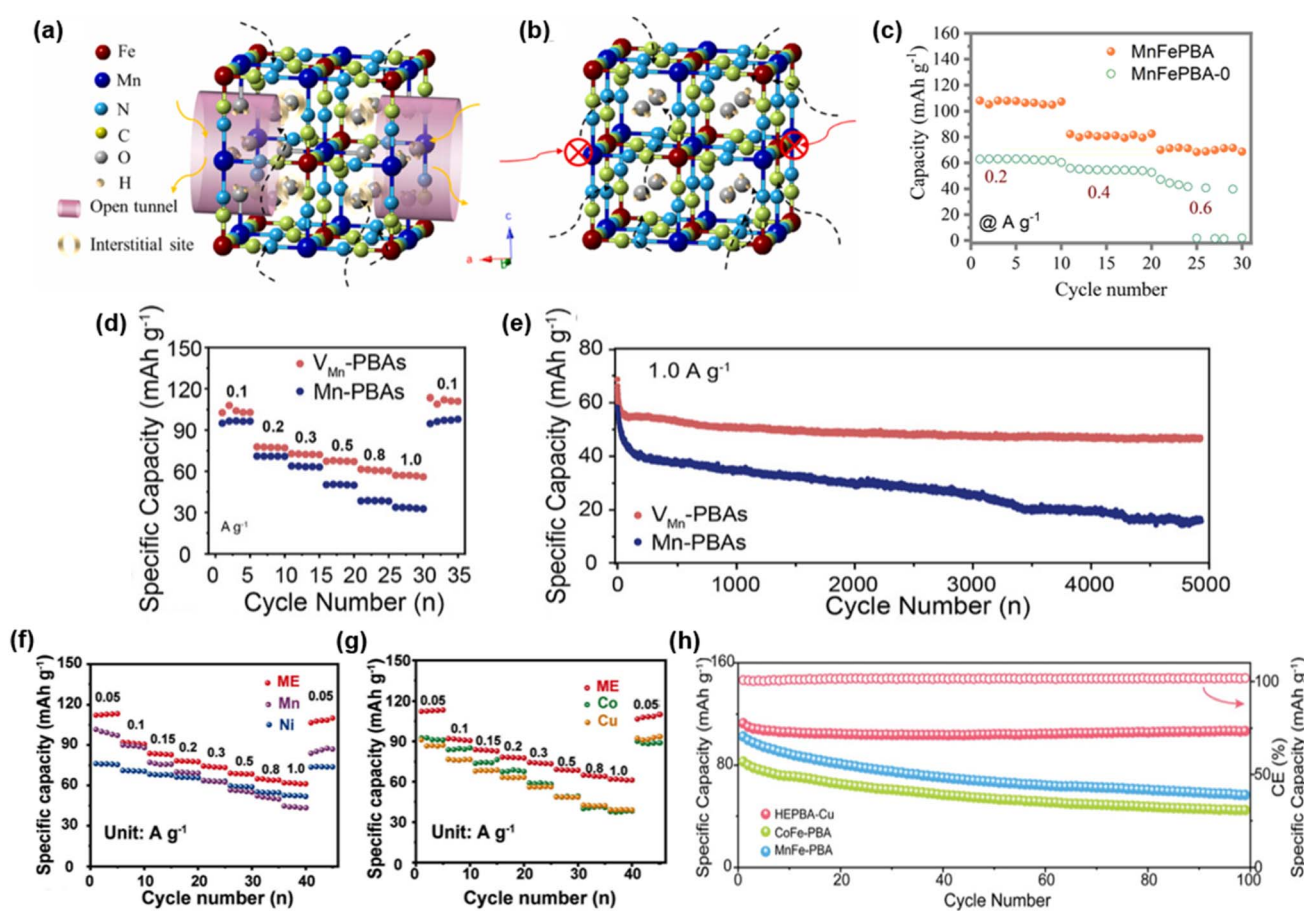


Fig. 13 (a) Corresponding crystal structure of a MnFe-PBA unit cell. The yellow and pink hollow cylinders are used to mark interstitial sites for intercalated ions and enlarged open tunnels for the diffusion of carriers, respectively. (b) Corresponding crystal structure of a non-defective MnFe-PBA unit cell, and the possible pathways for  $\text{Al}$  ion ingress. (c) The effects of vacancy on the rate performance. MnFePBA is with a vacancy and MnFePBA-0 is a non-defective material. Reproduced with permission.<sup>99</sup> Copyright 2021, Elsevier. (d) Rate performance and (e) long-term cycling stability of the PBAs//AC cell at  $1 \text{ A g}^{-1}$ . Reproduced with permission.<sup>100</sup> Copyright 2025, Wiley-VCH. (f and g) Rate performance at current densities from  $0.05$  to  $1.0 \text{ A g}^{-1}$  for ME-PBAs and the different single-metal PBAs. Reproduced with permission.<sup>101</sup> Copyright 2024, Wiley-VCH. (h) Cycling performance of HEPBA-Cu and bimetallic PBA at  $1.0 \text{ A g}^{-1}$ . Reproduced with permission.<sup>102</sup> Copyright 2024, Wiley-VCH.



densities ( $0.1\text{--}1.0\text{ A g}^{-1}$ ). At  $1.0\text{ A g}^{-1}$ ,  $\text{V}_{\text{Mn}}\text{-PBAs}$  retained 67.4% of their capacity after 5000 cycles, in sharp contrast to 26.6% retention for Mn-PBAs (Fig. 13d and e). This improvement was attributed to the introduction of vacancies, which effectively suppressed structural deformation and alleviated the unfavorable Jahn–Teller distortion in Mn–N octahedra. As a result, vacancy engineering enhanced both discharge capacity and cycling stability.

**3.3.3.2 Entropy regulation.** Increasing system entropy ( $\Delta S$ ) can reduce the Gibbs free energy ( $\Delta G$ ), enhancing structural stability and improving redox activity, thereby leading to better electrochemical performance. Liu *et al.* adopted an entropy-production strategy to design structurally reinforced medium-entropy PBA (ME-PBA) frameworks containing multiple redox-active metals, with the composition  $\text{Na}_{1.69}\text{Mn}_{0.34}\text{Co}_{0.33}\text{Ni}_{0.13}\text{Cu}_{0.20}[\text{Fe}(\text{CN})_6]_{0.93}\cdot2.51\text{H}_2\text{O}$ .<sup>101</sup> Compared with single-phase PBAs, ME-PBAs exhibited higher discharge capacities across  $0.05\text{--}1.0\text{ A g}^{-1}$  and ultra-long cycling stability, retaining 66.9% capacity after 10 000 cycles at  $1.0\text{ A g}^{-1}$  (Fig. 13f and g). In a full cell with a MoO anode, ME-PBAs delivered  $60.9\text{ mAh g}^{-1}$  at  $0.5\text{ A g}^{-1}$  and maintained 89.7% of their capacity after 600 cycles. This superior performance was attributed to the synergistic contribution of multiple redox centers: Mn and Fe boost capacity, Co and Cu increase operating voltage, and Ni improves long-term stability, collectively enabling higher capacities and faster kinetics.

Du *et al.* further employed high-entropy PBAs (HE-PBAs) as cathodes for AAIBs.<sup>102</sup> By introducing multiple transition metals, the intrinsic d-band ( $\varepsilon_{\text{d}}$ ) of individual metals was broadened and the electronic degeneracy reduced, thereby improving electron-transfer efficiency and accelerating local charge compensation. Benefiting from the long-range disorder and strong lattice strain fields inherent in high-entropy structures, HE-PBAs accommodated lattice breathing effects while minimizing volume fluctuations during cycling. As a result, HE-PBAs outperformed bimetallic PBAs in both capacity and cycling stability, achieving a remarkable 91.2% capacity retention after 10 000 cycles at a high current density of  $5.0\text{ A g}^{-1}$  (Fig. 13h).

**3.3.3.3 Nanostructure engineering.** PBAs with disordered dispersed morphologies often suffer from long ion-transport pathways and insufficient utilization of electrochemically active sites, which limit their overall electrochemical performance. Nanostructure engineering provides an effective means of regulating ion diffusion and structural stability, thereby improving capacity, rate capability, and cycling stability.

In 2020, Ru *et al.* synthesized potassium cobalt hexacyanoferrate ( $\text{K}_2\text{CoFe}(\text{CN})_6$ ) nanocube assemblies *via* a facile hydrothermal method followed by low-temperature calcination, forming a structure reminiscent of the traditional Chinese Burr puzzle framework (Fig. 14a).<sup>103</sup> In  $1\text{ M Al}(\text{NO}_3)_3$  electrolyte, the material retained 76% of its initial capacity after 1600 cycles at

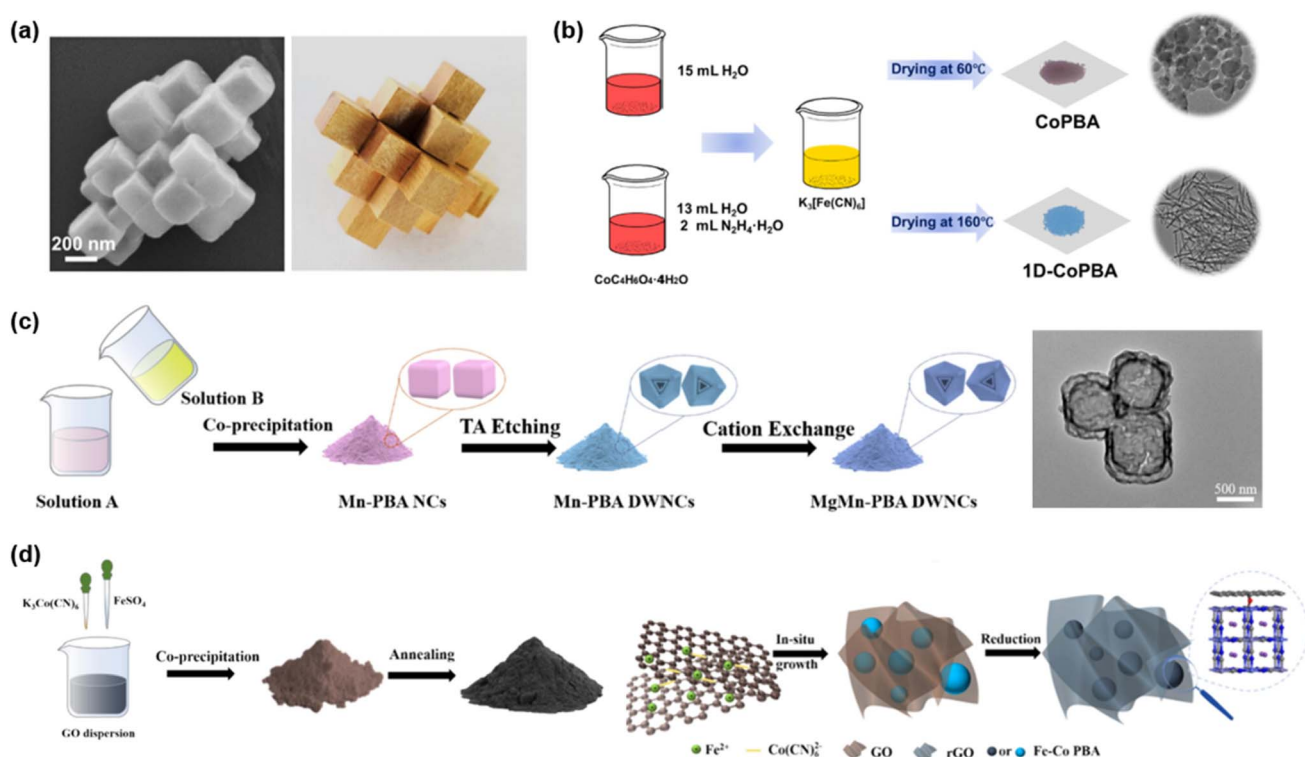


**Fig. 14** (a) SEM images of the  $\text{K}_2\text{CoFe}(\text{CN})_6$  nanocube and structure of burr puzzles. Reproduced with permission.<sup>103</sup> Copyright 2020, Elsevier. (b) Schematic illustration of the synthesis and structural characteristics of the CoPBA and 1D-CoPBA materials. Reproduced with permission.<sup>104</sup> Copyright 2024, American Chemical Society. (c) Schematic representation of the synthetic process of Mn-PBA NCs, Mn-PBA DWNCs and MgMn-PBA DWNCs, respectively. Reproduced with permission.<sup>105</sup> Copyright 2024, Elsevier. (d) Schematic representation of the synthetic process of Fe–Co PBA/rGO. Reproduced with permission.<sup>106</sup> Copyright 2024, Elsevier.

0.1 A g<sup>-1</sup>. Zheng *et al.* prepared one-dimensional Co-PBA (1D-CoPBA) *via in situ* reduction with hydrazine hydrate (Fig. 14b).<sup>104</sup> The 1D architecture significantly improved electrical conductivity and hydrophilicity, thereby enhancing electrolyte accessibility. As a result, 1D-CoPBA delivered 100.1 mAh g<sup>-1</sup> at 50 mA g<sup>-1</sup> and retained 87% of its capacity after 2000 cycles at 1000 mA g<sup>-1</sup>, outperforming conventional Co-PBA. Chang *et al.* employed tannic acid (TA) etching and cation exchange to synthesize Mg-substituted double-walled Mn-PBA nanocubes (MgMn-PBA DWNCs) (Fig. 14c).<sup>105</sup> Mg substitution and Mn vacancies provided abundant active sites, buffered volume changes, and improved ion diffusion. Consequently, MgMn-PBA DWNCs delivered a high capacity of 148 mAh g<sup>-1</sup> with 99.5% retention after 2000 cycles at 1 A g<sup>-1</sup> and maintained 74 mAh g<sup>-1</sup> even at 4 A g<sup>-1</sup>. Furthermore, a full cell assembled with an  $\alpha$ -MoO<sub>3</sub> anode exhibited 78.6 mAh g<sup>-1</sup> after 2000 cycles at 1 A g<sup>-1</sup>, with an average coulombic efficiency of 98.5%, demonstrating outstanding Al<sup>3+</sup> storage capability.

The intrinsic low conductivity of PBAs remains a bottleneck, prompting the development of nanocomposites that combine complementary materials to improve electron transport and overall performance. Zhao *et al.* fabricated Fe-Co PBA/rGO composites *via an in situ* synthesis method (Fig. 14d).<sup>106</sup> Owing to the interfacial chemical coupling between the Fe-Co PBA and rGO, the composite exhibited enhanced electronic structure and accelerated charge transfer. Compared with the pristine Fe-Co PBA, physically mixed Fe-Co PBA/rGO, and rGO, the Fe-Co PBA/rGO composite cathode demonstrated markedly improved rate capability and long-term cycling stability, achieving 112.5 mAh g<sup>-1</sup> at 0.1 A g<sup>-1</sup> and maintaining 66.7 mAh g<sup>-1</sup> after 1500 cycles at 1 A g<sup>-1</sup>.

In summary, PBAs with their three-dimensional open framework and tunable redox potential hold great promise as cathode materials for AAIBs. However, their relatively limited capacity and structural instability arising from lattice distortion during cycling remain key bottlenecks. To address these issues, defect engineering enhances ion diffusion, entropy engineering introduces multiple redox-active centers and reinforces structural robustness, and nanostructure engineering shortens diffusion pathways and buffers volume change. These strategies have collectively improved capacity, rate capability and cycling stability. Looking forward, achieving both high capacity and long lifespan while maintaining framework integrity will be crucial for advancing PBAs in AAIBs. The synergistic optimization of defect regulation, entropy modulation, and nanostructure design, coupled with *in situ* characterization and theoretical modeling, is expected to drive PBAs toward next-generation high-performance cathodes.

### 3.4 Organic cathode materials

In recent years, organic cathode materials have attracted extensive attention due to their abundance, environmental friendliness, structural tunability, and facile synthesis. Compared with inorganic metal oxides, organic materials are composed of common elements (C, H, O, and N) and possess

flexible molecular backbones that can be rationally tailored to optimize electrochemical performance.<sup>107,108</sup> Furthermore, their intrinsic structural flexibility helps mitigate volume strain during charge/discharge processes, thereby enhancing cycling stability. In addition, the relatively weak coordination or ion-dipole interactions within organic frameworks facilitate the rapid migration of Al<sup>3+</sup>, avoiding strong electrostatic interactions typically observed in inorganic cathode materials with high Al<sup>3+</sup> charge density.<sup>109-111</sup>

In terms of energy storage mechanisms, the electrochemical behavior of organic cathodes mainly relies on reversible redox-active groups. Through electron transfer involving carbonyl groups, nitrogen heterocycles, conjugated  $\pi$  frameworks, or radical sites, organic cathodes enable reversible storage and release of Al<sup>3+</sup>. Based on the type of redox-active center, organic cathode materials can be classified into quinone-based compounds, N-heteroaromatic compounds, conductive polymers, and radical polymers.

**3.4.1 Quinone-based compounds.** Quinone-based compounds represent one of the most extensively studied classes of organic cathodes owing to their high redox activity and excellent stability in aqueous environments. Their electrochemical activity originates from reversible carbonyl (C=O) redox centers within the molecular backbone, where each C=O group participates in one-electron transfer, enabling high theoretical capacities. In AAIBs, these carbonyl groups can coordinate with Al<sup>3+</sup> to store and release charge.

In 2021, He *et al.* reported tetrachloro-1,4-benzoquinone (TCQ) as a cathode material for AAIBs.<sup>112</sup> TCQ contains two carbonyl groups that serve as redox-active sites for Al<sup>3+</sup> storage, undergoing a reversible transformation between carbonyl and hydroxyl groups. During discharge, TCQ is reduced to tetrachlorohydroquinone (TCHQ) by accepting two electrons, and the coordinated Al<sup>3+</sup> substitutes the hydrogen atoms of the hydroxyl groups, while in the charging process Al<sup>3+</sup> is released and TCHQ is oxidized back to TCQ (Fig. 15a). The Al//TCQ full cell with 1 M Al(OTf)<sub>3</sub> electrolyte delivered a specific capacity of 147.7 mAh g<sup>-1</sup> at 0.2 A g<sup>-1</sup> and retained 70.7% capacity after 200 cycles at 2 A g<sup>-1</sup> (Fig. 15b and c), demonstrating good cycling stability. This study provided a solid proof-of-concept for quinone derivatives as stable organic cathodes in AAIBs.

Li *et al.* further systematically evaluated six representative quinone compounds, namely 1,4-naphthoquinone (1,4-NQ), 1,2-naphthoquinone (1,2-NQ), anthraquinone (9,10-AQ), phenanthrenequinone (9,10-PQ), pyrene-4,5,9,10-tetraone (PTO), and macrocyclic calix[4]quinone (C4Q), in coin-cell configurations (Fig. 15d).<sup>113</sup> Among them, C4Q exhibited superior performance due to its large cavity and eight adjacent carbonyl groups, each serving as a redox-active site. As a result, C4Q delivered a higher discharge voltage of almost up to 1 V and a specific capacity of 400 mAh g<sup>-1</sup> at 40 mA g<sup>-1</sup> (Fig. 15e and f), along with excellent rate capability (300 mAh g<sup>-1</sup> at 800 mA g<sup>-1</sup>), good cycling stability (81% capacity retention after 50 cycles), and outstanding low-temperature performance (224 mAh g<sup>-1</sup> at  $-20^{\circ}\text{C}$ ). The pouch-type Al-C4Q cell achieved an energy density of 93 Wh kg<sup>-1</sup>, highlighting the potential of quinone-based materials for practical AAIB applications.



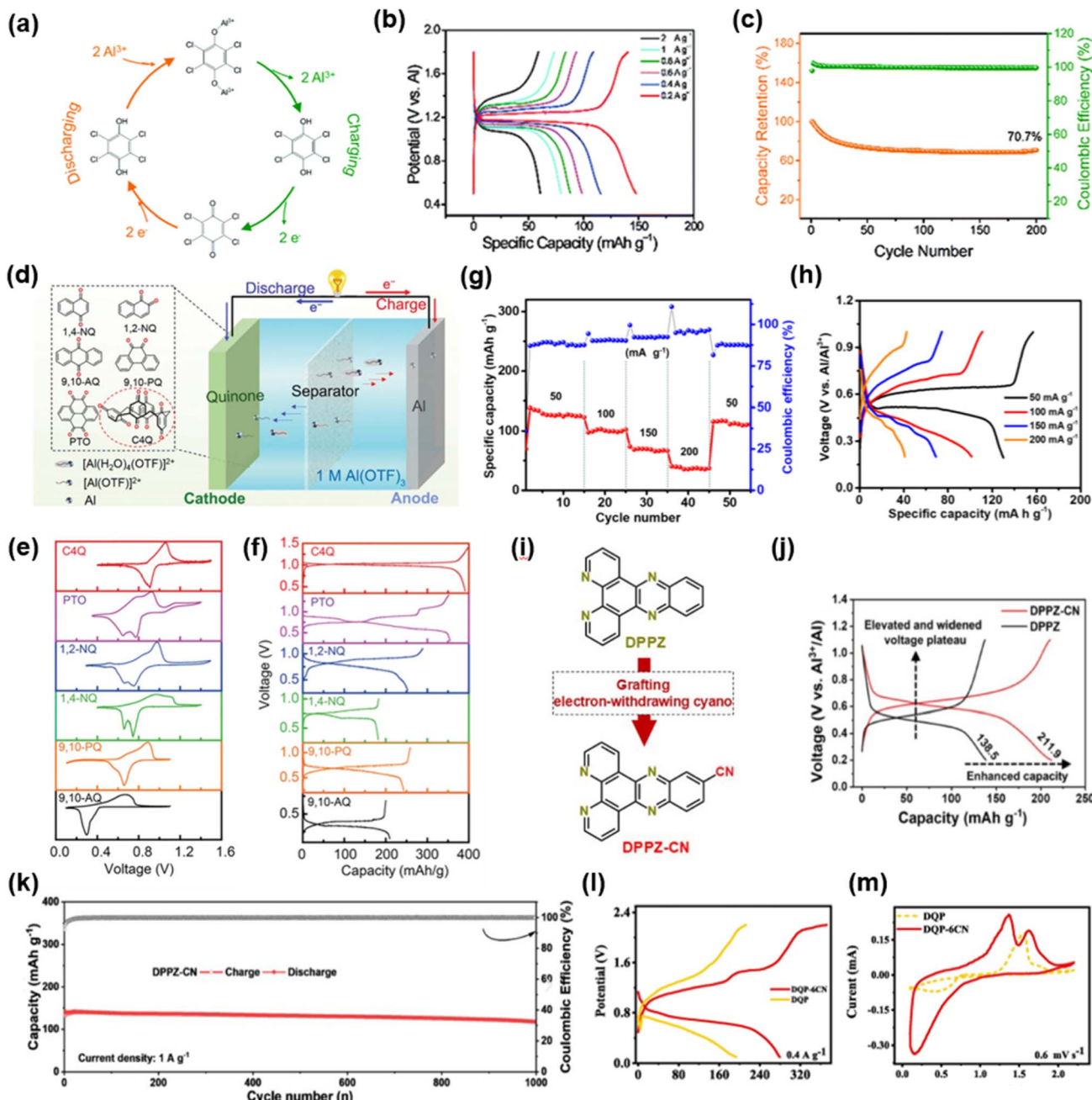


Fig. 15 (a) Schematic diagram of the structure transformation of TCQ in the electrochemical process. (b) GCD curves at various current densities and (c) cycling performance of the Al//TCQ battery. Reproduced with permission.<sup>112</sup> Copyright 2021, Royal Society of Chemistry. (d) Schematic illustration of fabricated aqueous Al-quinone batteries. (e) CV curves at 0.1 mV s<sup>-1</sup> and (f) GCD curves at a current density of 40 mA g<sup>-1</sup> of different quinone compounds. Reproduced with permission.<sup>113</sup> Copyright 2021, Wiley-VCH. (g) Rate performance of PZ at various current densities from 50 to 200 mA g<sup>-1</sup> and (h) corresponding discharge/charge curves. Reproduced with permission.<sup>114</sup> Copyright 2021, Wiley-VCH. (i) Typical molecular structure. (j) Charge/discharge profiles at 0.1 A g<sup>-1</sup> for Al//DPPZ-CN and Al//DPPZ batteries with 1 M Al(ClO<sub>4</sub>)<sub>3</sub> aqueous electrolyte. (k) Long-term cycling performance of the Al//DPPZ-CN battery at 1 A g<sup>-1</sup>. Reproduced with permission.<sup>116</sup> Copyright 2025, Wiley-VCH. (l) GCD curves of DQP-6CN and DQP and (m) CV curves of DQP-6CN. Reproduced with permission.<sup>117</sup> Copyright 2025, Elsevier.

**3.4.2 N-Heteroaromatic compounds.** Compounds containing nitrogen atoms within heteroaromatic frameworks, particularly those with C=N imine groups, represent a versatile class of organic cathodes for AAIBs. The C=N groups act as redox-active centers that reversibly convert to -C-N- during discharge while interacting with Al<sup>3+</sup>. Their extended  $\pi$ -

conjugated frameworks and flexible molecular structures provide abundant active sites, offering high theoretical capacities, analogous to carbonyl-based organic cathodes.

In 2021, Chen *et al.* demonstrated that phenazine (PZ) utilizes its C=N groups as redox-active centers, undergoing reversible -C=N-/C-N- transformations during Al<sup>3+</sup> insertion/

extraction in 5 M Al(OTf)<sub>3</sub> electrolyte.<sup>114</sup> The PZ cathode delivered a high specific capacity of 132 mAh g<sup>-1</sup> at 50 mA g<sup>-1</sup> and retained 76.5% of its capacity after 300 cycles (Fig. 15g and h). The excellent cycling stability was attributed to minimal structural changes, extensive  $\pi$ -conjugation, and intrinsic molecular flexibility of PZ, which maintain structural integrity during cycling.

However, small-molecule N-heteroaromatic electrodes often suffer from limited electronic conductivity and partial solubility in aqueous electrolytes, compromising long-term performance.<sup>115</sup> To address these limitations, Li *et al.* designed di-pyrido[3,2-*a*:2',3'-*c*]phenazine-11-carbonitrile (DPPZ-CN), a multifunctional small-molecule cathode incorporating pyridine, pyrazine, and cyano groups (Fig. 15i).<sup>116</sup> The highly conjugated N-heteroaromatic backbone enhances  $\pi$ - $\pi$  stacking and hydrogen bonding, while the electron-withdrawing cyano group modulates electronic delocalization, improving conductivity and increasing working voltage. DPPZ-CN exhibited 211.9 mAh g<sup>-1</sup> at 100 mA g<sup>-1</sup> with a voltage plateau of 0.62 V and retained 117.7 mAh g<sup>-1</sup> after 1000 cycles at 1 A g<sup>-1</sup>, corresponding to a capacity retention of 82.4% (Fig. 15j and k). Building on this strategy, Lu *et al.* synthesized diquinoxalino[2,3-*a*:2',3'-*c*]phenazine-2,3,8,9,14,15-hexacarbonitrile (DQP-6CN) functionalized with six cyano groups.<sup>117</sup> The introduction of multiple cyano groups not only increased the number of redox-active sites but also strengthened  $\pi$ -conjugation and reduced local electron density, thus enhancing capacity, electronic conductivity and structural stability. In 5 M Al(OTf)<sub>3</sub> electrolyte, DQP-6CN delivered a high reversible capacity of 279 mAh g<sup>-1</sup> at 400 mA g<sup>-1</sup>, surpassing that of unsubstituted DQP (193.5 mAh g<sup>-1</sup>) (Fig. 15l). Cyclic voltammetry (CV) revealed multiple distinct redox peaks for DQP-6CN, confirming the simultaneous participation of imine and cyano groups in the redox processes (Fig. 15m). Despite these advances, N-heteroaromatic cathodes generally operate at discharge voltages below 0.8 V, lower than that for quinone-based materials, which remains a limitation for their broader applications in AAIBs.

#### 3.4.3 $\pi$ -Conjugated carbonyl-imine hybrid compounds.

Beyond organic cathodes containing a single type of redox-active center, such as carbonyl or imine groups, recent efforts have focused on constructing hybrid systems that integrate both functionalities within a conjugated backbone. Introducing C=O and C=N groups into a planar  $\pi$ -conjugated framework enables multiple redox-active sites and enhanced intermolecular interactions. The carbonyl and imine groups both provide reversible electron-transfer centers, increasing theoretical capacity, while the extended  $\pi$ -conjugation improves electronic conductivity, suppresses dissolution, and enhances structural stability. Consequently,  $\pi$ -conjugated carbonyl-imine hybrid compounds have emerged as a promising design strategy for high-performance organic cathodes in AAIBs.

In 2024, Su *et al.* designed a fully conjugated heterocyclic molecule, tribenzoquinoline-5,10-dione (3BQ), derived from 9,10-anthraquinone (AQ), featuring both carbonyl and imine groups for AAIBs (Fig. 16a).<sup>118</sup> The multiple redox centers and expanded  $\pi$ -conjugated framework endowed 3BQ with a high

theoretical capacity of 515 mAh g<sup>-1</sup>. When composited with conductive carbon nanotubes (CNTs) featuring highly delocalized  $\pi$ -bonds, the resulting 3BQ-CNT hybrid exhibited enhanced  $\pi$ - $\pi$  interactions, improved electronic delocalization, and stabilized molecular packing, facilitating efficient Al<sup>3+</sup> transport. Consequently, 3BQ-CNTs delivered 445.84 mAh g<sup>-1</sup> at 0.05 A g<sup>-1</sup> and maintained 125.7 mAh g<sup>-1</sup> after over 4000 cycles at 1.0 A g<sup>-1</sup>, with a per-cycle decay rate of 0.011% (Fig. 16b and c).

Building on this hybrid design concept, Lu *et al.* synthesized DDQP, a  $\pi$ -conjugated planar carbonyl and imine conjugated backbone, *via* dehydration condensation of phenanthrenequinone (PQ) and 2,3,5,6-tetraaminocyclohexa-2,5-diene-1,4-dione (TABQ) (Fig. 16d).<sup>119</sup> Theoretical calculations revealed that DDQP exhibits higher electronic density of states near the Fermi level, a lower lowest unoccupied molecular orbital (LUMO) energy, and a reduced LUMO-HOMO gap than its precursors, indicating stronger electron affinity and improved charge transport ability (Fig. 16e). Electrochemical measurements revealed that DDQP delivered 239.54 mAh g<sup>-1</sup> at 400 mA g<sup>-1</sup>, nearly twice that of PQ and TABQ (Fig. 16f), along with improved rate capability and cycling stability. Similarly, Hu *et al.* synthesized BQPT (benzo[*f*]benzo[6,7]quinoxalino[2,3,9,10]phenanthrol[4,5-*abc*]phenazine-5,10,16,21-tetraone), a multi-redox hybrid containing four carbonyl and four imine groups, *via* a dehydration condensation strategy.<sup>120</sup> Both C=O and C=N groups participate in redox processes during discharge, collectively accepting eight electrons and coordinating with eight Al(OTf)<sub>2</sub><sup>+</sup> cations (Fig. 16g). This multi-electron mechanism enabled a high capacity of 321.71 mAh g<sup>-1</sup> at 0.4 A g<sup>-1</sup> (Fig. 16h). Therefore, rational functional group integration and conjugated backbone design offer a feasible and effective route to enhance the electrochemical performance of organic cathodes.

Overall, these studies demonstrate that incorporating both carbonyl and imine groups within an extended  $\pi$ -conjugated framework is an effective strategy to enhance the electrochemical performance of AAIB cathodes. Such hybrid molecular design overcomes the limitations of single-type redox centers, providing a promising pathway for the development of high-performance organic cathodes for AAIBs. Nevertheless, both small and macro-molecular organic cathodes are prone to dissolution, which can be mitigated by incorporating them into conductive polymers, as discussed in the following section.

#### 3.4.4 Conductive polymers.

Conductive polymers, including polyaniline (PANI), polypyrrole (PPy), and polythiophene (PTh), have attracted increasing attention in aqueous batteries owing to their unique  $\pi$ -conjugated backbones and favorable electrochemical reversibility.<sup>121,122</sup> Compared with small-molecule organic cathodes, conductive polymers possess higher molecular weights and stronger intermolecular interactions, which help mitigate dissolution. Their continuous conjugated skeleton facilitates electronic transport along the polymer chains and supports rapid and reversible electrochemical reactions. Furthermore, the molecular structures of conductive polymers can be flexibly tuned *via* monomer design



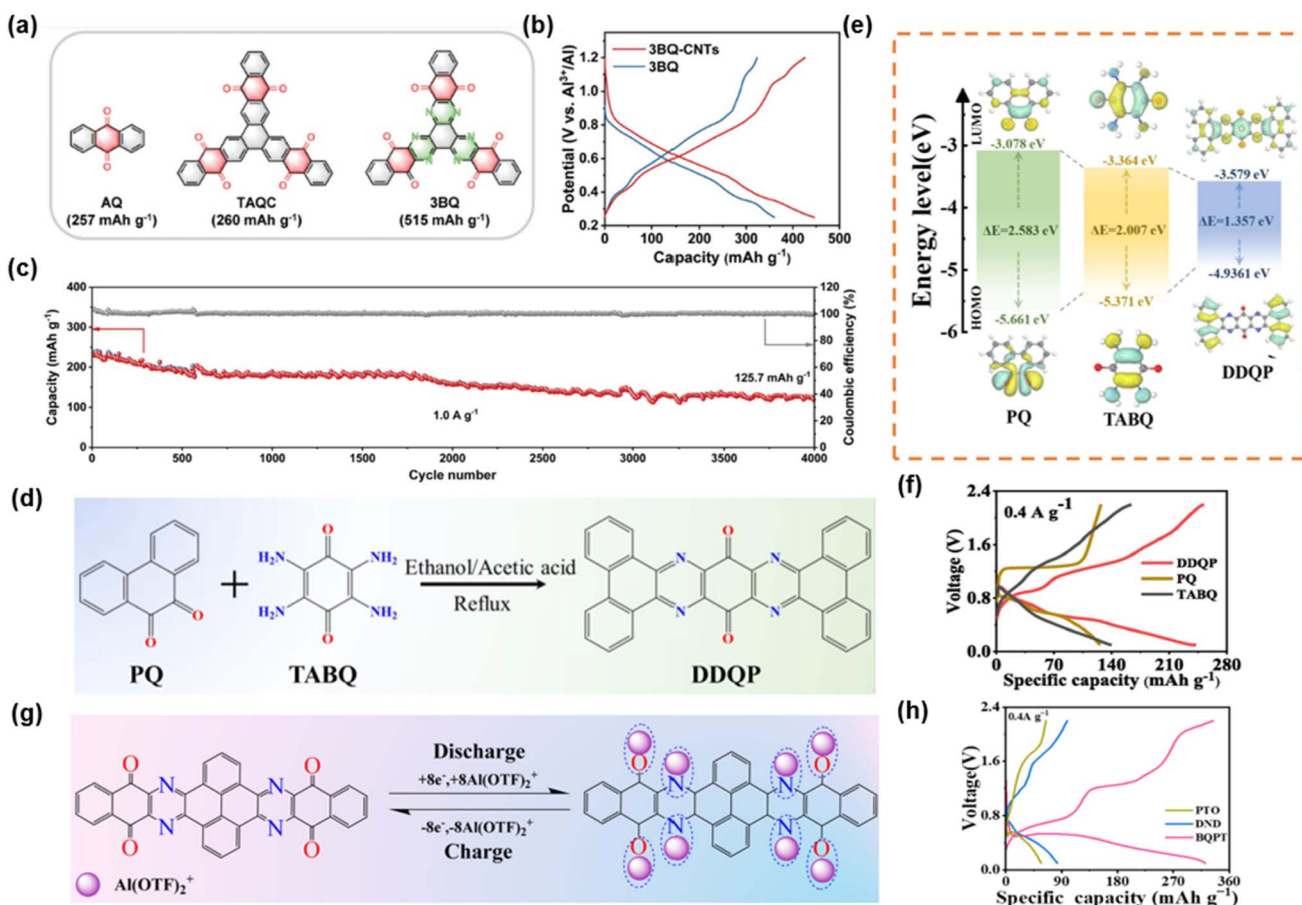


Fig. 16 (a) Schematic illustration of molecular design from AQ to TAQC and 3BQ via expanding the  $\pi$ -conjugation strategy. (b) Typical galvanostatic charge/discharge profiles of the 3BQ-CNTs//Al and 3BQ//Al batteries at  $0.05 \text{ A g}^{-1}$ . (c) Long-cycle performance of 3BQ-CNTs electrodes at  $1.0 \text{ A g}^{-1}$ . Reproduced with permission.<sup>118</sup> Copyright 2024, Wiley-VCH. (d) Synthesis pathway of DDQP. (e) LUMO and HOMO of PQ, TABQ and DDQP and the energy level gap. (f) First charge/discharge curves of PQ, TABQ and DDQP at  $400 \text{ mA g}^{-1}$ . Reproduced with permission.<sup>119</sup> Copyright 2024, Elsevier. (g) Mechanistic description of the reversible redox reaction of BQPT and (h) GCD curves of DND, PTO, and BQPT electrodes at  $0.4 \text{ A g}^{-1}$ . Reproduced with permission.<sup>120</sup> Copyright 2024, American Chemical Society.

and copolymerization, enabling improvements in specific capacity, conductivity, and cycling stability.

Building on this foundation, in 2022, Sariyer *et al.* synthesized poly(*o*-phenylenediamine) (PoPD) *via* electro-polymerization. Using  $0.25 \text{ M AlCl}_3$  as the electrolyte in a three-electrode system, PoPD delivered an average discharge potential of  $-0.20 \text{ V}$  and a capacity of  $156 \text{ mAh g}^{-1}$  at  $5\text{C}$  (Fig. 17a).<sup>123</sup> Even after 1000 cycles,  $110 \text{ mAh g}^{-1}$  was retained (Fig. 17b), demonstrating excellent cycling stability. Building upon this, Meng *et al.* functionalized PANI with sulfonic acid groups to obtain SPANI, which enhanced both conductivity and ion-polymer interactions.<sup>124</sup> In an aqueous deep eutectic electrolyte composed of  $\text{Al}(\text{ClO}_4)_3 \cdot 9\text{H}_2\text{O}$  and succinonitrile (SN), SPANI exhibited a capacity of  $185 \text{ mAh g}^{-1}$  at  $0.1 \text{ A g}^{-1}$ , outperforming pristine PANI ( $143 \text{ mAh g}^{-1}$ ) (Fig. 17c), and retained  $165 \text{ mAh g}^{-1}$  with 89% capacity retention after 300 cycles. XPS analysis revealed the redox mechanism: during charging, the reduced  $-\text{NH}_2$  groups in SPANI were oxidized to  $-\text{NH}^+$  and  $=\text{NH}^+$ , which coordinated with  $\text{ClO}_4^-$ , while during discharging, the oxidized groups were reduced back and coordinated with  $\text{Al}^{3+}$

(Fig. 17d). This study highlighted that incorporating the  $-\text{SO}_3\text{H}$  group simultaneously improved conductivity, ion interaction and electrochemical reversibility, offering valuable guidelines for the molecular design of conductive polymer cathodes.

Extending these advances, Wang *et al.* developed carbon-supported poly(2,3-diaminophenazine) (PDAP) cathodes *via* electropolymerization (Fig. 17e).<sup>125</sup> The PDAP framework, containing  $\text{C}=\text{N}$  and  $-\text{NH}-$  groups, provided abundant redox-active sites. In  $1 \text{ M Al}(\text{ClO}_4)_3$  electrolyte, the Al//PDAP cell delivered a high capacity of  $338 \text{ mAh g}^{-1}$  at  $0.2 \text{ A g}^{-1}$  and maintained  $233 \text{ mAh g}^{-1}$  after 100 cycles. Even at  $2 \text{ A g}^{-1}$ ,  $86 \text{ mAh g}^{-1}$  was retained after 1000 cycles (65% retention). PDAP also exhibited excellent temperature tolerance, delivering  $155 \text{ mAh g}^{-1}$  at  $-20^\circ\text{C}$  and up to  $348 \text{ mAh g}^{-1}$  at  $45^\circ\text{C}$ . These outstanding properties originated from the strong  $\pi-\pi$  stacking and  $\text{N}-\text{H}\cdots\text{N}$  hydrogen bonding among PDAP chains, which suppressed dissolution, as evidenced by UV-vis spectroscopy of electrolyte after soaking (Fig. 17g). Theoretical calculations further confirmed that increasing the chain length from monomer to tetramer narrowed the bandgap (from  $1.525$  to  $1.058 \text{ eV}$ ) and



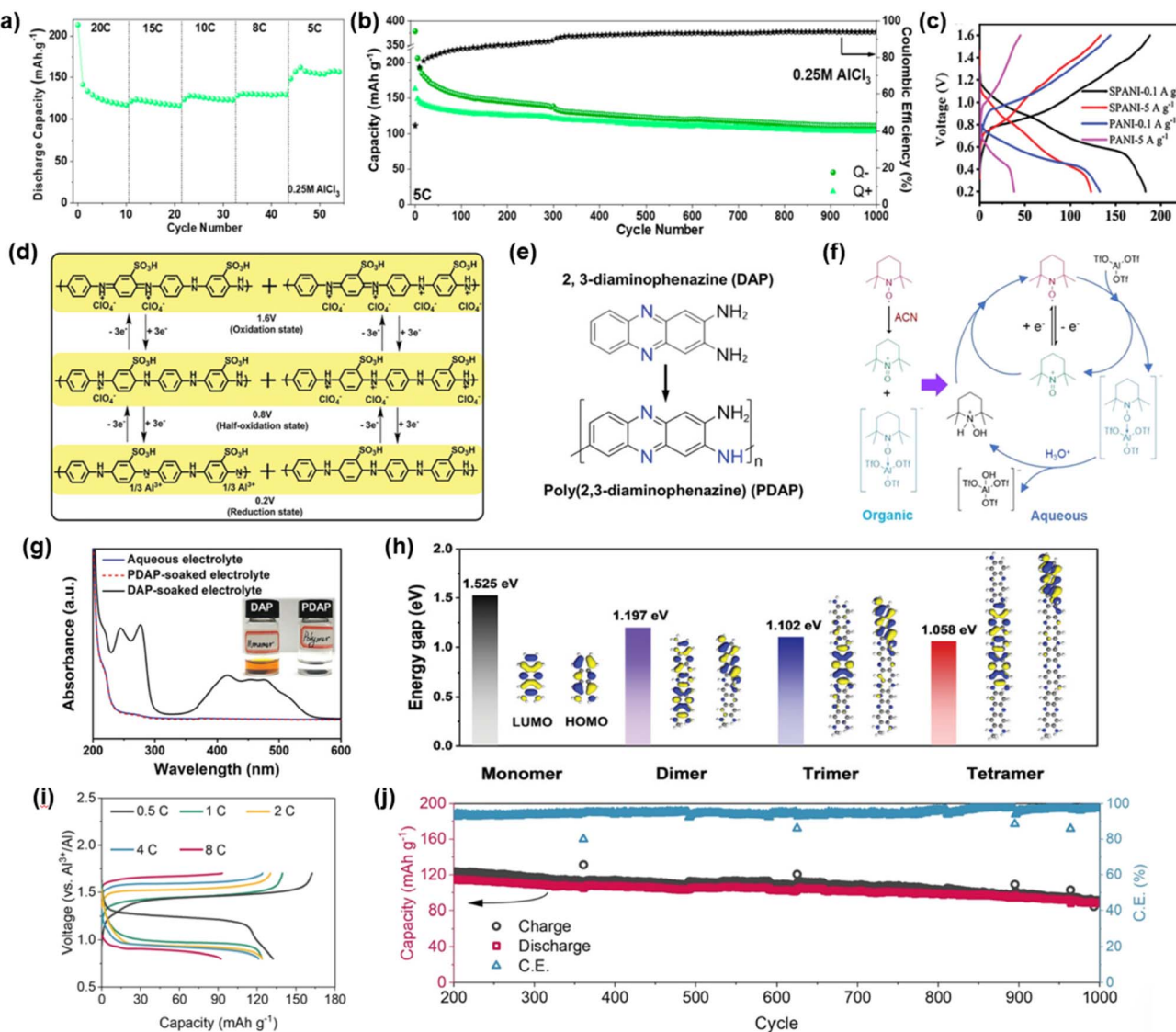


Fig. 17 (a) C-Rate performance in 0.25 M  $\text{AlCl}_3$ . (b) Long-term cycling performance at 5C in 0.25 M  $\text{AlCl}_3$ . Reproduced with permission.<sup>123</sup> Copyright 2022, American Chemical Society. (c) The discharge/charge curves at different current densities and (d) schematic diagram of the charge/discharge mechanism of the SPANI/ASHEE/Al battery. Reproduced with permission.<sup>124</sup> Copyright 2022, Wiley-VCH. (e) Illustration of the electropolymerization process of PDAP. (g) The UV-vis spectra of DAP-soaked, PDAP-soaked electrolyte, and fresh electrolyte (1 M  $\text{Al}(\text{ClO}_4)_3$ ). (h) HOMO–LUMO energy gaps for the optimized models with different molecular chain lengths (monomer, dimer, trimer, and tetramer). Reproduced with permission.<sup>125</sup> Copyright 2024, Wiley-VCH. (f) Schematic illustration of the solvent-dependent redox behavior of TEMPO in acetonitrile and aqueous electrolytes. (i) Typical charge/discharge voltage profiles of the PTMA cathodes cycled at 0.5 to 8C. (j) Long cycling performance and coulombic efficiency of PTMA-based AAIBs at 4C. Reproduced with permission.<sup>129</sup> Copyright 2023, American Chemical Society.

increased the density of states near the Fermi level, indicating enhanced electron delocalization and faster charge transfer (Fig. 17h). This work not only provided a promising strategy for designing high-performance organic cathodes for AAIBs, but also demonstrated their stable operation over a wide temperature range.

Overall, these studies illustrate the versatility of conductive polymers as AAIB cathodes. Progressing from PoPD to functionalized PANI and PDAP, rational molecular design through functional group incorporation and extension of the conjugated backbone has proven effective in improving capacity,

conductivity, and cycling stability. These findings highlight conductive polymers as a tunable platform for designing robust, high-performance organic cathodes for AAIBs.

**3.4.5 Radical polymers.** Radical polymers represent a class of organic cathode materials, typically composed of aliphatic polymer backbones with redox-active side groups. Unlike conventional conductive polymers, their electrochemical activity primarily arises from reversible redox reactions between the free radicals or oxoammonium ions on the side chains, allowing for stable potential output during charge–discharge processes.<sup>126,127</sup> The most representative system is based on



2,2,6,6-tetramethylpiperidin-1-oxyl (TEMPO) side groups, which exhibit high redox potentials and fast electron-transfer kinetics.<sup>128</sup> However, TEMPO is prone to disproportionation under acidic conditions, limiting their applicability in acidic AAIBs electrolytes.

In 2023, Jiang *et al.* systematically investigated the electrochemical behavior of TEMPO radicals in both organic and aqueous media.<sup>129</sup> They found that TEMPO undergoes irreversible disproportionation in acetonitrile due to the formation of aminoxy anions ( $\text{TEMPO}^-$ ), which coordinate with excess  $\text{Al}(\text{OTf})_3$ , rendering the redox process irreversible. In contrast, in aqueous electrolytes,  $\text{TEMPO}^-$  in  $[\text{Al}(\text{OTf})_3 \cdot \text{TEMPO}]^-$  can be substituted by  $\text{OH}^-$  or water molecules, enabling a fully

reversible  $\text{TEMPO}^+/\text{TEMPO}^-$  redox cycle and preserving the radical activity (Fig. 17f). Building on this understanding, the authors prepared the first TEMPO radical polymer cathode, poly(TEMPO methacrylate) (PTMA). In 1 M  $\text{Al}(\text{OTf})_3$  electrolyte, the PTMA cathode delivered a discharge capacity of approximately 120 mAh g<sup>-1</sup> at 4C and retained 77% after 800 cycles, corresponding to a low per-cycle decay rate of 0.028% (Fig. 17i and j). This work highlights the critical role of aqueous environments in stabilizing TEMPO radicals and demonstrates the potential of non-conjugated radical polymers as high-performance cathodes for AAIBs. Overall, the electrochemical performance of various cathode materials discussed in this review is summarized in Table 1.

Table 1 Electrochemical performances of reported cathode materials for AAIBs

Cathode material	Anode material	Electrolyte	Discharge voltage (V)	Current density (mA g <sup>-1</sup> )	Specific capacity (mAh g <sup>-1</sup> )	Cycle number	Ref.
$\alpha\text{-MnO}_2$	Al	2 M $\text{Al}(\text{OTf})_3$	1.3	100	380	40	45
$\alpha\text{-MnO}_2$	Al	5 M $\text{Al}(\text{OTf})_3$	1.5	100	480	180	46
$\gamma\text{-MnO}_2$	Al	5 M $\text{Al}(\text{OTf})_3$	1.5	200	482	200	47
$\delta\text{-MnO}_2$	Al	2 M $\text{Al}(\text{OTf})_3$ + 0.5 M $\text{MnSO}_4$	1.35	100	554	65	48
$\delta\text{-MnO}_2$	Pt-sputtered Al	5 M $\text{Al}(\text{OTf})_3$	1.1	50	452	50	49
$\text{Al}_x\text{MnO}_2 \cdot n\text{H}_2\text{O}$	Al-Cu	2 M $\text{Al}(\text{OTf})_3$	1.5	500	400	400	51
$\text{Al}_x\text{MnO}_2 \cdot n\text{H}_2\text{O}$	Al	5 M $\text{Al}(\text{OTf})_3$	1.2	30	467	60	52
$\text{Al}_x\text{MnO}_2$	Zn-Al	2 M $\text{Al}(\text{OTf})_3$	1.6	100	460	80	53
BQ- $\text{Al}_x\text{MnO}_2$	Zn <sub>50</sub> Al <sub>50</sub> alloy	2 M $\text{Al}(\text{OTf})_3$ + 0.2 M $\text{Mn}(\text{OTf})_2$	1.6	1000	300	800	55
Cu <sup>2+</sup> -pre-intercalated $\delta\text{-MnO}_2$	Al	5 M $\text{Al}(\text{OTf})_3$	1.5	400	363	300	56
Co-doped $\delta\text{-MnO}_2$	Al	2 M $\text{Al}(\text{OTf})_3$	1.4	100	585	300	59
V-doped $\delta\text{-MnO}_2$	Al-Cu	2 M $\text{Al}(\text{OTf})_3$	1.14	200	518	400	60
$\text{V}_2\text{O}_5$	Al	2 M $\text{Al}(\text{OTf})_3$	0.9	20	200	50	38
$\text{V}_2\text{O}_5$	Al	5 M $\text{Al}(\text{OTf})_3$	—	400	400	200	65
$\text{V}_2\text{O}_5@\text{MXene}$	Al	5 M $\text{Al}(\text{OTf})_3$	—	100	626	100	66
$\text{VO}_2$	Al	5 M $\text{Al}(\text{OTf})_3$	—	150	234	1000	69
Cu-doped $\text{VO}_2$	Al	5 M $\text{Al}(\text{OTf})_3$	—	400	642	200	71
$\text{LiV}_3\text{O}_8$	Activated carbon	2 M $\text{Al}(\text{OTf})_3$	—	0.29C	289	500	72
$\text{VOPO}_4 \cdot 2\text{H}_2\text{O}$	Al	2.5 M $\text{Al}(\text{OTf})_3$	0.9	20	125	40	80
CuHCF	Graphite	0.5 M $\text{Al}_2(\text{SO}_4)_3$	—	50	63	1000	90
CuHCF	—	1 M $\text{AlCl}_3$	—	1000	54.5	5000	93
CuHCF	$\text{MoO}_3$	3 M $\text{AlCl}_3$	0.6	3000	48	150	94
FeFe-PBA	Deep eutectic-modified Al	2 M $\text{Al}(\text{OTf})_3$	—	100	85	150	96
KNHCF	Al	5 M $\text{Al}(\text{OTf})_3$	0.7	20	46.5	500	97
V-PBA	Zn	Deep eutectic	1.2	100	161	500	98
MnFe-PBA	Al	1 M $\text{Al}(\text{OTf})_3$	0.9	200	106	50	99
Medium-entropy PBA	MoO	3 M $\text{Al}(\text{OTf})_3$	—	500	60.9	600	101
MgMn-PBA	$\text{MoO}_3$	1 M $\text{Al}(\text{NO}_3)_3$	—	1000	148	2000	105
Fe-Co PBA/rGO	$\text{MoO}_3$	1 M $\text{AlCl}_3$	—	100	112.5	1500	106
TCQ	Zn-Al	1 M $\text{Al}(\text{OTf})_3$	—	200	148	200	112
C4Q	Al	1 M $\text{Al}(\text{OTf})_3$	1.0	40	400	50	113
PZ	Al	5 M $\text{Al}(\text{OTf})_3$	0.6	50	132	300	114
DPPZ-CN	Al	1 M $\text{Al}(\text{ClO}_4)_3$	0.6	100	212	1000	116
DQP-6CN	Al	5 M $\text{Al}(\text{OTf})_3$	0.8	400	279	200	117
3BQ-CNT	Al	1 M $\text{Al}(\text{OTf})_3$	—	50	446	4000	118
SPANI	Al	$\text{Al}(\text{ClO}_4)_3 \cdot 9\text{H}_2\text{O}$ + succinonitrile	0.5	100	185	300	124
PDAP	Al	1 M $\text{Al}(\text{ClO}_4)_3$	—	200	338	100	125
poly(TEMPO methacrylate)	Al	1 M $\text{Al}(\text{OTf})_3$	1.1	4C	120	800	129



## 4. Summary and prospects

AAIBs as an emerging electrical energy storage technology, combine high safety, environmental friendliness and low cost, demonstrating promising potential for green energy applications. Despite notable progress in electrode material design and electrolyte optimization in recent years, the development of AAIBs remains at an early stage, and their commercial deployment is still a considerable distance away. Key limiting factors include the sluggish migration kinetics of multivalent  $\text{Al}^{3+}$  and insufficient structural reversibility of cathode materials during repeated charge/discharge cycles, which lead to capacity fading and restricted cycle life. These issues significantly constrain AAIBs from achieving high capacity, high power density, and long-term stability.

Regarding cathode materials, different types exhibit distinct structural features and ion/electron transport properties, which determine their electrochemical performance and associated challenges. This review systematically summarizes recent advances in AAIBs cathode materials, focusing on four representative systems: manganese-based oxides, vanadium-based compounds, PBAs, and organic materials. Specifically:

(1) Manganese oxides are among the most widely studied AAIB cathodes due to their abundance, low cost, diverse crystal structures and multiple electron-transfer capability. Layered  $\delta\text{-MnO}_2$ , with large interlayer spacing and two-dimensional diffusion channels, facilitates  $\text{Al}^{3+}$  diffusion and generally exhibits high specific capacity, whereas tunnel-type  $\text{MnO}_2$  ( $\alpha$ ,  $\beta$ , and  $\gamma$ ) with narrower channels limits  $\text{Al}^{3+}$  diffusion and storage, resulting in lower capacity and sluggish kinetics. Although layered structures offer higher capacity, they often suffer from structural instability during cycling, undergoing *in situ* phase transformations to thermodynamically more stable  $\text{Al}_x\text{MnO}_2$  phases. While this process can partially relieve lattice strain, it often causes capacity decay. Unmodified  $\text{MnO}_2$  cathodes can deliver initial capacities of 500–600  $\text{mAh g}^{-1}$ , but structural collapse and Mn dissolution hinder stable cycling beyond 200 cycles. Strategies such as molecular or metal-ion pre-intercalation or doping have been developed to expand interlayer spacing, mitigate lattice strain, enhance structural flexibility, and prolong cycling stability. However, while pre-intercalation or doping strategies can effectively enlarge the interlayer spacing, they may slightly perturb the crystal structure, which could influence long-term structural stability during repeated cycling. In addition, the strong interaction between  $\text{Al}^{3+}$  ions and the metal–oxygen framework may further affect such structural changes. Future strategies should aim to balance high initial capacity with durable structural integrity.

(2) Vanadium-based cathodes mainly include layered  $\text{V}_2\text{O}_5$ , tunnel-type  $\text{VO}_2$ , vanadates, and vanadium phosphates. Layered  $\text{V}_2\text{O}_5$  provides large interlayer spacing conducive to  $\text{Al}^{3+}$  storage but suffers from lattice contraction and structural degradation upon cycling. Tunnel-type  $\text{VO}_2$  maintains structural integrity but limits ion diffusion due to fixed tunnel size. Vanadates utilize pre-inserted cations as “pillars” to expand interlayer spacing, enhancing structural stability, whereas vanadium phosphates

feature robust 3D frameworks but limited electronic conductivity due to  $[\text{PO}_4]$  units. Overall, V-based materials often exhibit lower capacity than Mn-based oxides. Similar to Mn-based oxides, although strategies such as defect engineering, metal-ion doping, nanoscale structuring, and conductive composite design can improve the electrochemical performance of V-based cathodes, achieving high capacity, fast kinetics, and long-term stability simultaneously remains challenging.

(3) PBAs offer tunable frameworks, long cycle life, and multiple redox-active centers, showing great promise in AAIBs. Depending on the number of active centers, PBAs are classified as single or dual redox-active center systems. Single-center PBAs are limited by  $\text{Fe}^{2+}/\text{Fe}^{3+}$  charge transfer, with capacities typically in tens of  $\text{mAh g}^{-1}$ , while dual-center PBAs leverage multi-metal synergy to achieve capacities above 100  $\text{mAh g}^{-1}$ . Their remarkable advantage lies in cycling stability, with thousands to tens of thousands of cycles achievable, far exceeding those of Mn- and V-based cathodes. Current strategies to enhance performance include defect engineering to improve ion diffusion, entropy regulation to increase structural robustness *via* multi-metal centers, and nanostructure design to shorten ion transport paths and buffer volume changes. Nevertheless, the relatively low intrinsic capacity of PBAs, together with the limited utilization of redox-active sites, remains a key bottleneck for their application in high-energy AAIBs. Future work should focus on further optimizing framework design to achieve high capacity, high rate, and long lifespan concurrently.

(4) Organic cathodes, composed mainly of C, H, O, and N, possess tunable molecular backbones and flexible structures, alleviating volume strain during charge/discharge. Compared with the strong electrostatic interactions in inorganic cathodes, weak coordination or ion–dipole interactions within the organic framework facilitate  $\text{Al}^{3+}$  ion migration. Energy storage relies on reversible redox-active functional groups, such as carbonyls, imines, or TEMPO radicals. Based on the type of redox-active site, organic cathodes are categorized into quinone-based compounds, N-heteroaromatics,  $\pi$ -conjugated carbonyl-imine hybrids, conductive polymers, and radical polymers. Overall, organic materials typically exhibit better cycling stability than their inorganic counterparts, with capacities higher than those of PBAs but lower than those of Mn oxides. Performance can be improved *via* functional group integration, backbone conjugation optimization, and conductive composite formation. Nevertheless, challenges such as active material dissolution, limited energy density, and balancing molecular stability with high redox activity still hinder practical applications, calling for rational molecular and composite design to achieve high capacity, fast kinetics, and long-term cycling stability.

To further advance the development of high-performance AAIBs, future research should focus on the following directions:

(1) Design and optimization of cathode materials. The structural and chemical characteristics of the cathode critically govern  $\text{Al}^{3+}$  accessibility, migration kinetics, and the reversibility of  $\text{Al}^{3+}$ –cathode interactions. For inorganic cathodes, strategies such as defect engineering, molecular pre-intercalation, heteroatom doping, and conductive network construction should be further explored to expand interlayer



spacing, stabilize frameworks, and create flexible coordination environments. Importantly, future efforts should emphasize establishing clear structure–chemistry–electrochemistry relationships, enabling predictive and rational cathode design. These approaches are expected to mitigate lattice strain during  $\text{Al}^{3+}$ –cathode interactions and enhance charge transfer, enabling higher capacity, improved rate capability, and long-term cycling stability. For organic cathodes, future research should focus on the rational design of multifunctional groups and the modulation of molecular backbone flexibility to facilitate more  $\text{Al}^{3+}$  interactions with active sites. Combined with optimized  $\pi$ -conjugation and conductive composite formation, these strategies can improve ion/electron transport, suppress dissolution and achieve synergistic enhancements in electrochemical performance. Overall, a multiscale, material-tailored design strategy offers a promising pathway toward high-performance and durable AAIB cathodes.

(2) Mechanism insight through advanced characterization and theoretical modeling. *In situ* techniques (XRD, XAS, Raman spectroscopy, *etc.*) combined with first-principles calculations and molecular dynamics simulations can provide atomic-level understanding of ion migration pathways, redox mechanisms, and interfacial processes. Particular attention should be placed on distinguishing  $\text{Al}^{3+}$ -dominated storage from proton-assisted or co-insertion mechanisms, which remains a key challenge in aqueous systems. Correlating structural evolution induced by  $\text{Al}^{3+}$ –cathode interactions with electrochemical performance will offer theoretical guidance for rational cathode design.

(3) Sustainable materials and scalable device engineering. Research should integrate material sustainability with device-level optimization, bridging laboratory studies and practical applications. Development of earth-abundant, environmentally friendly, and low-cost materials, including bio-derived organic and inorganic–organic hybrid frameworks, will enhance AAIB sustainability. Simultaneously, full-cell design optimization and systematic evaluation of long-term stability, safety, and durability under realistic conditions, including extreme cold or high-temperature environments, are essential. Coordinated design of sustainable materials and scalable devices will provide a solid foundation for the practical deployment of AAIBs in green energy storage.

## Author contributions

J. Feng collected papers related to the topic and wrote the manuscript. C. Yu and X. Huang conceived the overall idea of the perspective. The manuscript was revised by all the authors.

## Conflicts of interest

There are no conflicts to declare.

## Data availability

No primary research results, software or code have been included and no new data were generated or analysed as part of this review.

## Acknowledgements

The authors acknowledge the support from the Australian Research Council, the Queensland node of the NCRIS-enabled Australian National Fabrication Facility (ANFF), and the Centre for Microscopy and Microanalysis, The University of Queensland.

## References

- 1 J. Li, J. Fleetwood, W. B. Hawley and W. Kays, From Materials to Cell: State-of-the-Art and Prospective Technologies for Lithium-Ion Battery Electrode Processing, *Chem. Rev.*, 2022, **122**, 903–956.
- 2 A. Manthiram, A reflection on lithium-ion battery cathode chemistry, *Nat. Commun.*, 2020, **11**, 1550.
- 3 J. Xu, X. Cai, S. Cai, Y. Shao, C. Hu, S. Lu and S. Ding, High-Energy Lithium-Ion Batteries: Recent Progress and a Promising Future in Applications, *Energy Environ. Mater.*, 2023, **6**, e12450.
- 4 E. J. M. Dugamin, A. Richard, M. Cathelineau, M. C. Boiron, F. Despinois and A. Brisset, Groundwater in sedimentary basins as potential lithium resource: a global prospective study, *Sci. Rep.*, 2021, **11**, 21091.
- 5 L. Han, L. Wang, Z. Chen, Y. Kan, Y. Hu, H. Zhang and X. He, Incombustible Polymer Electrolyte Boosting Safety of Solid-State Lithium Batteries: A Review, *Adv. Funct. Mater.*, 2023, **33**, 2300892.
- 6 Y. Chen, Y. Kang, Y. Zhao, L. Wang, J. Liu, Y. Li, Z. Liang, X. He, X. Li, N. Tavajohi and B. Li, A review of lithium-ion battery safety concerns: The issues, strategies, and testing standards, *J. Energy Chem.*, 2021, **59**, 83–99.
- 7 X. Gao, Y.-N. Zhou, D. Han, J. Zhou, D. Zhou, W. Tang and J. B. Goodenough, Thermodynamic Understanding of Li-Dendrite Formation, *Joule*, 2020, **4**, 1864–1879.
- 8 X. Cui, J. Wang, S. Sun, X. Chen, Y. Wang, D. Han, J. Wang, X. Yao and W. Yan, Safety Hazards of Lithium Metal Batteries: From the Perspective of Lithium Dendrites and Thermal Runaway, *Energy Fuels*, 2025, **39**, 7665–7690.
- 9 P. K. Nayak, L. Yang, W. Brehm and P. Adelhelm, From Lithium-Ion to Sodium-Ion Batteries: Advantages, Challenges, and Surprises, *Angew. Chem., Int. Ed.*, 2018, **57**, 102–120.
- 10 T. L. Kulova, V. N. Fateev, E. A. Seregina and A. S. Grigoriev, A Brief Review of Post-Lithium-Ion Batteries, *Int. J. Electrochem. Sci.*, 2020, **15**, 7242–7259.
- 11 W. Du, E. H. Ang, Y. Yang, Y. Zhang, M. Ye and C. C. Li, Challenges in the material and structural design of zinc anode towards high-performance aqueous zinc-ion batteries, *Energy Environ. Sci.*, 2020, **13**, 3330–3360.
- 12 D. Wang, Z. Zhang, Y. Hao, H. Jia, X. Shen, B. Qu, G. Huang, X. Zhou, J. Wang, C. Xu and F. Pan, Challenges and Progress in Rechargeable Magnesium-Ion Batteries: Materials, Interfaces, and Devices, *Adv. Funct. Mater.*, 2024, **34**, 2410406.
- 13 T. Dutta and J. Mary Gladis, Recent developments on electrode materials and electrolytes for aluminium-ion batteries, *J. Energy Storage*, 2024, **86**, 111287.



14 M. Ye, Y. Guan, R. Xu, P. Wang, Y. Zhang, J. Yu, D. Li, L. Li, Q. Zhao, Z. Wang, J. Liang and Y. Wu, Aqueous potassium-ion battery cathodes: Current status and prospects, *J. Energy Chem.*, 2025, **106**, 650–670.

15 H. Zhang, L. Qiao and M. Armand, Organic Electrolyte Design for Rechargeable Batteries: From Lithium to Magnesium, *Angew. Chem., Int. Ed.*, 2022, **61**, e202214054.

16 H. Aziam, B. Larhrib, C. Hakim, N. Sabi, H. Ben Youcef and I. Saadoune, Solid-state electrolytes for beyond lithium-ion batteries: A review, *Renew. Sustain. Energy Rev.*, 2022, **167**, 112694.

17 A. A. Yaroshevsky, Abundances of chemical elements in the Earth's crust, *Geochem. Int.*, 2006, **44**, 48–55.

18 X. Zheng, C. Han, C.-S. Lee, W. Yao, C. Zhi and Y. Tang, Materials challenges for aluminum ion based aqueous energy storage devices: Progress and prospects, *Prog. Mater. Sci.*, 2024, **143**, 101253.

19 Y. Zhang, S. Liu, Y. Ji, J. Ma and H. Yu, Emerging Nonaqueous Aluminum-Ion Batteries: Challenges, Status, and Perspectives, *Adv. Mater.*, 2018, **30**, 1706310.

20 J. Tu, W. L. Song, H. P. Lei, Z. J. Yu, L. L. Chen, M. Y. Wang and S. Q. Jiao, Nonaqueous Rechargeable Aluminum Batteries: Progresses, Challenges, and Perspectives, *Chem. Rev.*, 2021, **121**, 4903–4961.

21 B.-E. Jia, A. Q. Thang, C. Yan, C. Liu, C. Lv, Q. Zhu, J. Xu, J. Chen, H. Pan and Q. Yan, Rechargeable Aqueous Aluminum-Ion Battery: Progress and Outlook, *Small*, 2022, **18**, 2107773.

22 D. Chao, W. Zhou, F. Xie, C. Ye, H. Li, M. Jaroniec and S.-Z. Qiao, Roadmap for advanced aqueous batteries: From design of materials to applications, *Sci. Adv.*, 2020, **6**, eaba4098.

23 E. Levi, M. D. Levi, O. Chasid and D. Aurbach, A review on the problems of the solid state ions diffusion in cathodes for rechargeable Mg batteries, *J. Electroceram.*, 2009, **22**, 13–19.

24 F. Wu, H. Yang, Y. Bai and C. Wu, Paving the Path toward Reliable Cathode Materials for Aluminum-Ion Batteries, *Adv. Mater.*, 2019, **31**, 1806510.

25 D. Ma, J. Li, H. Li, D. Yuan, Z. Ji, M. Manawan, C. P. de León Albarran, C. Wu and J. H. Pan, Progress of Advanced Cathode Materials of Rechargeable Aluminum-Ion Batteries, *Energy Mater. Adv.*, 2024, **5**, 0088.

26 K. Bhimani, A. Anjan, V. Mahajani, R. M. Manoj and N. Koratkar, Tuning the Aluminum–Water Interface in Aqueous Aluminum Metal Batteries, *ACS Appl. Energy Mater.*, 2025, **8**, 6194–6202.

27 X. Geng, X. Hou, X. He and H. J. Fan, Challenges and Strategies on Interphasial Regulation for Aqueous Rechargeable Batteries, *Adv. Energy Mater.*, 2024, **14**, 2304094.

28 S. Chen, N. A. Gadelhak, Y. Wu, J. Feng, C. Yu, X. Huang and A. K. Nanjundan, Aqueous Aluminium-Ion Batteries: Cathode Material Design, Anode Engineering and Electrolyte Innovation, *Small*, 2025, e07888.

29 R. Mori, Aqueous rechargeable aluminum battery - a mini review, *Energy Adv.*, 2025, **4**, 1321–1336.

30 H. Sun, B. Chen, M. Tan, Y. Li, X. Lang and Q. Jiang, Rational design and construction of aqueous multivalent metal ion battery systems, *J. Mater. Chem. A*, 2025, **13**, 17159–17196.

31 V. Mathew, B. Sambandam, S. Kim, S. Kim, S. Park, S. Lee, M. H. Alfaruqi, V. Soundharajan, S. Islam, D. Y. Putro, J.-Y. Hwang, Y.-K. Sun and J. Kim, Manganese and Vanadium Oxide Cathodes for Aqueous Rechargeable Zinc-Ion Batteries: A Focused View on Performance, Mechanism, and Developments, *ACS Energy Lett.*, 2020, **5**, 2376–2400.

32 Y. Xu, G. Zhang, J. Liu, J. Zhang, X. Wang, X. Pu, J. Wang, C. Yan, Y. Cao, H. Yang, W. Li and X. Li, Recent Advances on Challenges and Strategies of Manganese Dioxide Cathodes for Aqueous Zinc-Ion Batteries, *Energy Environ. Mater.*, 2023, **6**, e12575.

33 R. Liu, Z. Liang, Y. Xiang, W. Zhao, H. Liu, Y. Chen and K. An, Recognition of V/V/V Multielectron Reactions in Na<sub>3</sub>V(PO<sub>4</sub>)<sub>2</sub>: A Potential High Energy Density Cathode for Sodium-Ion Batteries, *Molecules*, 2020, **25**, 1000.

34 P. M. Hari Prasad, G. Malavika, A. Pillai, S. Sadan and Z. S. Pillai, Emerging organic electrode materials for sustainable batteries, *NPG Asia Mater.*, 2024, **16**, 37.

35 Z. Song and H. Zhou, Towards sustainable and versatile energy storage devices: an overview of organic electrode materials, *Energy Environ. Sci.*, 2013, **6**, 2280–2301.

36 X. Wang, Z. Xi and Q. Zhao, Progress on aqueous rechargeable aluminium metal batteries, *Ind. Chem. Mater.*, 2024, **3**, 7–30.

37 H. Liu, Q. Zhou, Q. Xia, Y. Lei, X. Long Huang, M. Tebyetekerwa and X. Song Zhao, Interface challenges and optimization strategies for aqueous zinc-ion batteries, *J. Energy Chem.*, 2023, **77**, 642–659.

38 Q. Zhao, L. Liu, J. Yin, J. Zheng, D. Zhang, J. Chen and L. A. Archer, Proton Intercalation/De-Intercalation Dynamics in Vanadium Oxides for Aqueous Aluminum Electrochemical Cells, *Angew. Chem., Int. Ed.*, 2020, **59**, 3048.

39 X. Luo, R. Wang, L. Zhang, Z. Liu, H. Li, J. Mao, S. Zhang, J. Hao, T. Zhou and C. Zhang, Air-Stable and Low-Cost High-Voltage Hydrated Eutectic Electrolyte for High-Performance Aqueous Aluminum-Ion Rechargeable Battery with Wide-Temperature Range, *ACS Nano*, 2024, **18**, 12981–12993.

40 Y. Guo, Y. Zhang and H. Lu, Manganese-based materials as cathode for rechargeable aqueous zinc-ion batteries, *Battery Energy*, 2022, **1**, 20210014.

41 B. Zhang, P. Dong, S. Yuan, Y. Zhang, Y. Zhang and Y. Wang, Manganese-Based Oxide Cathode Materials for Aqueous Zinc-Ion Batteries: Materials, Mechanism, Challenges, and Strategies, *Chem Bio Eng.*, 2024, **1**, 113–132.

42 Y. Yuan, C. Liu, B. W. Byles, W. Yao, B. Song, M. Cheng, Z. Huang, K. Amine, E. Pomerantseva, R. Shahbazian-Yassar and J. Lu, Ordering Heterogeneity of [MnO<sub>6</sub>] Octahedra in Tunnel-Structured MnO<sub>2</sub> and Its Influence on Ion Storage, *Joule*, 2019, **3**, 471–484.



43 O. Ghodbane, J.-L. Pascal, B. Fraisse and F. Favier, Structural in Situ Study of the Thermal Behavior of Manganese Dioxide Materials: Toward Selected Electrode Materials for Supercapacitors, *ACS Appl. Mater. Interfaces*, 2010, **2**, 3493–3505.

44 D. Wang, L. Wang, G. Liang, H. Li, Z. Liu, Z. Tang, J. Liang and C. Zhi, A Superior  $\delta$ -MnO<sub>2</sub> Cathode and a Self-Healing Zn- $\delta$ -MnO<sub>2</sub> Battery, *ACS Nano*, 2019, **13**, 10643–10652.

45 Q. Zhao, M. J. Zachman, W. I. Al Sadat, J. Zheng, L. F. Kourkoutis and L. Archer, Solid electrolyte interphases for high-energy aqueous aluminum electrochemical cells, *Sci. Adv.*, 2018, **4**, eaau8131.

46 X. Yang, Q. Sun, L. Chai, S. Chen, W. Zhang, H. Y. Yang and Z. Li,  $\alpha$ -MnO<sub>2</sub> Cathode with Oxygen Vacancies Accelerated Affinity Electrolyte for Dual-Ion Co-Encapsulated Aqueous Aluminum Ion Batteries, *Small*, 2024, **20**, 2400335.

47 H. Gu, X. Yang, S. Chen, W. Zhang, H. Y. Yang and Z. Li, Oxygen Vacancies Boosted Proton Intercalation Kinetics for Aqueous Aluminum–Manganese Batteries, *Nano Lett.*, 2023, **23**, 11842–11849.

48 S. He, J. Wang, X. Zhang, J. Chen, Z. Wang, T. Yang, Z. Liu, Y. Liang, B. Wang, S. Liu, L. Zhang, J. Huang, J. Huang, L. A. O’Dell and H. Yu, A High-Energy Aqueous Aluminum-Manganese Battery, *Adv. Funct. Mater.*, 2019, **29**, 1905228.

49 G. Li, Y. Zhao, B. Guo, J. Zhang, J. Jia, A. Wang and C. Liu, Architecting a High Specific Energy Aqueous Aluminum–Manganese Battery, *Battery Energy*, 2025, e70016.

50 C. Yan, C. Lv, B.-E. Jia, L. Zhong, X. Cao, X. Guo, H. Liu, W. Xu, D. Liu, L. Yang, J. Liu, H. H. Hng, W. Chen, L. Song, S. Li, Z. Liu, Q. Yan and G. Yu, Reversible Al Metal Anodes Enabled by Amorphization for Aqueous Aluminum Batteries, *J. Am. Chem. Soc.*, 2022, **144**, 11444–11455.

51 Q. Ran, H. Shi, H. Meng, S.-P. Zeng, W.-B. Wan, W. Zhang, Z. Wen, X.-Y. Lang and Q. Jiang, Aluminum-copper alloy anode materials for high-energy aqueous aluminum batteries, *Nat. Commun.*, 2022, **13**, 576.

52 C. Wu, S. Gu, Q. Zhang, Y. Bai, M. Li, Y. Yuan, H. Wang, X. Liu, Y. Yuan, N. Zhu, F. Wu, H. Li, L. Gu and J. Lu, Electrochemically activated spinel manganese oxide for rechargeable aqueous aluminum battery, *Nat. Commun.*, 2019, **10**, 73.

53 C. Yan, C. Lv, L. Wang, W. Cui, L. Zhang, K. N. Dinh, H. Tan, C. Wu, T. Wu, Y. Ren, J. Chen, Z. Liu, M. Srinivasan, X. Rui, Q. Yan and G. Yu, Architecting a Stable High-Energy Aqueous Al-Ion Battery, *J. Am. Chem. Soc.*, 2020, **142**, 15295–15304.

54 Y. Liu, G. He, H. Jiang, I. P. Parkin, P. R. Shearing and D. J. L. Brett, Cathode Design for Aqueous Rechargeable Multivalent Ion Batteries: Challenges and Opportunities, *Adv. Funct. Mater.*, 2021, **31**, 2010445.

55 H. Meng, Q. Ran, M.-H. Zhu, Q.-Z. Zhao, G.-F. Han, T.-H. Wang, Z. Wen, X.-Y. Lang and Q. Jiang, Benzoquinone-Lubricated Intercalation in Manganese Oxide for High-Capacity and High-Rate Aqueous Aluminum-Ion Battery, *Small*, 2024, **20**, 2310722.

56 H. Gu, M. Chen, Z. Wang, W. Zhang and Z. Li, Enhancing H<sup>+</sup> intercalation kinetics and stability in Cu<sup>2+</sup> pre-intercalated  $\delta$ -MnO<sub>2</sub> for aqueous aluminum batteries, *J. Energy Chem.*, 2025, **102**, 126–133.

57 A. Zhang, Y. Liang, H. Zhang, Z. Geng and J. Zeng, Doping regulation in transition metal compounds for electrocatalysis, *Chem. Soc. Rev.*, 2021, **50**, 9817–9844.

58 P. Gao, Z. Chen, Y. Gong, R. Zhang, H. Liu, P. Tang, X. Chen, S. Passerini and J. Liu, The Role of Cation Vacancies in Electrode Materials for Enhanced Electrochemical Energy Storage: Synthesis, Advanced Characterization, and Fundamentals, *Adv. Energy Mater.*, 2020, **10**, 1903780.

59 J. Yang, W. Gong and F. Geng, Defect Modulation in Cobalt Manganese Oxide Sheets for Stable and High-Energy Aqueous Aluminum-Ion Batteries, *Adv. Funct. Mater.*, 2023, **33**, 2301202.

60 S. Chen, Y. Kong, C. Tang, N. A. Gadelhak, A. K. Nanjundan, A. Du, C. Yu and X. Huang, Doping Regulation Stabilizing  $\delta$ -MnO<sub>2</sub> Cathode for High-Performance Aqueous Aluminium-ion Batteries, *Small*, 2024, **20**, 2312229.

61 B. Baatiyah, Y. S. Wudil and M. A. Gondal, Recent advances and challenges in MnO<sub>2</sub>-based composite cathodes for high-performance flexible zinc-ion batteries: A critical review, *J. Energy Storage*, 2025, **125**, 117000.

62 Y. Hu, H. Li, H. Gu, W. Zhang and Z. Li, Al<sup>3+</sup> pre-intercalation and g-C<sub>3</sub>N<sub>4</sub> coating synergistically modulate gibbs free energy for robust and compatible MnO<sub>2</sub> cathodes in aqueous aluminum batteries, *Chem. Eng. J.*, 2025, **507**, 160532.

63 J. R. González, F. Nacimiento, M. Cabello, R. Alcántara, P. Lavela and J. L. Tirado, Reversible intercalation of aluminium into vanadium pentoxide xerogel for aqueous rechargeable batteries, *RSC Adv.*, 2016, **6**, 62157–62164.

64 P. De, J. Halder, S. Priya, A. K. Srivastava and A. Chandra, Two-Dimensional V<sub>2</sub>O<sub>5</sub> Nanosheets as an Advanced Cathode Material for Realizing Low-Cost Aqueous Aluminum-Ion Batteries, *ACS Appl. Energy Mater.*, 2023, **6**, 753–762.

65 Z. Wang, H. Gu, T. Wu, W. Zhang and Z. Li, Enhanced dynamics of Al<sup>3+</sup>/H<sup>+</sup> ions in aqueous aluminum ion batteries: Construction of metastable structures in vanadium pentoxide upon oxygen vacancies, *J. Energy Chem.*, 2025, **101**, 562–569.

66 X. Yang, H. Gu, L. Chai, S. Chen, W. Zhang, H. Y. Yang and Z. Li, Construction of V<sub>2</sub>O<sub>5</sub>@MXene Cathodes toward a High Specific Capacity Aqueous Aluminum-Ion Battery, *Nano Lett.*, 2024, **24**, 8542–8549.

67 S. Lee, X.-G. Sun, A. A. Lubimtsev, X. Gao, P. Ganesh, T. Z. Ward, G. Eres, M. F. Chisholm, S. Dai and H. N. Lee, Persistent Electrochemical Performance in Epitaxial VO<sub>2</sub>(B), *Nano Lett.*, 2017, **17**, 2229–2233.

68 Q. He, T. Hu, Q. Wu, C. Wang, X. Han, Z. Chen, Y. Zhu, J. Chen, Y. Zhang, L. Shi, X. Wang, Y. Ma and J. Zhao, Tunnel-Oriented VO<sub>2</sub> (B) Cathode for High-Rate Aqueous Zinc-Ion Batteries, *Adv. Mater.*, 2024, **36**, 2400888.

69 Y. Cai, S. Kumar, R. Chua, V. Verma, D. Yuan, Z. Kou, H. Ren, H. Arora and M. Srinivasan, Bronze-type



vanadium dioxide holey nanobelts as high performing cathode material for aqueous aluminium-ion batteries, *J. Mater. Chem. A*, 2020, **8**, 12716–12722.

70 Y. Wang, X. Shi, J. Wang, X. Liu and X. Lu, Nanobelt-like vanadium dioxide with three-dimensional interconnected tunnel structure enables ultrafast Al-ion storage, *Mater. Today Energy*, 2021, **19**, 100578.

71 Z. Wang, H. Gu and Z. Li, Orbital-Modulated Cu-Doped VO<sub>2</sub> Nanoflowers via Glucose-Assisted Synthesis: Structural Optimization and Electronic Coupling Engineering for High-Capacity Aqueous Aluminum Ion Batteries, *Small*, 2025, **21**, 2503861.

72 V. Soundharajan, S. Nithiananth, J. Lee, J. H. Kim, J.-Y. Hwang and J. Kim, LiV<sub>3</sub>O<sub>8</sub> as an intercalation-type cathode for aqueous aluminium-ion batteries, *J. Mater. Chem. A*, 2022, **10**, 18162–18169.

73 R. Liu, J. Liu, Y. Li, C. Zhang and H. Li, Aqueous aluminium-ion batteries based on layered NH<sub>4</sub>V<sub>4</sub>O<sub>10</sub> nanosheets as cathode, *Solid State Sci.*, 2023, **145**, 107315.

74 V. P. H. Radhakantha, S. Pradhan and A. J. Bhattacharyya, Exploring Aluminum-Ion (Al<sup>3+</sup>) Insertion in Ammonium Vanadium Bronze (NH<sub>4</sub>V<sub>4</sub>O<sub>10</sub>) for Aqueous Aluminum-Ion Rechargeable Batteries, *J. Phys. Chem. C*, 2024, **128**, 20025–20034.

75 T. Wu, Y. Wang, Z. Wang, W. Zhang and Z. Li, Achieving (NH<sub>4</sub>)<sub>2</sub>V<sub>10</sub>O<sub>25</sub>·8H<sub>2</sub>O reversible stable phase transition, fast energy storage, and dynamic characteristics with MXene for aqueous aluminium batteries, *Chem. Eng. J.*, 2024, **499**, 155926.

76 X. Xu, F. Xiong, J. Meng, X. Wang, C. Niu, Q. An and L. Mai, Vanadium-Based Nanomaterials: A Promising Family for Emerging Metal-Ion Batteries, *Adv. Funct. Mater.*, 2020, **30**, 1904398.

77 A. Kravtsev and Y. Ein-Eli, Higher, Stronger, Better ... A Review of 5 Volt Cathode Materials for Advanced Lithium-Ion Batteries, *Adv. Energy Mater.*, 2012, **2**, 922–939.

78 F. Nacimiento, M. Cabello, R. Alcántara, P. Lavela and J. L. Tirado, NASICON-type Na<sub>3</sub>V<sub>2</sub>(PO<sub>4</sub>)<sub>3</sub> as a new positive electrode material for rechargeable aluminium battery, *Electrochim. Acta*, 2018, **260**, 798–804.

79 P. Wang, Z. Chen, H. Wang, Z. Ji, Y. Feng, J. Wang, J. Liu, M. Hu, J. Fei, W. Gan and Y. Huang, A high-performance flexible aqueous Al ion rechargeable battery with long cycle life, *Energy Storage Mater.*, 2020, **25**, 426–435.

80 Q. Pang, S. Yang, X. Yu, W. He, S. Zhang, Y. Tian, M. Xing, Y. Fu and X. Luo, Realizing reversible storage of trivalent aluminium ions using VOPO<sub>4</sub>·2H<sub>2</sub>O nanosheets as cathode material in aqueous aluminium metal batteries, *J. Alloys Compd.*, 2021, **885**, 161008.

81 Y. Liu, J.-L. Yang, H.-H. Liu, J.-M. Cao, Y. Liu and X.-L. Wu, Effective reversible calcium/aluminium ion intercalation into VOPO<sub>4</sub> enabled by organic molecular assistance, *J. Mater. Chem. A*, 2025, **13**, 17404–17410.

82 C. D. Wessells, S. V. Peddada, R. A. Huggins and Y. Cui, Nickel Hexacyanoferrate Nanoparticle Electrodes For Aqueous Sodium and Potassium Ion Batteries, *Nano Lett.*, 2011, **11**, 5421–5425.

83 C. D. Wessells, R. A. Huggins and Y. Cui, Copper hexacyanoferrate battery electrodes with long cycle life and high power, *Nat. Commun.*, 2011, **2**, 550.

84 J. Peng, W. Zhang, Q. Liu, J. Wang, S. Chou, H. Liu and S. Dou, Prussian Blue Analogues for Sodium-Ion Batteries: Past, Present, and Future, *Adv. Mater.*, 2022, **34**, 2108384.

85 Q. Liu, Z. Hu, M. Chen, C. Zou, H. Jin, S. Wang, S.-L. Chou, Y. Liu and S.-X. Dou, The Cathode Choice for Commercialization of Sodium-Ion Batteries: Layered Transition Metal Oxides versus Prussian Blue Analogs, *Adv. Funct. Mater.*, 2020, **30**, 1909530.

86 X.-Y. Fu, L.-L. Zhang, C.-C. Wang, H.-B. Sun and X.-L. Yang, Recent progress of Prussian blue analogues as cathode materials for metal ion secondary batteries, *Rare Met.*, 2025, **44**, 34–59.

87 J. Song, L. Wang, Y. Lu, J. Liu, B. Guo, P. Xiao, J.-J. Lee, X.-Q. Yang, G. Henkelman and J. B. Goodenough, Removal of Interstitial H<sub>2</sub>O in Hexacyanometallates for a Superior Cathode of a Sodium-Ion Battery, *J. Am. Chem. Soc.*, 2015, **137**, 2658–2664.

88 W. Wang, Y. Gang, J. Peng, Z. Hu, Z. Yan, W. Lai, Y. Zhu, D. Appadoo, M. Ye, Y. Cao, Q.-F. Gu, H.-K. Liu, S.-X. Dou and S.-L. Chou, Effect of Eliminating Water in Prussian Blue Cathode for Sodium-Ion Batteries, *Adv. Funct. Mater.*, 2022, **32**, 2111727.

89 Z. Li, K. Xiang, W. Xing, W. C. Carter and Y.-M. Chiang, Reversible Aluminum-Ion Intercalation in Prussian Blue Analogs and Demonstration of a High-Power Aluminum-Ion Asymmetric Capacitor, *Adv. Energy Mater.*, 2015, **5**, 1401410.

90 S. Liu, G. L. Pan, G. R. Li and X. P. Gao, Copper hexacyanoferrate nanoparticles as cathode material for aqueous Al-ion batteries, *J. Mater. Chem. A*, 2015, **3**, 959–962.

91 Z. Zhao, W. Zhang, M. Liu, S. J. Yoo, N. Yue, F. Liu, X. Zhou, K. Song, J.-G. Kim, Z. Chen, X.-Y. Lang, Q. Jiang, C. Zhi and W. Zheng, Ultrafast Nucleation Reverses Dissolution of Transition Metal Ions for Robust Aqueous Batteries, *Nano Lett.*, 2023, **23**, 5307–5316.

92 V. P. H. Radhakantha, J. Tiongson, U. S. Manjunatha, L. O'Dell and A. J. Bhattacharyya, The critical impact of electrolyte concentration on Al<sup>3+</sup> redox and stability of CuHCF in aqueous aluminium-ion batteries, *J. Mater. Chem. A*, 2026.

93 J. Zheng, D. Li, Z. Feng, Y. Wang and T. Sun, Preintercalated Copper Hexacyanoferrate as a Long-Time Cycle Cathode Material for Aqueous Aluminium-Ion Batteries, *ACS Sustain. Chem. Eng.*, 2023, **11**, 6280–6291.

94 K. Sayeed, A. Sadhanala, C. V. Yelamaggad and K. Pandey, Inceptive high-performance flexible aqueous aluminium-ion batteries derived from pre-intercalated copper hexacyanoferrate cathode, *J. Energy Storage*, 2025, **132**, 117881.

95 A. Zhou, L. Jiang, J. Yue, Y. Tong, Q. Zhang, Z. Lin, B. Liu, C. Wu, L. Suo, Y. S. Hu, H. Li and L. Chen, Water-in-Salt Electrolyte Promotes High-Capacity FeFe(CN)<sub>6</sub> Cathode

for Aqueous Al-Ion Battery, *ACS Appl. Mater. Interfaces*, 2019, **11**, 41356–41362.

96 R. Bai, J. Yang, G. Li, J. Luo and W. Tang, Rechargeable aqueous aluminum-FeFe(CN)<sub>6</sub> battery with artificial interphase through deep eutectic solution, *Energy Storage Mater.*, 2021, **41**, 41–50.

97 Y. Gao, H. Yang, X. Wang, Y. Bai, N. Zhu, S. Guo, L. Suo, H. Li, H. Xu and C. Wu, The Compensation Effect Mechanism of Fe–Ni Mixed Prussian Blue Analogues in Aqueous Rechargeable Aluminum-Ion Batteries, *ChemSusChem*, 2020, **13**, 732–740.

98 W. Feng, B. Li, G. Yuan, Y. Li, Y. Zhang, M. Du, Y. Su, Y. Tang, H. Yue, Y. Li, M. Shakouri, H.-C. Chen, W. Li, Z. Liu and H. Pang, High Performance Aluminum Ion Batteries Enabled by the Coordination Between Vanadium-Based PBAs Cathode and Aqueous Eutectic Electrolyte, *Adv. Sci.*, 2025, e11274.

99 D. Wang, H. Lv, T. Hussain, Q. Yang, G. Liang, Y. Zhao, L. Ma, Q. Li, H. Li, B. Dong, T. Kaewmaraya and C. Zhi, A manganese hexacyanoferrate framework with enlarged ion tunnels and two-species redox reaction for aqueous Al-ion batteries, *Nano Energy*, 2021, **84**, 105945.

100 W. Shang, Y. Liu, Y.-N. Liu, J.-L. Yang, H.-H. Liu, H. Yu, J.-M. Cao and X.-L. Wu, Lattice Distortion Confinement Induced by Cationic Vacancy for Ambient Temperature Durable Aluminum-Ion Batteries, *Adv. Funct. Mater.*, 2025, **35**, 2422805.

101 Y.-N. Liu, J.-L. Yang, Z.-Y. Gu, X.-Y. Zhang, Y. Liu, M.-Y. Su, X.-L. Zhang, I. V. Zatovsky, K. Li, J.-M. Cao and X.-L. Wu, Entropy-Regulated Cathode with Low Strain and Constraint Phase-Change Toward Ultralong-Life Aqueous Al-Ion Batteries, *Angew. Chem., Int. Ed.*, 2024, **63**, e202316925.

102 K. Du, Y. Liu, Y. Zhao, H. Li, H. Liu, C. Sun, M. Han, T. Ma and Y. Hu, High-Entropy Prussian Blue Analogues Enable Lattice Respiration for Ultrastable Aqueous Aluminum-Ion Batteries, *Adv. Mater.*, 2024, **36**, 2404172.

103 Y. Ru, S. Zheng, H. Xue and H. Pang, Potassium cobalt hexacyanoferrate nanocubic assemblies for high-performance aqueous aluminum ion batteries, *Chem. Eng. J.*, 2020, **382**, 122853.

104 J. Zheng, J. Liu, M. Ma, R. Zhang, S. Zhang, Y. Wang and T. Sun, Prussian Blue Analogue-Based Nanowires as Cathode Materials for Aqueous Aluminum-Ion Storage, *ACS Appl. Nano Mater.*, 2024, **7**, 28659–28668.

105 W. Chang, J. Peng, W. Mao, Q. Wang, Y. Zhu and N. Peng, Mg-Substituted dual-walled Prussian blue analogous achieving enhanced active sites and stability for aqueous Al-ion batteries, *Chem. Eng. J.*, 2024, **500**, 157204.

106 A. Zhao, J. Peng, W. Mao, Q. Wang, Y. Zhu and N. Peng, Fe-Co PBA/rGO interface strategy enabling fast Al<sup>3+</sup> intercalation for stable aqueous Al-ion batteries, *Chem. Eng. J.*, 2024, **493**, 152790.

107 Y. Lu, Q. Zhang, L. Li, Z. Niu and J. Chen, Design Strategies toward Enhancing the Performance of Organic Electrode Materials in Metal-Ion Batteries, *Chem.*, 2018, **4**, 2786–2813.

108 Y. Qi, H. Zhao and Y. Lei, Organic molecular design for high-power density sodium-ion batteries, *Chem. Commun.*, 2025, **61**, 2375–2386.

109 W. Walker, S. Grugeon, O. Mentre, S. Laruelle, J.-M. Tarascon and F. Wudl, Ethoxycarbonyl-Based Organic Electrode for Li-Batteries, *J. Am. Chem. Soc.*, 2010, **132**, 6517–6523.

110 Y. Liang, Y. Jing, S. Gheytani, K.-Y. Lee, P. Liu, A. Facchetti and Y. Yao, Universal quinone electrodes for long cycle life aqueous rechargeable batteries, *Nat. Mater.*, 2017, **16**, 841–848.

111 X. Peng, Y. Xie, A. Baktash, J. Tang, T. Lin, X. Huang, Y. Hu, Z. Jia, D. J. Searles, Y. Yamauchi, L. Wang and B. Luo, Heterocyclic Conjugated Polymer Nanoarchitectonics with Synergistic Redox-Active Sites for High-Performance Aluminium Organic Batteries, *Angew. Chem., Int. Ed.*, 2022, **61**, e202203646.

112 J. He, X. Shi, C. Wang, H. Zhang, X. Liu, Z. Yang and X. Lu, A quinone electrode with reversible phase conversion for long-life rechargeable aqueous aluminum–metal batteries, *Chem. Commun.*, 2021, **57**, 6931–6934.

113 Y. Li, L. Liu, Y. Lu, R. Shi, Y. Ma, Z. Yan, K. Zhang and J. Chen, High-Energy-Density Quinone-Based Electrodes with [Al(OTf)]<sup>2+</sup> Storage Mechanism for Rechargeable Aqueous Aluminum Batteries, *Adv. Funct. Mater.*, 2021, **31**, 2102063.

114 J. Chen, Q. Zhu, L. Jiang, R. Liu, Y. Yang, M. Tang, J. Wang, H. Wang and L. Guo, Rechargeable Aqueous Aluminum Organic Batteries, *Angew. Chem., Int. Ed.*, 2021, **60**, 5794–5799.

115 J. Cui, Z. Guo, J. Yi, X. Liu, K. Wu, P. Liang, Q. Li, Y. Liu, Y. Wang, Y. Xia and J. Zhang, Organic Cathode Materials for Rechargeable Zinc Batteries: Mechanisms, Challenges, and Perspectives, *ChemSusChem*, 2020, **13**, 2160–2185.

116 H. Li, M. Cao, R. Wang, P. Xiong, Y. Liu, L. Zhang, L. Zhang, L. Zhang, D. Chao and C. Zhang, Design Strategy for Small-Molecule Organic Cathodes: Regulated Active Groups Enable High Capacity and Voltage in Aqueous and Seawater Aluminum Ion Batteries, *Angew. Chem., Int. Ed.*, 2025, **64**, e202508057.

117 Y. Lu, Q. Ge, C. Hu, H. Chen, W. Zhang and Z. Li, An  $\pi$ -conjugated organic cathode with multiple cyano-substituted for stable aqueous aluminum batteries, *J. Colloid Interface Sci.*, 2025, **682**, 281–287.

118 J. Su, M. Zhang, H. Tian, M. Han, Z. Sun, K. Du, F. Cui, J. Li, W. Huang and Y. Hu, Synergistic  $\pi$ -Conjugation Organic Cathode for Ultra-Stable Aqueous Aluminum Batteries, *Small*, 2024, **20**, 2312086.

119 Y. Lu, C. Hu, Y. Hu, W. Zhang and Z. Li, Carbonyl and imine conjugated frameworks for aqueous Organo-Aluminum batteries with high specific capacity and low dissolution, *J. Colloid Interface Sci.*, 2024, **665**, 181–187.

120 C. Hu, Y. Lu, H. Gu, W. Zhang and Z. Li, Multiple Redox Site  $\pi$ -Conjugated Materials for Aqueous Aluminum–Organic Battery Cathodes, *ACS Energy Lett.*, 2024, **9**, 4353–4360.



121 F. Wan, L. Zhang, X. Wang, S. Bi, Z. Niu and J. Chen, An Aqueous Rechargeable Zinc-Organic Battery with Hybrid Mechanism, *Adv. Funct. Mater.*, 2018, **28**, 1804975.

122 X. Li, X. Xie, R. Lv, B. Na, B. Wang and Y. He, Nanostructured Polypyrrole Composite Aerogels for a Rechargeable Flexible Aqueous Zn-Ion Battery with High Rate Capabilities, *Energy Technol.*, 2019, **7**, 1801092.

123 S. Sariyer, A. Ghosh, S. N. Dambasan, E. M. Halim, M. El Rhazi, H. Perrot, O. Sel and R. Demir-Cakan, Aqueous Multivalent Charge Storage Mechanism in Aromatic Diamine-Based Organic Electrodes, *ACS Appl. Mater. Interfaces*, 2022, **14**, 8508–8520.

124 P. Meng, J. Huang, Z. Yang, F. Wang, T. Lv, J. Zhang, C. Fu and W. Xiao, A Low-Cost and Air-Stable Rechargeable Aluminum-Ion Battery, *Adv. Mater.*, 2022, **34**, 2106511.

125 W. Wang, S. Zhang, L. Zhang, R. Wang, Q. Ma, H. Li, J. Hao, T. Zhou, J. Mao and C. Zhang, Electropolymerized Bipolar Poly(2,3-diaminophenazine) Cathode for High-Performance Aqueous Al-Ion Batteries with An Extended Temperature Range of  $-20$  to  $45$  °C, *Adv. Mater.*, 2024, **36**, 2400642.

126 Y. Xiong, Y. Li, X. Cui, S. Li, X. Peng, Y. Ju, T. Zhou, R. Feng, Y. Zhang, Z. Wang, Q. Wang and L. Dong, Stable Radical Polymers as New Electroactive Materials: Synthesis, Properties, and Emerging Applications, *Adv. Funct. Mater.*, 2025, **35**, 2419661.

127 D. R. Nevers, F. R. Brushett and D. R. Wheeler, Engineering radical polymer electrodes for electrochemical energy storage, *J. Power Sources*, 2017, **352**, 226–244.

128 K. Sato, R. Ichinoi, R. Mizukami, T. Serikawa, Y. Sasaki, J. Lutkenhaus, H. Nishide and K. Oyaizu, Diffusion-Cooperative Model for Charge Transport by Redox-Active Nonconjugated Polymers, *J. Am. Chem. Soc.*, 2018, **140**, 1049–1056.

129 S. Jiang, Y. Xie, Y. Xie, L.-J. Yu, X. Yan, F.-G. Zhao, C. J. Mudugamuwa, M. L. Coote, Z. Jia and K. Zhang, Lewis Acid-Induced Reversible Disproportionation of TEMPO Enables Aqueous Aluminum Radical Batteries, *J. Am. Chem. Soc.*, 2023, **145**, 14519–14528.

